# METASURFACE MICROLENS FOCAL PLANE ARRAYS AND MIRRORS

A DISSERTATION SUBMITTED TO
THE GRADUATE SCHOOL OF ENGINEERING AND SCIENCE
OF BILKENT UNIVERSITY
IN PARTIAL FULFILLMENT OF THE REQUIREMENTS FOR
THE DEGREE OF
DOCTOR OF PHILOSOPHY
IN
ELECTRICAL AND ELECTRONICS ENGINEERING

By
Onur Akın
January 2017

METASURFACE MICROLENS FOCAL PLANE ARRAYS AND MIRRORS

By Onur Akın

January 2017

We certify that we have read this dissertation and that in our opinion it is fully adequate, in scope and in quality, as a dissertation for the degree of Doctor of Philosophy.

Hilmi Volkan Demir(Advisor)

Vakur Behçet Ertürk

Oğuz Gülseren

Arif Sanlı Ergün

Tuba Okutucu Özyurt

Approved for the Graduate School of Engineering and Science:

Ezhan Karaşan
Director of the Graduate School

# ABSTRACT

## METASURFACE MICROLENS FOCAL PLANE ARRAYS AND MIRRORS

Onur Akın
Ph.D. in Electrical and Electronics Engineering
Advisor: Hilmi Volkan Demir
January 2017

Lenses, mirrors and focal plane arrays (FPAs) are among the key components affecting the functionality, performance and cost of electro-optical (EO) systems. Conventional lenses rely on phase accumulation mechanism for bending wavefront of light. This mechanism and the scarcity of transparent materials result in high-complexity, high-cost and bulky EO systems. Conventional mirrors, on the other hand, are limited by the electromagnetic properties of metals and cannot be used in certain EO systems. Also, conventional FPAs suffer the fundamental tradeoff between the optical resolution and optical crosstalk. Metasurfaces, relying on the concept of abrupt phase shifts, can be used to built a new class of optical components. However, for realizing metasurfaces, optical resonators should cover a full 0-to-2$\pi$ phase shift response with close to uniform amplitude response. In this thesis, to develop these metasurface optical components, nanoantennas that act as unit cell optical resonators were designed and modeled. A design methodology for building and optimizing these metasurfaces using the designed nanoantennas was developed. After obtaining the metasurfaces, we successfully addressed the problems of optical crosstalk in mid-wavelength infrared (MWIR) FPAs and weak field localization in mirror contacts. Full-wave simulations confirmed major crosstalk suppression of the microlens arrays to achieve $\leq 1\%$ optical crosstalk in the proposed metasurface FPAs, which outperforms all other types of MWIR FPAs reported to date. However, due to intrinsic absorption losses in metals, the resulting device efficiency was low ($\leq 10\%$). To solve this problem, metallic nanoantennas were replaced by dielectric nanodisks and the focusing efficiency was dramatically increased to 80%. This is the first account of high-efficiency low-crosstalk MWIR FPAs. Full-wave simulations also confirmed the strong field localization of metasurface mirrors that can impose a phase shift response close to 0°. The findings of this thesis indicate that metasurface FPAs and mirrors are highly promising for future EO systems.
*Keywords:* Metasurfaces, Microlenses, Magnetic mirrors.

# ÖZET

## METAYÜZEY MİKROLENS ODAK DÜZLEM MATRİSLERİ VE AYNALARI

Onur Akın
Elektrik ve Elektronik Mühendisliği, Doktora
Tez Danışmanı: Hilmi Volkan Demir
Ocak 2017

Mercek, ayna ve odak düzlem matrisleri (ODM) elektro-optik (EO) sistemlerin işlevselliğini, performansını ve maliyetini doğrudan etkileyen önemli bileşenlerdendir. Konvansiyonel mercekler ışığın dalgaboyunu faz biriktirme mekanizmasıyla bükerler. Bu mekanizma ve saydam malzemelerin yetersizliği, EO sistemlerin karmaşıklığının, maliyetinin ve ağırlığının artmasına neden olmaktadır. Diğer yandan, konvasiyonel aynalar metallerin temel elektromanyetik özellikleri ile limitlenmişlerdir ve belirli EO sistemlerde kullanılamazlar. Ayrıca, ODM'ler optik çözünürlük ve optik bağlaşımın arasındaki temel ödünleşim nedeniyle performans kaybına uğramaktadır. Metayüzeyler ani faz kaymaları prensibine dayanmaları sayesinde yeni bir optik bileşen çeşidinin geliştirilmesine olanak tanımaktadır. Ancak, metayüzeylerin gerçeklenebilmesi için, 0-to-$2\pi$ arasındaki faz değişimini neredeyse tektip genlik değişimi ile sağlayabilen optik rezonatörlere ihtiyaç duyulmaktadır. Bu tezde, metayüzey optik bileşenleri tasarlamak için, birim hücre optik rezonatör gibi davranan nanoantenler tasarlanmış ve modellenmiştir. Bu metayüzeylerin gerçeklenebilmesi ve optimizasyonu için bir tasarım yöntemi geliştirilmiştir. Daha sonra bu metayüzeyler kullanılarak, orta kızılötesi bant (OKB) ODM'lerdeki optik bağlaşım ve kontakt aynalardaki zayıf alan lokalizasyonu problemlerine çözüm üretilmiştir. Tam-dalga benzetimleri bağlaşımın büyük ölçüde baskılandığını doğrularken, önerilen metayüzey ODM'lerin $\leq$ %1 optik bağlaşımının diğer OKB ODM'lerden daha düşük olduğunu göstermiştir. Fakat, metallerin özsel kayıpları yüzünden oldukça düşük verimlilik elde edilebilmiştir ($\leq$ %10). Bu sorunu çözmek için metal nanoantenler dielektrik nanoantenler ile değistirilmiş ve verimlilik %80'e çıkarılmıştır. Tam-dalga benzetimleri, metayüzey aynaların kuvvetli alan lokalizasyonunu da doğrulamıştır. Bu tezdeki bulgular, metayüzey ODM ve aynaların gelecek nesil EO sistemlerinin önemli bileşenlerinden olabileceğini göstermektedir.

*Anahtar sözcükler*: Metayüzeyler, Mikrolensler, Manyetik aynalar.

# Acknowledgement

I would like to express my deepest gratitude to my supervisor and mentor Prof. Hilmi Volkan Demir. His invaluable guidance, motivation, encouragement and endless support helped me more than anything else during my journey from an undergraduate student to a PhD candidate making this thesis work.

I would like to thank Prof. Oğuz Gülseren and Prof. Vakur Behçet Ertürk for contributing to the quality of this thesis work by providing invaluable suggestions.

I also would like to thank Prof. Arif Sanlı Ergün and Prof. Tuba Okutucu Özyurt for accepting to be in my thesis jury.

Last but not least, I would like to thank my family and friends for always being there for me.

# Contents

# List of Figures

# List of Tables

# Chapter 1

# Introduction

Motivation of seeing one's own image led to the invention of the mirror which can be labeled as the first optical component. This invention marked the beginning of the field of optics around 2000 BC [3]. Different kinds of optical components, including various types of lenses and prisms, were designed, developed and used through the periods of classical Greece, the Roman Empire and the Islamic Golden age. Between the seventeenth and the nineteenth centuries, a completely new kind of optical components and systems emerged through studies of science pioneers such as Galileo, Newton, Huygens and Fresnel. These inventions led to the major improvements of their age besides the realm of optics and revolutionized our understanding of the universe. Finally, following the breakthrough discovery of electricity, the integration of the field of optics and electronics paved the way for development of complex electro-optical components and systems such as electro-optical (EO) imaging systems.

EO imaging systems typically operate in the visible and near-infrared bands of the electromagnetic spectrum while the operation of the infrared (IR) imaging systems is commonly the far-infrared region. The optical transmission properties of the atmosphere, however, divide the operation bandwidth of the IR imagining systems into two sub-regions: the mid-wave infrared, which is roughly from 3 μm to 5 μm, and the long wave infrared (LWIR), which is from roughly 8 μm to 14 μm [4]. EO and IR imaging systems are composed mainly of optical components, detectors and electronics such as pre-amplifiers and analog-to-digital converters.

Despite its long history of progressive development, optical components still make the major contribution to the phenomena that either limit the functionality or increase the complexity and/or cost of EO and IR imagining systems. For example, the lack of variation in materials used in manufacturing optical components results in limited functionality and the scarcity of such materials increases the cost of these components. Especially, the choice of naturally transparent material is particularly limited in both the near-infrared and MWIR region of the electromagnetic spectrum and this situation dictates usage of special geometries in design and thereby causing difficulties in fabrication processes of the relevant optical components [5]. Another difficulty arises when the optics designer is confronted with the generally conflicting requirements of size and performance of an EO or IR imaging system since an optical component needs to be thick or even bulky for achieving certain functionality using conventional optics. Also, in order to achieve certain functionalities such as achromatic focusing, the number of optical components being used must increase and this situation causes integration difficulties such as proper alignment of the components. Furthermore, additional undesired effects that can cause performance degradation may occur due to functioning mechanisms of conventional optical components. For example, the emergence of diffraction spots at approximately the centers of nearby pixels increased spatial cross-talk in the case of refractive microlens arrays that were purposefully designed to decrease spatial cross-talk [2]. Finally, some applications may require additional functionalities that may not be achievable using the familiar geometries of conventional optical components as in the case of magnetic mirrors [6].

Conventional optical components mainly re-shape the wavefront and/or change the polarization state of light for achieving the required functionalities. For doing so, well-defined gradual phase is accumulated along the path of light through these devices. Generalizing this approach as transformation optics, metamaterials have been designed and developed for functioning as optical components that can achieve novel phenomena such as abnormal light bending, sub-wavelength focusing and cloaking [7, 8]. Despite these promising functionalities, material characteristics still impose rigid restrictions of usual Snell's law on capabilities of optical components based on metamaterials [9]. Moreover, the difficulties in fabricating relatively thick metamaterials cause degradations in relevant optical components performance such as the quite small suppression ratio of thick chiral metamaterials [10].

Recently, metasurfaces that can be defined as the two-dimensional counterparts of matematerials have been investigated progressively [5, 10–30]. Main motivation behind this intensive interest originates from the opportunity that the amplitude, phase and polarization state of light can be controlled using metasurfaces. Controlling such properties of light has paved the door for modulating wavefront, designing beam structure and controlling direction of light on a subwavelength scale [5, 10–12]. Conceptually, phase, amplitude and/or polarization state of light is changed abruptly over the scale of the wavelength as light traverses such a metasurface [13, 14]. This concept is quite different from the one used in designing conventional optical components since the required phase, amplitude and/or polarization state changes are introduced through gradual accumulation over at least several wavelengths in that case. Using this concept, new phenomena such as anomalous reflection, anomalous refraction, strong photonic spin-Hall effect and plasmonic Rashba effect has been observed by realizing proper metasurfaces [5, 15, 16]. The observations of anomalous reflection and refraction led to the generalization of the laws of reflection and refraction. Implementation of this concept has been mainly done using transmissive array metasurfaces with metallic unit elements since most of the optical components function in transmissive mode. Nevertheless, alternative implementations based on either reflective array metasurfaces or dielectric unit elements have also been studied for overcoming the efficiency problems occuring in several of the initial metallic transmissive array metasurface designs. As results of these studies, both high energy conversion of propagating waves into surface waves and anomalous reflection with high efficiency have been observed [17–19]. Moreover, implementation of different types of metasurfaces enabled observation of out-of-plane refraction, generation of optical vortices with a variety of topological charges, manipulation of light polarization state in a controllable manner and generation of holograms [20–25]. Furthermore, birefringent and bianisotropic metasurfaces were also implemented [26, 27].

Of particular interest to our studies is the focusing ability of metasurfaces. This ability has also been investigated in the context of metasurfaces [27–31]. Using transmissive metallic metasurfaces, aberration-free lenses were designed and fabricated at the center wavelength of 1.55 μm [28]. For increasing the efficiency of aberration-free lens metasurfaces, metasurfaces were implemented with different type of unit cells in an another study [29]. Moreover, drawbacks of flat metasurface lenses such as off-axis aberration have also been dealt with the design of aplanatic metasurfaces [30]. Furthermore, single achromatic metalens

designs have been investigated for focusing light at three different wavelengths on the same focal plane [31].

Among their direct utilization as optical components, different types of metasurface, sometimes labeled as metatronics, have been studied for designing lumped nanocircuit elements and frequency selective filters [32–34]. Of particular interest to our studies are the reflection phase controllable metasurface designs that were implemented for increasing the interaction between the active semiconductor material close to contact and electric field [6].

The goal of this thesis work is to model and design novel metasurface architectures and to propose and demonstrate new EO and IR optical components in thin films inspired by these optical metasurfaces. Also, the proposed optical metasurface components is compared and contrasted against the existing conventional approaches and the technological advantages and disadvantages given the state of the art is identified. For achieving these purposes, we study the concept of optical phase discontinuities for modifying phase, amplitude and polarization state of light. We present our studies on understanding the physics of building blocks used to implement metasurfaces. Also, we discuss our approach of using antisymmetric V-shaped antennas for optimizing the functionality of metasurfaces. Moreover, we explain our modeling methodologies and assumptions in using these models. Furthermore, we present our results on simulation and implementation of the designed metasurfaces.

The rest of this thesis is organized as follows. In Chapter 2, first we provide a background for the rest of the thesis. The concept of optical phase discontinuities is progressively explored through several sections of this chapter. Also, Pancharatnam-Berry (PB) phase is briefly summarized and a detailed derivation of the generalized Snell's laws of reflection and refraction is provided. Main principles used in realization of the concept of optical phase discontinuities are summarized. Then, building blocks of metasurfaces are investigated in two different groups (metallic and dielectric building blocks). Major emphasis is given to metallic nanoantennas and various types of them are studied in detail. Simplified models are developed following derivation of integral equations and these models are used to study the scattering amplitudes and phase shifts of these metallic nanoantennas in a large parameter space. Also, results of more realistic but

time-consuming models are provided for a limited parameter space. Finally, recent studies in dielectric nanoantennas are discussed and modeling and simulation of silicon nanodisks that are used to design metasurface lenses are explored.

In Chapter 3, a metasurface design methodology is expressed in detail. Then, using this design methodology, metasurface lenses, metasurface parabolic mirrors and metasurface magnetic mirrors are designed. Full-wave simulations are performed to analyze the scattered field distributions from designed metasurfaces and expected behavior of the designed metasurface lenses and mirrors are confirmed.

In Chapter 4, the optical cross-talk problem in mid-wavelength infrared focal plane arrays (MWIR-FPAs) is addressed using metallic metasurface microlens arrays. Conventional approaches to this optical cross-talk problem are summarized and their drawbacks are discussed. A set of asymmetrically shaped optical antennas are designed and using this set microlens arrays are designed, modeled and simulated using Lumerical FDTD. Then, the scattered field distributions from designed microlens arrays are recorded and analyzed. Finally, the optical cross-talk performance of metasurface microlens arrays integrated FPA's are compared to reference FPA systems.

In Chapter 5, the efficiency problem in metallic metasurface microlens arrays used in MWIR-FPAs is addressed using dielectric metasurface microlens arrays. The drawbacks of metallic metasurfaces are discussed. A set of asymmetrically shaped optical antennas are replaced by silicon nanodisks and using this set of silicon nanodisks, microlens arrays are designed, modeled and simulated using Lumerical FDTD. Then, the scattered field distributions from designed microlens arrays are recorded and analyzed. Finally, both the optical cross-talk performance and efficiency of metasurface microlens arrays integrated FPA's are compared to reference FPA systems.

In Chapter 6, we conclude our thesis study by summarizing the key points and providing the scientific contributions.

# Chapter 2

# Building Blocks of Metasurfaces

Optically thin resonators can be used as the building blocks of metasurfaces. Electromagnetic cavities [35–37], nanoparticle clusters [38–40] and plasmonic antennas [41–44] are different types of optically thin resonators. Due to their widely tailorable optical properties and the ease of fabrication, plasmonic antennas were preferred by many research groups to design and fabricate different types of metasurfaces [9, 13, 14, 17, 21, 25, 27, 45–62]. However, the efficiency of transmitting plasmonic metasurfaces are limited due to the absorption losses of metals. This situation has led to increased attention to dielectric metasurfaces [18, 31, 63–79].

In this chapter, metallic and dielectric nanoantennas that can be used as the building blocks of metasurfaces are investigated. In Section 1, a theoretical background is provided. In Section 2, metallic nanoantennas are described in four subsections. Each of these subsections corresponds to a different geometry of the metallic nanoantennas and either analytic or numerical models of these antennas are provided. In Section 3, different geometries of dielectric nanoantennas are described and recent studies about these antennas are presented. Then, numerical models of dielectric nanoantennas used to realize dielectric metasurfaces are given and their behavior is analyzed.

## 2.1 Background

This section includes three subsections that progressively explore the concept of optical phase discontinuities. In the first subsection, a brief summary of Pancharatnam-Berry (PB) phase, which is fundamentally related to this concept, is given and various studies related to PB optic elements are discussed. In the second subsection, a detailed derivation of the generalized Snell's laws of reflection and refraction is provided since these laws are the key elements to the understanding of this concept. Then, main principles used in realization of this concept are summarized in subsection three.

### 2.1.1 Pancharatnam-Berry Phase

Phase, amplitude and/or polarization state of light can be modified during the processes of wavefront shaping, flow direction change and polarization conversion. Generally, this modification takes place gradually and slowly as realized in the case of conventional optical components. However, sudden modification is also possible via the introduction of phase discontinuities over the scale of wavelength along the optical path. This phase discontinuity or abrupt phase change can be achieved through implementation of space variant subwavelength gratings or arrays of resonators that have subwavelength distance to a nearest neighbor.

In his famous paper, Pancharatnam investigated the phase shift experienced by a light beam that is going through different intermediate polarization states and returning to its original polarization state at the end [80]. Figure 2.1 shows the depiction of this transition on the Poincaré sphere. Red dashed lines correspond to the polarization vectors while green continuous curves correspond to the polarization state transitions that form a geodesic triangle. Although the light beam returned to its original polarization state, it did not have the same initial phase. Pancharatnam experimentally verified this phase shift and showed that it is proportional to the half of the solid angle $S_A$ corresponding to the geodesic triangle on the Poincaré sphere.

In 1987, Berry expressed the phenomena Pancharatnam showed using quantum mechanics and showed its relation to Adiabatic phase [81]. He also mentioned

a very significant point that constitutes the fundamental idea of Pancharatnam-Berry (PB) optic elements and metasurfaces. The polarization changes need not be slow, their sudden accomplishment also leads to phase shifts. This idea was later used in several studies and PB optic elements such as space-variant polarization state manipulating gratings and polarization dependent focusing lenses were demonstrated [82, 83].

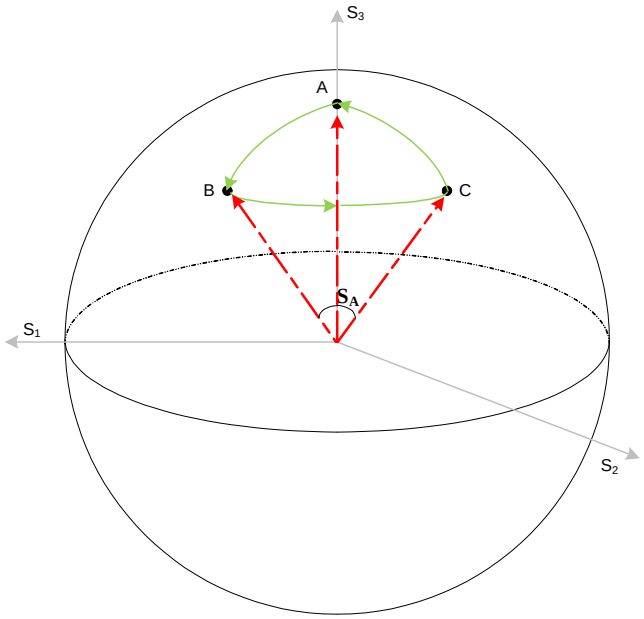


Figure 2.1: Cyclic polarization state transitions on the Poincaré sphere.

### 2.1.2 Generalized Snell's Laws of Reflection and Refraction

Between two points A and B, light rays follow the path that takes the extremum time of travel relative to neighboring points according to Fermat's principle [84]. Figure 2.2 shows the depiction of ray reflection on a surface with zero phase gradient. The straightforward derivation of the law of reflection for this surface using Fermat's principle is given by Equations (2.1) to (2.4). In these equations, the letters $a$, $b$, $d$ and $x$ are the corresponding heights and distances shown in Figure 2.2 while $\Theta_i$ and $\Theta_r$ are the incidence and reflection angles, respectively.

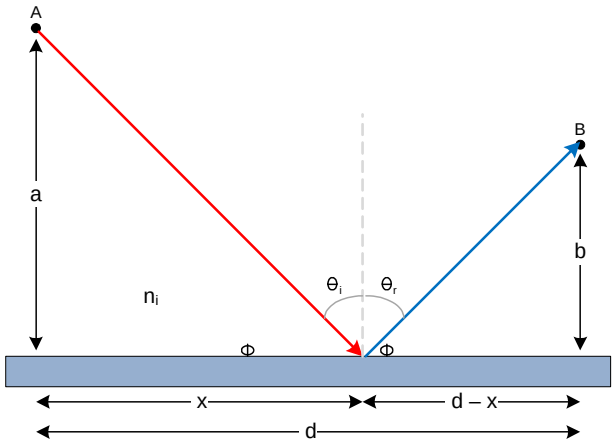


Figure 2.2: Depiction of the law of reflection.

$$L = \sqrt{a^2 + x^2} + \sqrt{b^2 + (d-x)^2} \tag{2.1}$$

$$\frac{dL}{dx} = \frac{1}{2}\frac{2x}{\sqrt{a^2 + x^2}} + \frac{1}{2}\frac{2(d-x)(-1)}{\sqrt{b^2 + (d-x)^2}} = 0 \tag{2.2}$$

$$\frac{x}{\sqrt{a^2 + x^2}} = \frac{(d-x)}{\sqrt{b^2 + (d-x)^2}} \tag{2.3}$$

$$\sin\theta_i = \sin\theta_r \tag{2.4}$$

Introduction of an abrupt phase shift along the surface perturbs the law of reflection. Figure 2.3 shows the depiction of ray reflection from such a surface with nonzero phase gradient. When a planewave having an incidence angle of $\Theta_i$ reflects from this surface, the phase difference between two paths that are infinitesimally close to the actual path taken by the reflecting wave should be zero. Mathematical formulation of this situation is given in Equation (2.5). In this equation, $k_0$ is the wavenumber of light and $n_i$ is the refractive index while $\Theta_i$ and $\Theta_r$ are the incidence and reflection angles, respectively. $\phi$ and $(\phi + d\phi)$ correspond to the abrupt phase shifts at the specified locations of the surface. $dx$ is the distance between two points that the two infinitesimally close paths cross the interface.

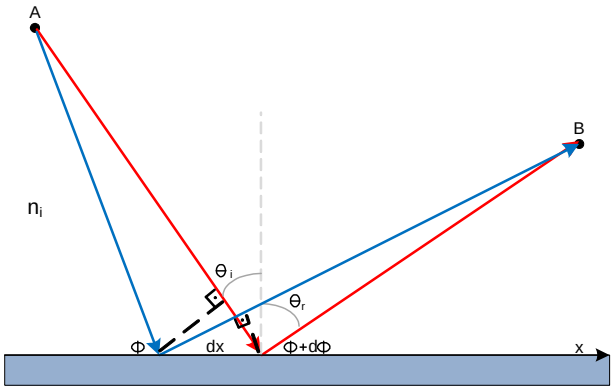


Figure 2.3: Depiction of the law of generalized reflection.

$$[k_0 n_i \sin(\theta_i) dx + (\phi + d\phi)] - [k_0 n_i \sin(\theta_r) dx + \phi] = 0 \tag{2.5}$$

If the phase gradient along the surface is designed to be constant, then Equation (2.5) results in the generalized Snell's law of reflection. This law is provided in Equation (2.6) where $\lambda_0$ is the wavelength of light. The phenomena predicted by this law are fundamentally different from the specular reflection since there is a nonlinear relation between the angles of incidence and reflection. This law also implies that there is a critical angle above which the reflected wave becomes evanescent. This special angle is given by Equation (2.7).

$$\sin(\theta_r) - sin(\theta_i) = \frac{\lambda_0}{2\pi n_i} \frac{d\phi}{dx} \tag{2.6}$$

$$\theta_c^e = \sin^{-1}(1 - \frac{\lambda_0}{2\pi n_i} \left| \frac{d\phi}{dx} \right|) \tag{2.7}$$

Figure 2.4 illustrates the ray refraction through a surface with zero phase gradients between two media having different refractive indices. The derivation of the law of reflection for this surface using Fermat's principle is given by Equations (2.8) to (2.10). In these equations, the letters $a$, $b$, $d$ and $x$ are the corresponding heights and distances shown in Figure 2.2 while $\Theta_i$ and $\Theta_t$ are the incidence and transmittance angles, respectively. $n_i$ and $n_t$ are the refractive indices of the media and $t$ is the time of travel.

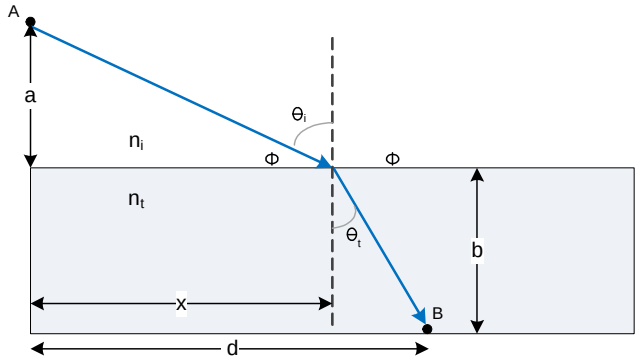


Figure 2.4: Depiction of the law of refraction.

$$t = n_i\sqrt{a^2 + x^2} + n_t\sqrt{b^2 + (d-x)^2} \tag{2.8}$$

$$\frac{dt}{dx} = n_i\frac{x}{\sqrt{a^2 + x^2}} - n_t\frac{d-x}{\sqrt{b^2 + (d-x)^2}} = 0 \tag{2.9}$$

$$n_i \sin\theta_i = n_t sin\theta_t \tag{2.10}$$

Introduction of an abrupt phase shift along the surface perturbs the law of refraction. Figure 2.5 shows the depiction of ray refraction through such a surface with nonzero phase gradient. When a plane wave having an incidence angle of $\Theta_i$ refracts through this surface, the phase difference between two paths that are infinitesimally close to the actual path taken by the refracting wave should be zero. Mathematical formulation of this situation is given in Equation (2.11). In this equation, $k_0$ is the wavenumber of light. $n_i$ and $n_t$ are the refractive indices of the media while $\Theta_i$ and $\Theta_t$ are the incidence and transmittance angles respectively. $\phi$ and $(\phi + d\phi)$ correspond to the abrupt phase shifts at the specified locations of the surface. $dx$ is the distance between two points that the two infinitesimally close paths cross the interface.

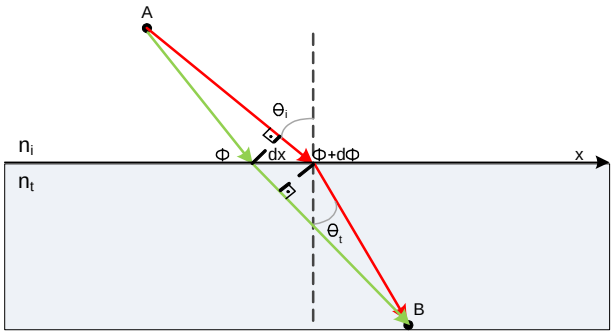


Figure 2.5: Depiction of law of generalized refraction.

$$[k_0 n_i \sin(\theta_i) dx + (\phi + d\phi)] - [k_0 n_t \sin(\theta_t) dx + \phi] = 0 \tag{2.11}$$

If the phase gradient along the surface is designed to be constant, then Equation (2.12) leads to the generalized Snell's law of refraction. This law is given in Equation (2.12) where $\lambda_0$ is the wavelength of light. This equation states that the angle of refraction can be tuned by just changing the phase gradient. Also, the orientation of ray with respect to the surface normal becomes critical even if it has the same angle of incidence. This situation results in two different critical angles given by Equation (2.13).

$$n_t sin(\theta_t) - n_i sin(\theta_i) = \frac{\lambda_0}{2\pi} \frac{d\phi}{dx} \tag{2.12}$$

$$\theta_c = \sin^{-1}(\pm \frac{n_t}{n_i} - \frac{\lambda_0}{2\pi n_i} \frac{d\phi}{dx}) \tag{2.13}$$

### 2.1.3 Concept of Optical Phase Discontinuities

For achieving the nonzero phase gradient along a surface, an array of optically thin resonators with subwavelength separation or subwavelength space-variant polarization-state manipulators shall be used [5, 85]. In the former case, the amplitudes of the scattered field by these resonators shall ideally be equal. In the latter case, the incoming beam is transmitted through a space-variant oriented grooves and the transmission coefficient should be close to one at all points.

In this thesis, we studied optically thin resonators since they offer a more flexible and simpler design methodology. Therefore, this part of the thesis only

involves the realization of the optical phase discontinuities concept by using optically thin resonators. The phenomenon that enables the usage of resonators as building blocks of metasurfaces is the phase shift between the incident and emitted fields across a resonance. The frequency response of a resonator depends on factors such as geometry and material characteristics. So, for designing a metasurface at a certain wavelength regime, one should decide on the appropriate material to be used and then the required phase gradient can be formed by tuning the geometries of the resonators at specified locations. However, when tuning the geometry of the resonator chosen, one should consider several factors and check if these factors are satisfied. The first of these factors is that the scattering amplitude of these resonators shall be equal ideally as previously stated in the beginning of this subsection. In addition to this requirement, the phase shifts of the chosen resonators shall also cover the whole 0-to-$2\pi$ range. This requirement is necessary for full control of the wavefront of light. Finally, another factor used in choosing the type of the resonator is the magnitude of the scattering amplitude and it should be as high as possible for not decreasing the efficiency of the metasurface to be realized.

## 2.2 Metallic Nanoantennas

Metallic nanoantennas are the optical analogues of the radiowave and microwave antennas since they have very similar properties except the additional properties resulting from their small size and resonance condition. In the radiowave and microwave regions of the electromagnetic spectrum, the control and modification of electromagnetic waves by transmitting and reflecting arrays is a well-known technique. Nevertheless, this well-known technique was not a feasible option for the visible and infrared region of the spectrum where the optical components operate. The reason for this situation is the necessity of fabricating antennas having sizes of several hundreds nanometers, which is in the wavelength scale in these regions. Recently, tools such as ion-beam lithography and electron-beam lithography have removed this obstacle and paved the way for designing optical components using this technique.

Primary function of the metallic nanoantennas is converting the optical radiation into localized energy and then re-radiating this energy efficiently with

a specified phase response. In the radiowave and microwave regions, this functionality is achieved by antennas on the order of $\lambda/10$ to $\lambda/100$ (where $\lambda$ is the wavelength of electromagnetic wave). However, in the optical region this fraction of wavelength can correspond to a size of few nanometers. In this length scale, the interaction between light and matter is quantized and the penetration of light into metals cannot be neglected. The finite electrons in the metal cannot create a simultaneous electronic response to the driving field and this delay results in a skin depth that is typically larger than the half diameter of the antenna. Therefore, the electrons of the metal respond to a shorter wavelength than that of the driving field. This wavelength is generally labeled as the effective wavelength and is given by Equation (2.14)

$$\lambda_{eff} = c_1 + c_2 \left( \frac{\lambda}{\lambda_p} \right) \tag{2.14}$$

where $\lambda_p$ is the plasma wavelength while $c_1$ and $c_2$ are geometric constants. The length of a metallic half-wave antenna is determined by half effective wavelength given by this equation. The ratio between the driving field's wavelength and this effective wavelength generally varies between 2 and 5 depending on the geometric factors [42].

### 2.2.1 Rod Nanoantennas

In this subsection, amplitude and phase responses of the simplest metallic nanoantenna, the rod antenna, are provided. For obtaining the mentioned behavior, the rod antenna is modeled with the method of moments (MoM). For obtaining fast results and scanning a large parameter space, a simplified one-dimensional approximation is used.

#### 2.2.1.1 Derivation of the Integral Equation

In the derivation of the integral equation governing the behavior of the rod antenna, thin-wire approximation is used. According to this approximation, both the rod antenna's length and the excitation wavelength are much longer than the radius of the antenna. The simplified geometry of the rod antenna using this

approximation and a reference coordinate system are depicted in Figure 2.6. In this figure, $h$ is the antenna length and $a$ is the antenna radius.

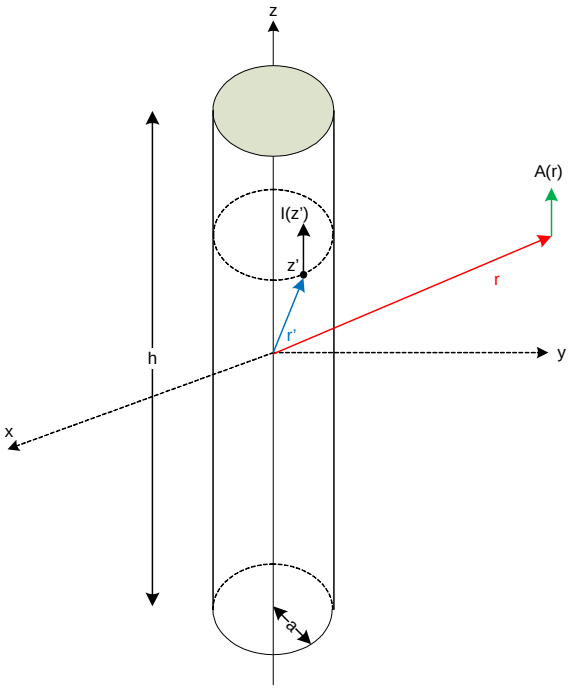


Figure 2.6: Thin-wire model of a rod antenna.

An antenna, whether transmitting or receiving, is always driven by an external source field. In receiving mode, the external source field is called the incident field ($\overline{E}_{inc}$). The incident field induces current on the antenna and the induced current generates its own field ($\overline{E}_{scat}$). Then, the total field, which is the sum of the incident and generated fields, is given by Equation (2.15). For a perfect electric conductor (PEC) antenna, the tangential component of the total electric field should be zero as given in Equation (2.16). Since the direction and the polarization of the incident field is known, the projection of the incident field on the antenna can be found. Then, the scattered field can be defined in terms of the incident field using Equation (2.17).

$$\overline{E}_{tot} = \overline{E}_{inc} + \overline{E}_{scat} \tag{2.15}$$

$$\hat{t} \cdot \overline{E}_{tot} = 0 \tag{2.16}$$

$$\hat{t} \cdot \overline{E}_{scat} = -\hat{t} \cdot \overline{E}_{inc} \tag{2.17}$$

An explicit expression for the scattered field is given by Equation (2.18) for an antenna in a homogeneous medium with an effective refractive index. In this expression, $w$ is the radial frequency of the field; $\mu_o$ and $\varepsilon_o$ are the free space permeability and permittivity, respectively; $\varepsilon_r$ is the permittivity of the effective medium where the antenna is buried; $k$ is the wavenumber; $\overline{A}$ is the vector magnetic potential; and $\nabla$ and $\nabla\cdot$ are the gradient and divergence operators, respectively.

$$\overline{E}_{scat} = \frac{1}{jw\mu_o\varepsilon_o\varepsilon_r}\left[\nabla(\nabla\cdot\overline{A}) + k^2\overline{A}\right] \tag{2.18}$$

Vector magnetic potentials are related to the induced current on the arms of the rod antenna and their direction is parallel to the induced current direction. In the limit of a thin antenna where the radius goes to zero, the reduced Kernel expression can be used. For such a case, vector magnetic potential is related to the induced current as given in Equation (2.19). In this equation, $\widehat{z}$ is the unit vector tangential to the antenna. $R_r$ is the effective distance between the radiated point and the source point.

$$\bar{A} = \frac{\mu_o}{4\pi}\int_h \hat{z}I(z')dz'\frac{e^{-jkR_r}}{R_r} \tag{2.19}$$

Combining Equation (2.17) and Equation (2.19) into Equation (2.18) and rearranging some of the terms, the Pocklington-type integral equation is obtained.

$$-j4\pi w\varepsilon_o\varepsilon_r\hat{z}\cdot\bar{E}_{inc} = \nabla(\nabla\cdot\int_h \hat{z}I(z')dz'\frac{e^{-jkR_r}}{R_r}) + k^2\int_h \hat{z}I(z')dz'\frac{e^{-jkR_r}}{R_r} \tag{2.20}$$

where $R_r$ is given by Equation (2.21). By applying the gradient and divergence operators and rearranging some of the constants, one can end up with Equation (2.22).

$$R_r = \sqrt{(z-z')^2 + a^2} \tag{2.21}$$

$$2kE_{inc}(z) = \left(\partial_z^2 + k^2\right)\frac{j\eta}{2\pi}\int_{-\frac{h}{2}}^{\frac{h}{2}}\frac{e^{-jkR_r}}{R_r}I(z')dz' \tag{2.22}$$

#### 2.2.1.2 MoM Numerical Solution

The objective of the previous section is to derive the Pocklington-type integral equation by applying the thin-wire approximation. However, the resulting Equation (2.22) generally does not have an analytical solution, hence numerical solutions must be implemented to solve this equation. In this subsection, MoM is numerically applied for solving this equation.

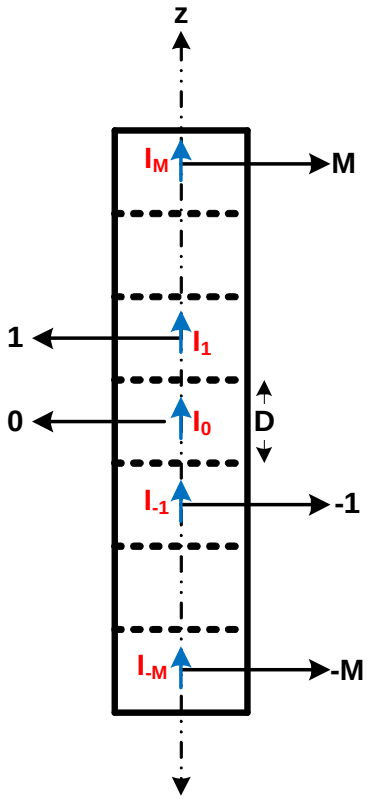


Figure 2.7: Current discretization on a rod antenna.

The rod antenna is discretized into $N$ $(2 \times M + 1)$ slices such that the current distribution is sampled at locations where the spatial variable $z'$ equals to numbers such as $\{-M, -M+1, ..., -1, 0, 1, M-1, M\}$. In Figure 2.7 a schematic representing this discretization process of the rod antenna is provided. $D$ is the sampling period, which is given by Equation (2.23).

$$D = \frac{h}{N} \tag{2.23}$$

For convenience, Equation (2.22) can be rearranged as follows:

$$2kE_{inc}(z) = \left(\partial_z^2 + k^2\right) V(z) \tag{2.24}$$

where $V(z)$ is given by Equation (2.25)

$$V(z) = \int_{-\frac{h}{2}}^{\frac{h}{2}} \kappa(z, z')I(z')dz' \tag{2.25}$$

$$\kappa(z, z') = \frac{j\eta}{2\pi} \frac{e^{-jk\sqrt{(z-z')^2+a^2}}}{\sqrt{(z-z')^2 + a^2}} \tag{2.26}$$

Discretization of Equation (2.25) leads to Equation (2.27) while expansion of the current distribution into a sum of weighted Dirac functions leads to Equation (2.28). Then, by using these two equations one can obtain Equation (2.29).

$$V(z_n) = \int_{-\frac{h}{2}}^{\frac{h}{2}} \kappa(z_n, z')I(z')dz' \tag{2.27}$$

$$I(z') = \sum_{m=-M}^{M} I_m \delta(z' - z_m) \tag{2.28}$$

$$V_n = \sum_{m=-M}^{M} \kappa(z_n, z_m)I_m \tag{2.29}$$

The second derivative with respect to $z$ can now be replaced by the finite difference counterpart that is given by the following equation:

$$\frac{\partial^2}{\partial z^2} V(z_n) = \frac{V(z_{n+1}) - 2V(z_n) + V(z_{n-1})}{D^2} \tag{2.30}$$

Equation (2.24) can be rewritten using Equation (2.30) and rearranging some of the constants with $d = 2k$ and $\alpha = 1 - \frac{k^2 D^2}{2}$,

$$V_{n+1} - 2\alpha V_n + V_{n-1} = E_n d D^2 \tag{2.31}$$

Now, the discrete form of the Pocklington-type integral equation can be written as follows, in which double bars over head denote matrices while vectors are denoted by single bars over head and variables without a bar over head are just scalars:

$$\overline{\overline{A}}\,\overline{\overline{\kappa}}\,\overline{I} = \overline{\overline{Q}}\,d\overline{E} \tag{2.32}$$

where $A$ is given by Equation (2.33) and $Q$ is given by Equation (2.34).

$$A = \frac{1}{D^2}\begin{bmatrix} 0 & 0 & 0 & 0 & 0 & \dots & 0 \\ 1 & -2\alpha & 1 & 0 & 0 & \dots & 0 \\ 0 & 1 & -2\alpha & 1 & 0 & \dots & 0 \\ \vdots & \ddots & \ddots & \ddots & \ddots & \ddots & \vdots \\ 0 & \dots & 0 & 1 & -2\alpha & 1 & 0 \\ 0 & \dots & 0 & 0 & 1 & -2\alpha & 1 \\ 0 & \dots & 0 & 0 & 0 & 0 & 0 \end{bmatrix} \tag{2.33}$$

$$Q = \begin{bmatrix} 0 & 0 & 0 & 0 & 0 & \dots & 0 \\ 0 & 1 & 0 & 0 & 0 & \dots & 0 \\ 0 & 0 & 1 & 0 & 0 & \dots & 0 \\ \vdots & \ddots & \ddots & \ddots & \ddots & \ddots & \vdots \\ 0 & \dots & 0 & 0 & 1 & 0 & 0 \\ 0 & \dots & 0 & 0 & 0 & 1 & 0 \\ 0 & \dots & 0 & 0 & 0 & 0 & 0 \end{bmatrix} \tag{2.34}$$

All of the matrices used in Equation (2.32) are $N \times N$ square matrices. First and last rows of these matrices are purposefully added as zero vectors for making these matrices square. However, both of these rows and the first and last columns of these matrices can be removed since the first and last elements of the current vector ($\overline{I}$) must be 0. This situation is a consequence of the end conditions stating that the current distribution must vanish at the physical ends of the antenna. After removing these rows and columns, the current distribution on the rod antenna can be find using Equation (2.35) where $\overline{\tilde{I}}$ is the reduced current distribution and zeros must be added as the first and last elements. $Z$ is given by Equation (2.36) where all of the variables are matrices.

$$\overline{\tilde{I}} = \overline{\overline{\mathrm{Z}^{-1}} d \overline{\tilde{E}}} \tag{2.35}$$

$$Z = A\kappa Q \tag{2.36}$$

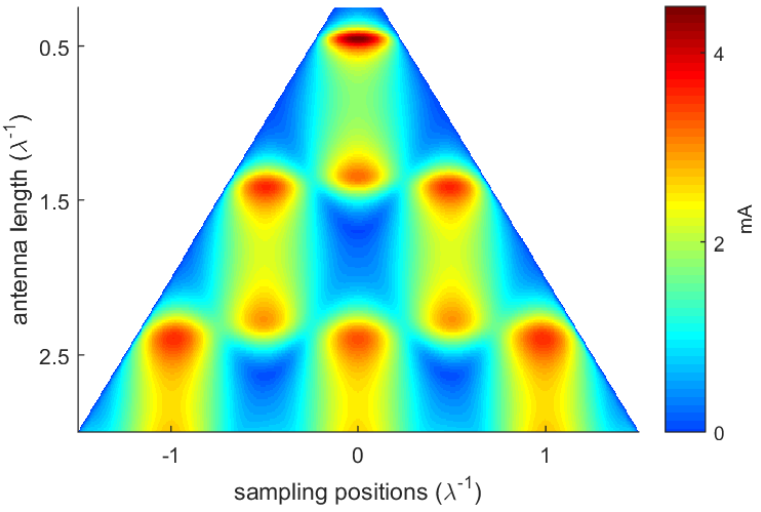


Figure 2.8: Amplitude of current distributions on rod antennas.

For finding the current distribution on a rod antenna using MoM, we first find the projection of the incident field on the rod antenna. Then, we calculate the coefficients including $\alpha$ and $D$. Using these coefficients matrix $A$ is calculated. Then, the impedance matrix $Z$ is calculated using the reduced kernel $Rr$ and multiplied by $A$. Finally, the inverse of the product of $A$ and $Z$ is multiplied by the vector corresponding to the projection of the incident field on the rod antenna for obtaining the current distribution. In Figure 2.8 amplitudes of the current distributions on the rod antennas of varying length are provided. The antenna length is changed from 0.25 to 3.0 wavelength in obtaining the data in this figure with MoM simulations. First, second and third order resonances are clearly observed at the 0.5, 1.5 and 2.5 wavelength long antennas. The phase of the current distributions are also provided in Figure 2.9.

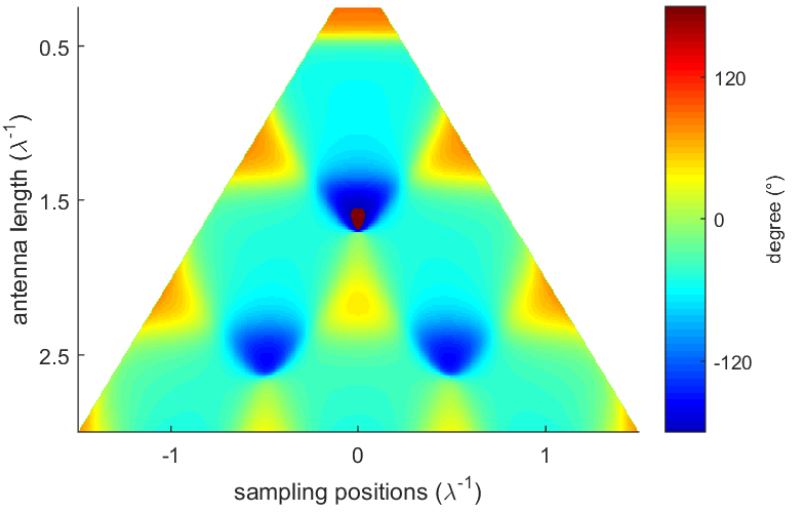


Figure 2.9: Phase of current distributions on rod antennas.

In order to account for the finite conductivity of the metals, the boundary condition given in Equation (2.16) should be modified as given by:

$$\hat{z} \cdot [E_{scat} + E_{inc}] = \frac{1-j}{2\pi a}\sqrt{\frac{\mu_0 \omega}{2\sigma}} I \tag{2.37}$$

where $a$ is the antenna radius, $\mu_0$ is the permeability, $\omega$ is the radial frequency of the incident field, and $\sigma$ is the AC conductivity of the metal. AC conductivity of the metal can be calculated from the DC conductivity of the metal when the frequency of interest is given and the electron relaxation lifetime of the metal is known.

#### 2.2.1.3 Radiation into Farfield

Finding the scattered fields of a metallic rod antenna using MoM is a problem that consists of two parts. Obtaining the current distribution along the antenna for a known incident field is the first part of this problem. For the second part, this current distribution should be re-radiated in order to find the scattered fields. In this subsection, solution to this part of the problem is provided.

The farfield radiation vector is defined as the three-dimensional spatial Fourier

transform of the current density [86] and is given by Equation (2.38).

$$F(\overline{k}) = \int_V J(r')e^{j\overline{k}\cdot\overline{r'}}d^3r' \tag{2.38}$$

where $J(r')$ is the current density on the antenna.This quantity depends on the wavenumber and the directional unit vector $\hat{r}$ which is uniquely defined by the spherical coordinate angles $\theta$ and $\phi$. For a thin-linear antenna, current density can be expressed as follows:

$$J(r) = \hat{z}I(z)\delta(x)\delta(y) \tag{2.39}$$

where $\delta(x)$ and $\delta(y)$ are the Dirac functions of variable $x$ and $y$, respectively, while $I(z)$ is the current distribution. Substituting Equation (2.39) into Equation (2.38) radiation vector of rod antenna is obtained:

$$F = \hat{z}\int_{-\frac{h}{2}}^{\frac{h}{2}} I(z')e^{jk_z z'}dz' \tag{2.40}$$

where $k_z = k\cos\theta$ is the amplitude of the $z$ component of the wavevector (which clearly shows the only angular dependence of radiation vector to the angular variable $\theta$). Electric and magnetic field vectors can be obtained from radiation vector. The relation between electric field and radiation vector is:

$$\overline{E} = -jk\eta\frac{e^{-jkr}}{4\pi r}\left[\hat{\theta}F_\theta + \hat{\phi}F_\phi\right] \tag{2.41}$$

where $\eta$ is the intrinsic impedance of the medium that surrounds the antenna. Inserting Equation (2.40) into Equation (2.41) relation between the scattered electric field and the current distribution on a rod antenna is obtained as in Equation (2.42). By taking the absolute square of this equation and dividing the result by double the intrinsic impedance of the medium, the radiation intensity of rod antennas can be found as given in Equation (2.43). Subsequently, gain pattern of rod antennas can be obtained by normalizing this radiation intensity. In Figure 2.10, normalized power gain pattern of several rod antennas are given. The lengths of these antennas are varied between $0.5\lambda$ and $3.0\lambda$ with incremental steps of $0.5\lambda$. The current distributions on these antennas are calculated using MoM and the scattered fields are obtained by re-radiating these current distributions using Equation (2.42).

$$\bar{E} = \hat{\theta}jk\eta\frac{e^{-jkr}}{4\pi r}\sin\theta\left[\int_{-\frac{h}{2}}^{\frac{h}{2}} I(z')e^{jkz'\cos\theta}dz'\right] \tag{2.42}$$

$$I_{rad} = \frac{\eta k^2}{32\pi^2}|F|^2 \sin^2\theta \tag{2.43}$$

Figure 2.11 shows the variation of amplitude and phase response of a PEC rod antenna located in vacuum with respect to its length. The antenna is excited by an incident field having wavevector normal to the axis of the antenna. Far field data along the wavevector direction is obtained by MoM. The amplitude response of the antenna peaks at the resonance condition of $L = \lambda_{eff}/2$ and the phase response of the antenna changes by an amount equal to $\pi$ across this resonance condition. However, this amount of phase shift is not sufficient for full control of the wavefront of light. For full control of the wavefront, $0 - 2\pi$ phase shift coverage is required. Therefore, rod antennas cannot be used as building blocks of metasurfaces.

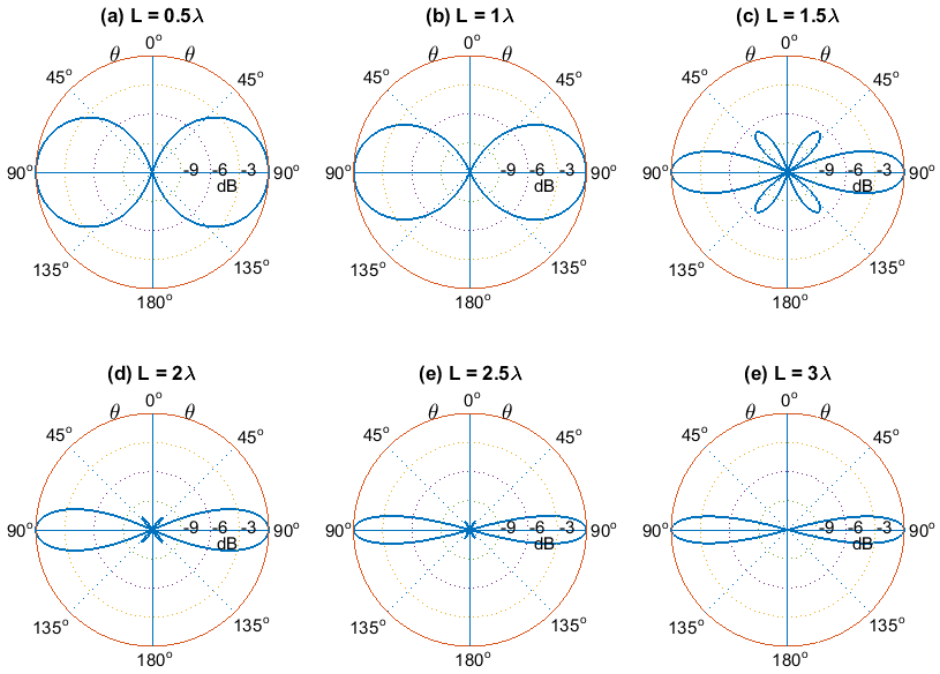


Figure 2.10: Normalized gain patterns of rod antennas.

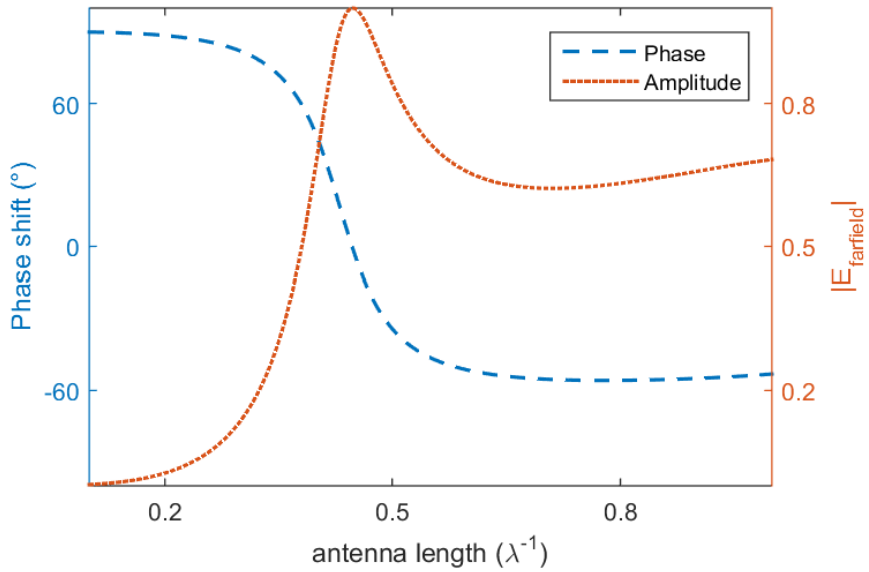


Figure 2.11: Calculated phase and amplitude responses of PEC rod antennas.

### 2.2.2 L-shaped Nanoantennas

In this subsection, amplitude and phase responses of L-shaped metallic nanoantennas are analyzed in detail. For analyzing the mentioned properties, the behavior of this nanoantenna is simulated using MoM methods. For obtaining fast results and scanning a large parameter space, a simplified one-dimensional model is simulated with the MoM method. Unlike rod nanoantennas, L-shaped nanoantennas have phase shift responses that cover the whole 0-$2\pi$ range thereby allowing for a full modification of the wavefront of light.

#### 2.2.2.1 Derivation of the Integral Equation

In the derivation of the integral equation governing the behavior of an L-shaped nanoantenna, thin-wire approximation is used. According to this approximation, antenna length and excitation wavelength are much longer than the radius of the nanoantenna. The simplified geometry of the L-shaped nanoantenna using this approximation and a reference coordinate system are depicted in Figure 2.12. In

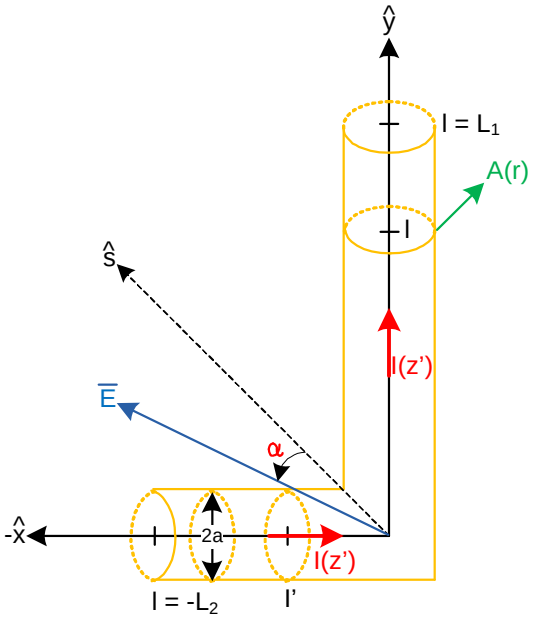


Figure 2.12: Depiction of simplified geometry of L-shaped nanoantennas.

this figure, lengths of the arms of L-shaped nanoantenna can be different and are labeled by symbols ($L_1$ and $L_2$). The angle between these two arms is fixed and is equal to 90°. $a$ is the radius of the nanoantenna while $\alpha$ is the angle between the incident electric field and the symmetry axis of the nanoantenna which is labeled as $\hat{s}$. $l'$ is a spatial variable on the nanoantenna where the source point is located while $l$ is an another spatial variable where the observation point is located. Finally, $A(r)$ is the magnetic potential vector resulting from the current distribution on the nanoantenna.

The total field, which is described in Section 2.2.1.1, is given by Equation (2.15) for the L-shaped nanoantenna. For PEC antennas, the tangential component of this total field should be zero on the antennas as given by Equation (2.16). Rearranging this equation, tangential component of the unknown scattered field can be written in terms of the known incident field as given by Equation (2.17). This scattered field depends on the vector magnetic potential and its dependence for an antenna in a homogeneous medium is given by Equation (2.18).

Vector magnetic potentials are related to the induced current on the arms of the antennas. In the limit of a thin antenna where the radius goes to zero, reduced

Kernel expression can be used. For this limit, vector magnetic potential is related to the induced current as given in Equation (2.44) for an L-shaped nanoantenna.

$$\bar{A} = \frac{\mu_o}{4\pi} \int_{-L_2}^{L_1} \hat{t} I(l') dl' \frac{e^{-jkR_r^L}}{R_r^L} \tag{2.44}$$

where $\hat{t}$ is expressed as follows:

$$\hat{t} = \hat{x} H(-l) + \hat{y} H(l) \tag{2.45}$$

where $H(l)$ is the Heaviside function whose output is 1(0) when its input is positive(negative). Using Equation (2.17) and Equation (2.44) in Equation (2.18) and rearranging some of the terms, the Pocklington type integral equation is obtained for an L-shaped nanoantenna and given by Equation (2.46). However, this equation does not have an analytical solution and a numerical solution must be used to solve this equation for obtaining the induced current distribution on this nanoantenna.

$$-j4\pi w \varepsilon_o \varepsilon_r \hat{t} \cdot \bar{E}_{inc} = \hat{t} \cdot \left[ \nabla(\nabla \cdot \int_{-L_2}^{L_1} \hat{t} I(l') dl' \frac{e^{-jkR_r^L}}{R_r^L}) + k^2 \int_{-L_2}^{L_1} \hat{t} I(l') dl' \frac{e^{-jkR_r^L}}{R_r^L} \right] \tag{2.46}$$

where $R_r^L$ is the reduced effective distance for the L-shaped nanoantenna. In order to calculate the reduced effective distance, two different conditions should be considered for the L-shaped nanoantenna:

1. When the observation and source points are on the same arm ($l$ and $l'$ have the same sign)
2. When the observation and source points are on the different arms ($l$ and $l'$ have different signs)

For case 1, Equation (2.47) should be used for the L-shaped nanoantenna. For case 2, Equation (2.48) should be used for the L-shaped nanoantenna.

$$R_r = \sqrt{a^2 + (l - l')^2} \tag{2.47}$$

where $l$ and $l'$ should have same signs since they are on the same arm.

$$R_r^L = \sqrt{a^2 + l^2 + l'^2} \tag{2.48}$$

where $l$ and $l'$ should have different signs since they are on different arms.

For an antenna that has tangential unit vectors lying in only $\hat{x}$ and $\hat{y}$ directions, gradient of divergence of the vector magnetic potential is given by Equation (2.49) or Equation (2.50).

$$\nabla(\nabla \cdot \overline{A}) \cdot \widehat{y} = \left[ \frac{\partial}{\partial y} \left( \frac{\partial}{\partial y} A_y + \frac{\partial}{\partial x} A_x \right) \right] \tag{2.49}$$

$$\nabla(\nabla \cdot \overline{A}) \cdot \widehat{x} = \left[ \frac{\partial}{\partial x} \left( \frac{\partial}{\partial x} A_x + \frac{\partial}{\partial y} A_y \right) \right] \tag{2.50}$$

For the L-shaped nanoantenna, the arm along $-\hat{x}$ direction is labeled as $\Gamma_1$ and the other arm is labeled as $\Gamma_2$ meaning arm 1 and arm 2, respectively. In order to find the vector magnetic potential affecting arm 1 of this antenna, $\hat{x}$ and $\hat{y}$ directed components of the vector magnetic potential shall be found. Only the current on arm 2 creates a vector magnetic potential that has $\hat{x}$ component and flow direction of this current is chosen to be the $\hat{x}$ direction as depicted in Figure 2.12. The vector magnetic potential due to this current is given as follows:

$$A_{1x} = \frac{\mu_o}{4\pi} \int_{-L_2}^{0} (I(l')) \frac{e^{-jkR_{rd}^L}}{R_{rd}^L} dl' \tag{2.51}$$

where $R_{rd}^L$ is defined by Equation (2.52). $x$ and $y$ are the observation point coordinates. $l'$ is the source point and its sign should be negative when used in calculations since sampling points on arm 2 is defined for values between 0 and $-L_2$ where $L_2$ is the length of arm 2.

$$R_{rd}^L = \sqrt{a^2 + (x - l')^2 + y^2} \tag{2.52}$$

The derivative of the kernel $\frac{e^{-jkR_{rd}^L}}{R_{rd}^L}$ with respect to $x$ is given by the following equation and it should be evaluated at $x$ equals 0 since the source point is on the antenna. $\left(R_{rd}^L\right)'$ is given by Equation (2.54) for L-shaped nanoantenna.

$$\frac{\partial}{\partial x} \frac{e^{-jkR_{rd}^L}}{R_{rd}^L} = \left( -jk \frac{e^{-jkR_{rd}^L}}{R_{rd}^L} - \frac{e^{-jkR_{rd}^L}}{\left(R_{rd}^L\right)^2} \right) \left(R_{rd}^L\right)' \tag{2.53}$$

$$\frac{\partial R_{rd}^L}{\partial x} = \frac{1/2 \times 2(x - l')}{\sqrt{\left(a^2 + (x - l')^2 + y^2\right)}} = \frac{-l'}{R_{rd}^L} \tag{2.54}$$

Using Equation (2.53) and Equation (2.54) in Equation (2.51), explicit expression for x component of the vector magnetic potential on arm 1 is obtained:

$$\frac{\partial A_{1x}}{\partial x} = \frac{\mu_o}{4\pi} \int_{-L_2}^{0} I(l') \frac{e^{-jkR_{rd}^L}}{(R_{rd}^L)^3} (1 + jkR_{rd}^L) l' dl' \tag{2.55}$$

where $R_{rd}^L$ is given by Equation (2.48) if $y$ is replaced by $l$.

For the L-shaped nanoantenna, only the current on arm 1 creates a vector magnetic potential that has $\hat{y}$ directed component. Flow direction of this current is chosen to be plus $\hat{y}$ direction. The vector magnetic potential due to this current is given as follows:

$$A_{1y} = \frac{\mu_o}{4\pi} \int_{0}^{L_1} I(l') \frac{e^{-jkR_{rs}^L}}{R_{rs}^L} dl' \tag{2.56}$$

where $R_{rs}^L$ is defined by the following equation. $l'$ is the source point and its sign is positive as a result of the coordinate system choice. Note that $x$ is 0 on arm 1, hence source point is only represented by $y$.

$$R_{rs}^L = \sqrt{a^2 + (y - l')^2} \tag{2.57}$$

In Figure 2.12, the orientation of the incident field is given with respect to the antenna symmetry axis. $\alpha$ is defined as the incidence angle and taken counter clockwise direction from the symmetry axis of the antenna. Incident field propagation direction is assumed to be out of page($+z$) direction. Boundary condition for arm 1 of L-shaped nanoantenna with the assumption of antenna being a perfect electric conductor is given as follows:

$$-E_{inc} \cos(\frac{\pi}{4} + \alpha) = \frac{1}{jw\mu_o\varepsilon_o\varepsilon_r} \left[ \left( \frac{\partial^2}{\partial y^2} + k^2 \right) A_{1y} + \frac{\partial}{\partial y} \left( \frac{\partial A_{1x}}{\partial x} \right) \right] \tag{2.58}$$

The constants in Equation (2.58) can be re-arranged as follows:

$$-\frac{1}{jw\mu_o\varepsilon_o\varepsilon_r} \frac{\mu_o}{4\pi} = \frac{1}{2k} \frac{j\eta}{2\pi} \tag{2.59}$$

where $\eta$ is the effective intrinsic impedance of the effective homogeneous medium where the antenna is placed. Then, the boundary condition for arm 1 can be

written as follows:

$$
\begin{aligned}
&2kE_{inc}\cos(\frac{\pi}{4}+\alpha) = \\
&\frac{j\eta}{2\pi}\left(\left[\frac{\partial^2}{\partial y^2}+k^2\right]\int_0^{L_1} I(l')\frac{e^{-jkR_{rs}^L}}{R_{rs}^L}dl'\right) + \\
&\frac{j\eta}{2\pi}\left(\frac{\partial}{\partial y}\int_{-L_2}^{0} I(l')\frac{e^{-jkR_{rd}^L}}{(R_{rd}^L)^3}(1+jkR_{rd}^L)l'dl'\right)
\end{aligned}
\tag{2.60}
$$

Rearranging Equation (2.60) and replacing variable $y$ with $l$, the following equation is obtained:

$$
\begin{aligned}
&2kE_{inc}\cos(\frac{\pi}{4}+\alpha) = \\
&\frac{j\eta}{2\pi}\left(\left[\frac{\partial^2}{\partial l^2}+k^2\right]\int_{-L_2}^{L_1} I(l')\kappa_1(l,l')dl'\right) + \\
&\frac{j\eta}{2\pi}\left(\frac{\partial}{\partial l}\int_{-L_2}^{L_1} I(l')\kappa_2(l,l')dl'\right)
\end{aligned}
\tag{2.61}
$$

where $\kappa_1$ is the integral kernel of the integration that will be differentiated twice and given by Equation (2.62). $\kappa_2$ is the integral kernel of the integration that will be differentiated only once and given by Equation (2.63).

$$
\kappa_1(l,l') = \frac{e^{-jkR_{rs}^L}}{R_{rs}^L}H(l') \tag{2.62}
$$

where $H$ symbolizes the Heaviside function whose output is 1 when its input is positive. $R_{rs}^L$ is given by Equation (2.47).

$$
\kappa_2(l,l') = \frac{e^{-jkR_{rd}^L}}{(R_{rd}^L)^3}(1+jkR_{rd}^L)l'H(-l') \tag{2.63}
$$

where $R_{rd}^L$ is given by Equation (2.48).

For arm 2, only the current on arm 1 creates a vector magnetic potential that has $y$ component and flow direction of this current is chosen to be $y$ direction. The vector magnetic potential due to this current is given by the following equation:

$$
A_{2y} = \frac{\mu_o}{4\pi}\int_0^{L_1} I(l')\frac{e^{-jkR_{rd}^L}}{R_{rd}^L}dl' \tag{2.64}
$$

where $R_{rd}^L$ is defined by the following equation. $x$ and $y$ are the observation point coordinates. $l'$ is the source point and its sign is positive as a result of the coordinate system choice.

$$R_{rd}^L = \sqrt{a^2 + x^2 + (y - l')^2} \tag{2.65}$$

The derivative of the integral kernel of Equation (2.64) with respect to $y$ is given by the following equation and it should be evaluated for $y$ being equal to 0.

$$\frac{\partial}{\partial y}\frac{e^{-jkR_{rd}^L}}{R_{rd}^L} = \left(-jk\frac{e^{-jkR_{rd}^L}}{R_{rd}^L} - \frac{e^{-jkR_{rd}^L}}{(R_{rd}^L)^2}\right)(R_{rd}^L)' \tag{2.66}$$

The derivative of the effective distance is calculated for the case of $y$ being equal to 0 and the result is given by the following equation:

$$\frac{\partial R_{rd}^L}{\partial y} = \frac{y - l'}{\sqrt{a^2 + x^2 + (y - l')^2}} = \frac{-l'}{R_{rd}^L} \tag{2.67}$$

Using Equation (2.66) and Equation (2.67) in Equation (2.64), the derivative of the $y$ component of the vector magnetic potential with respect to variable $y$ can be obtained as given in Equation (2.68). Effective distance is given by Equation (2.69) for the case of $y$ being equal to 0.

$$\frac{\partial A_{2y}}{\partial y} = \frac{\mu_o}{4\pi}\int_0^{L_1} I(l')\frac{e^{-jkR_{rd}^L}}{(R_{rd}^L)^3}(1 + jkR_{rd}^L)l'dl' \tag{2.68}$$

$$R_{rd}^L = \sqrt{a^2 + x^2 + l'^2} \tag{2.69}$$

Only the current on arm 2 creates a vector magnetic potential that has $x$ component and flow direction of this current is chosen to be negative $x$ direction. The vector magnetic potential due to this current is given by the following equation:

$$A_{2x} = \frac{\mu_o}{4\pi}\int_{-L_2}^{0} I(l')\frac{e^{-jkR_{rs}^L}}{R_{rs}^L}dl' \tag{2.70}$$

where $R_{rs}^L$ is defined by the following equation. $l'$ is the source point and its sign is negative as a result of the coordinate system choice. Note that $y$ is 0 on arm 2, hence source point is only represented by $x$.

$$R_{rs}^L = \sqrt{a^2 + (x - l')^2} \tag{2.71}$$

Boundary condition for arm 2 with the assumption of antenna being a perfect electric conductor is given by the following equation:

$$-E_{inc}\cos(\frac{3\pi}{4}+\alpha)=\frac{1}{jw\mu_o\varepsilon_o\varepsilon_r}\left[\left(\frac{\partial^2}{\partial x^2}+k^2\right)A_{2x}+\frac{\partial}{\partial x}\left(\frac{\partial A_{2y}}{\partial y}\right)\right] \tag{2.72}$$

The constants in Equation (2.72) can be re-arranged as follows.

$$\frac{1}{jw\mu_o\varepsilon_o\varepsilon_r}\frac{\mu_o}{4\pi}=-\frac{1}{2k}\frac{j\eta}{2\pi} \tag{2.73}$$

where $\eta$ is the effective intrinsic impedance of the homogeneous medium where the antenna stands. Then, the boundary condition for arm 2 can be written as follows:

$$\begin{aligned}&2kE_{inc}\cos(\frac{3\pi}{4}+\alpha)=\\&\frac{j\eta}{2\pi}\left(\left[\frac{\partial^2}{\partial x^2}+k^2\right]\int_{-L_2}^{0}I(l')\frac{e^{-jkR_{rs}^L}}{R_{rs}^L}dl'\right)+\\&\frac{j\eta}{2\pi}\left(\frac{\partial}{\partial x}\int_{0}^{L_1}I(l')\frac{e^{-jkR_{rd}^L}}{(R_{rd}^L)^3}(1+jkR_{rd}^L)l'dl'\right)\end{aligned} \tag{2.74}$$

Rearranging Equation (2.74) and replacing variable $x$ with $l$, the following equation is obtained:

$$\begin{aligned}&2kE_{inc}\cos(\frac{3\pi}{4}+\alpha)=\\&\frac{j\eta}{2\pi}\left(\left[\frac{\partial^2}{\partial l^2}+k^2\right]\int_{-L_2}^{L_1}I(l')\kappa_3(l,l')dl'\right)+\\&\frac{j\eta}{2\pi}\left(\frac{\partial}{\partial l}\int_{-L_2}^{L_1}I(l')\kappa_4(l,l')dl'\right)\end{aligned} \tag{2.75}$$

where $\kappa_3$ is the integral kernel of the integration that will be differentiated twice and given by Equation (2.76). $\kappa_4$ is the integral kernel of the integration that will be differentiated only once and given by Equation (2.77).

$$\kappa_3(l,l')=\frac{e^{-jkR_{rs}^L}}{R_{rs}^L}H(l') \tag{2.76}$$

where $H$ symbolizes the Heaviside function whose output is 1 when its input is positive. $R_{rs}^L$ is given by Equation (2.47).

$$\kappa_4(l,l')=\frac{e^{-jkR_{rd}^L}}{(R_{rd}^L)^3}(1+jkR_{rd}^L)l'H(l') \tag{2.77}$$

where $R_{rd}^{L}$ is given by Equation (2.48).

Combining the boundary conditions for both arms of the L-shaped nanoantenna, one can obtain the following equation:

$$\begin{aligned} &2kE_{inc}\left[\cos(\frac{\pi}{4}+\alpha)H(l)+\cos(\frac{3\pi}{4}+\alpha)H(-l)\right]= \\ &\frac{j\eta}{2\pi}\left(\left[\frac{\partial^2}{\partial l^2}+k^2\right]\int_{-L_2}^{L_1} I(l')\kappa_1(l,l')dl'\right)+ \\ &\frac{j\eta}{2\pi}\left(\frac{\partial}{\partial l}\int_{-L_2}^{L_1} I(l')\kappa_2(l,l')dl'\right) \end{aligned} \tag{2.78}$$

Where $\kappa_1$ and $\kappa_2$ are given by Equation (2.79) and Equation (2.80).

$$\kappa_1(l,l') = \frac{e^{-jkR_{rs}^{L}}}{R_{rs}^{L}}\left[H(l)H(l')+H(-l)H(-l')\right] \tag{2.79}$$

where $R_{rs}^{L}$ is given by Equation (2.47).

$$\kappa_2(l,l') = (1+jkR_{rd}^{L})\frac{e^{-jkR_{rd}^{L}}}{(R_{rd}^{L})^3}l'\left[H(l)H(-l')+H(-l)H(l')\right] \tag{2.80}$$

where $R_{rd}^{L}$ is given by Equation (2.48).

#### 2.2.2.2 MoM Numerical Solution

The Pocklington type integral equation Equation (2.78) does not have an analytical solution, hence numerical solutions must be implemented to solve this equation. In this subsection, MoM is applied for solving this equation. The antenna is discretized into $N$ ($N = N_1 + N_2$) parts such that the curvilinear variable $l'$ is sampled at points $\{-N_2, -N_2+1, ..., -1, 1, ..., N_1-1, N_1\}$. Figure 2.13 contains a schematic representing the discretization of the antenna. $D$ is the sampling period which is given by the following simple relation:

$$\frac{L_1+L_2}{N-1} \tag{2.81}$$

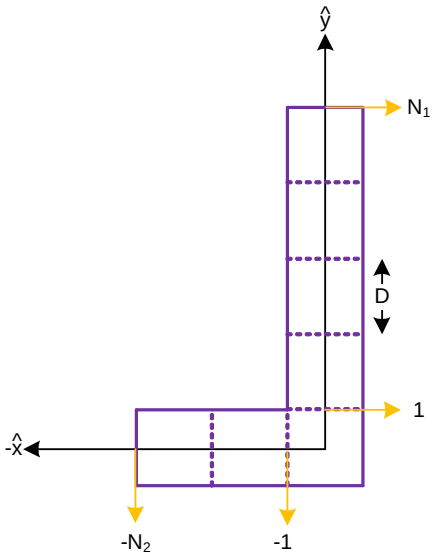


Figure 2.13: Current discretization on an L-shaped nanoantenna.

After discretization the integration parts of the Equation (2.78) are represented by discrete functions $V^1[l_n]$ and $V^2[l_n]$ which are given as follows:

$$V^{(i)}[l_n] = \frac{j\eta}{2\pi}\left\{\int_{-L_2}^{L_1} I(l')\kappa^{(i)}(l_n, l')dl'\right\} \tag{2.82}$$

The current distribution on the antenna is expanded into a sum of weighted Dirac functions:

$$I(l') = \sum_{m=-N_2}^{N_1} I_m \delta(l' - l_m) \tag{2.83}$$

When this weighted distribution is used in Equation (2.82), the following relation is obtained:

$$V_n{}^{(i)} = \sum_{m=-N_2}^{N_1} \kappa_{nm}^{(i)} I_m \tag{2.84}$$

$\kappa_{nm}^{(1)}$ and $\kappa_{nm}^{(2)}$ are given by the following equations:

$$\kappa_{nm}^{(1)} = \frac{j\eta}{2\pi}\frac{e^{-jkR_{rs}^L}}{R_{rs}^L}\left[H(l_n)H(l_m) + H(-l_n)H(-l_m)\right] \tag{2.85}$$

$$\kappa_{nm}^{(2)} = \frac{j\eta}{2\pi}(1 + jkR_{rd}^L)\frac{e^{-jkR_{rd}^L}}{(R_{rd}^L)^3} l_m \left[H(-l_n)H(l_m) + H(l_n)H(-l_m)\right] \tag{2.86}$$

First and second order derivatives of $V^{(i)}[l_n]$ are given by Equation (2.87) and Equation (2.88) where finite difference schemes are used to convert derivatives in the integral equation into sums.

$$\frac{\partial^2}{\partial l^2}V^1(l) = \frac{V^1_{n+1} - 2V^1_n + V^1_{n-1}}{D^2} \tag{2.87}$$

$$\frac{\partial}{\partial l}V^2(l) = \frac{V^2_{n+1} - V^2_{n-1}}{2D} \tag{2.88}$$

Equation (2.78) can be rewritten after discretization by using Equation (2.87) and Equation (2.88) after rearranging some of the constants such as $d = 2k$ and $\alpha = 1 - \frac{k^2D^2}{2}$:

$$\frac{1}{D^2}\left(V^1_{n+1} - 2\alpha V^1_n + V^1_{n-1}\right) + \frac{1}{2D}(V^2_{n+1} - V^2_{n-1}) = dE_n \tag{2.89}$$

where $E_n$ is the discretized (normalized) incident field projection on the antenna and given by the following equation:

$$E_n = \cos(\frac{\pi}{4} + \alpha)H(l_n) + \cos(\frac{3\pi}{4} + \alpha)H(-l_n) \tag{2.90}$$

Now, the discrete form of the Pocklington type integral equation can be written as follows:

$$\left[\mathrm{A}\kappa^{(1)} + C\kappa^{(2)}\right] I = QdE \tag{2.91}$$

where $A$ is given by Equation (2.92), $C$ is given by Equation (2.93) and $Q$ is given by Equation (2.94).

$$A = \frac{1}{D^2}\begin{bmatrix} 0 & 0 & 0 & 0 & 0 & \dots & 0 \\ 1 & -2\alpha & 1 & 0 & 0 & \dots & 0 \\ 0 & 1 & -2\alpha & 1 & 0 & \dots & 0 \\ \vdots & \ddots & \ddots & \ddots & \ddots & \ddots & \vdots \\ 0 & \dots & 0 & 1 & -2\alpha & 1 & 0 \\ 0 & \dots & 0 & 0 & 1 & -2\alpha & 1 \\ 0 & \dots & 0 & 0 & 0 & 0 & 0 \end{bmatrix} \tag{2.92}$$

$$C = \frac{1}{2D}\begin{bmatrix} 0 & 0 & 0 & 0 & 0 & \dots & 0 \\ -1 & 0 & 1 & 0 & 0 & \dots & 0 \\ 0 & -1 & 0 & 1 & 0 & \dots & 0 \\ \vdots & \ddots & \ddots & \ddots & \ddots & \ddots & \vdots \\ 0 & \dots & 0 & -1 & 0 & 1 & 0 \\ 0 & \dots & 0 & 0 & -1 & 0 & 1 \\ 0 & \dots & 0 & 0 & 0 & 0 & 0 \end{bmatrix} \tag{2.93}$$

$$Q = \begin{bmatrix} 0 & 0 & 0 & 0 & 0 & \dots & 0 \\ 0 & 1 & 0 & 0 & 0 & \dots & 0 \\ 0 & 0 & 1 & 0 & 0 & \dots & 0 \\ \vdots & \ddots & \ddots & \ddots & \ddots & \ddots & \vdots \\ 0 & \dots & 0 & 0 & 1 & 0 & 0 \\ 0 & \dots & 0 & 0 & 0 & 1 & 0 \\ 0 & \dots & 0 & 0 & 0 & 0 & 0 \end{bmatrix} \tag{2.94}$$

All of the matrices used in Equation (2.91) are $N \times N$ square matrices. First and last rows of these matrices are purposefully added as zero vectors for making these matrices square. However, both of these rows and first and last columns of these matrices can be removed since the first and last elements of the current vector $(\overline{I})$ must be 0. This situation is a consequence of the end conditions which state that the current distribution must vanish at the physical ends of the antenna. After removing these rows and columns, current distribution on the L-shaped nanoantenna can be find using Equation (2.95) where $I$ is the reduced current distribution and zeros must be added as the first and last elements. $Z$ is given by Equation (2.96)

$$I = dZ^{-1}E \tag{2.95}$$

$$Z = A\kappa Q \tag{2.96}$$

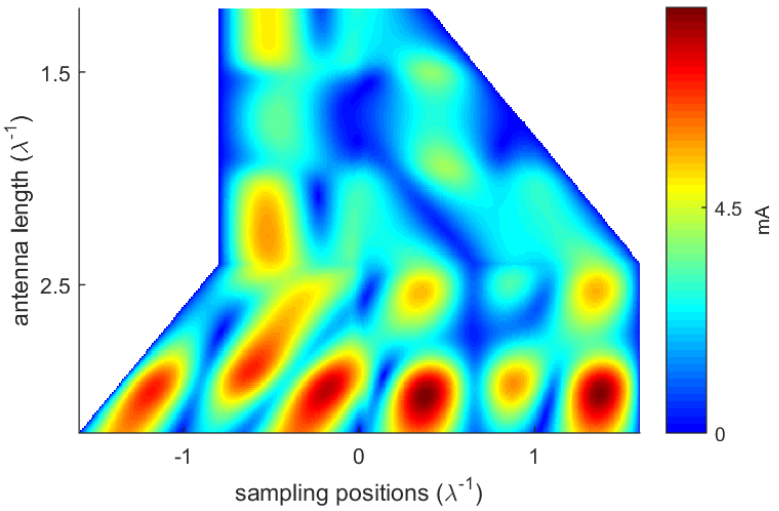


Figure 2.14: Amplitudes of the current distributions on L-shaped nanoantennas with symmetric excitation.

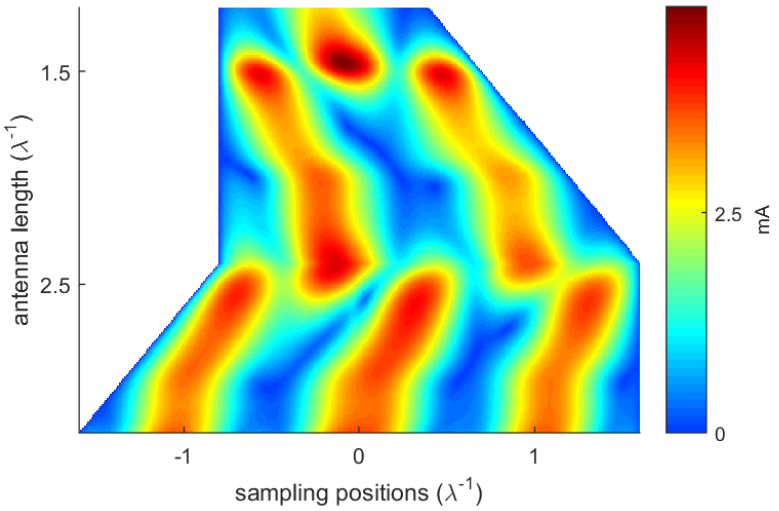


Figure 2.15: Amplitudes of the current distributions on L-shaped nanoantennas with antisymmetric excitation.

For finding the current distribution on an L-shaped nanoantenna using MoM, we first find the projection of the incident field on the L-shaped nanoantenna. Then, we calculate the coefficients such as $\alpha$ and $D$. Using these coefficients matrix $A$ and $C$ are calculated. Then, the impedance matrix $Z_1$ and $Z_2$ are calculated using the reduced kernels $R_r d$ and $R_r s$ and multiplied by $A$ and $C$, respectively. Finally, the inverse of the summation of the multiplication of $A$ and $Z_1$ and the multiplication of $C$ and $Z_2$ is multiplied by the vector corresponding to the projection of the incident field on the L-shaped nanoantenna for obtaining the current distribution.

In Figure 2.14 amplitudes of the current distributions on L-shaped nanoantennas of varying arm lengths are provided for the case of symmetric excitation. In the symmetric excitation, the polarization of the incident field has the same direction of the antenna symmetry axis. For this excitation, the arms of the antennas act as rod antennas of length $L_1$ and $L_2$ and their resonance conditions occur proportional to these lengths.

In Figure 2.15 amplitudes of the current distributions on L-shaped nanoantennas of varying arm lengths are provided for the case of antisymmetric excitation. In the antisymmetric excitation, the polarization of the incident field has a direction that is orthogonal to the antenna symmetry axis. For this excitation, the antennas act similar to rod antennas of length $L$ and their resonance condition occur proportional to this length. The total antenna lengths are varied from 1.2 to 3.2 wavelength in obtaining the data in these figures with MoM simulations. The phase of the current distributions are also provided in Figure 2.16 and Figure 2.17 for the cases of symmetric and antisymmetric excitations.

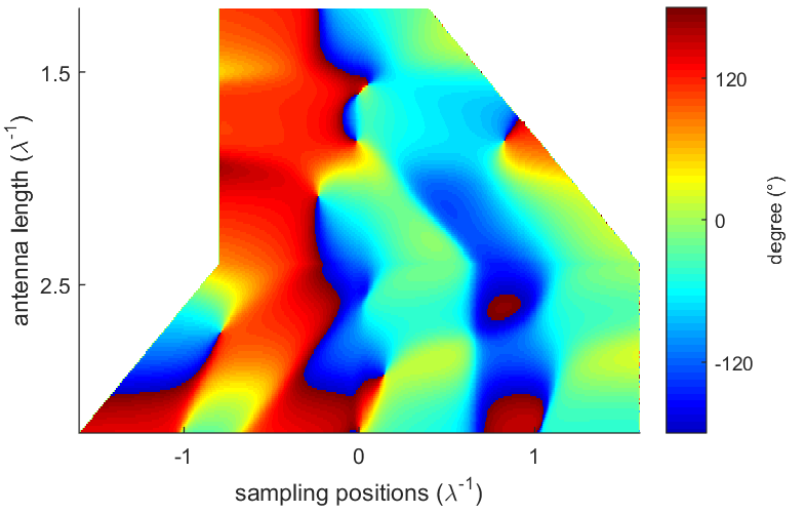


Figure 2.16: Phase of the current distribution on a L-shaped nanoantenna with symmetric excitation

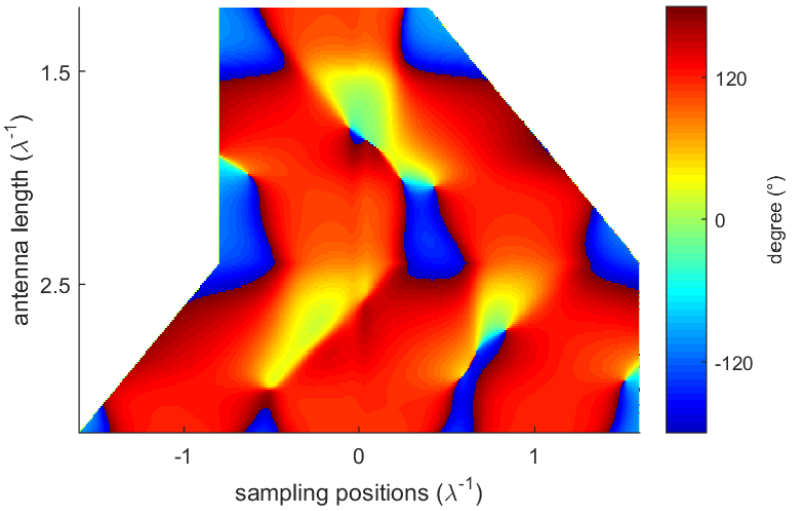


Figure 2.17: Phase of the current distribution on a L-shaped nanoantenna with antisymmetric excitation

In order to account for the finite conductivity of the metals, the boundary condition given in Equation (2.16) should be modified as follows:

$$\hat{t} \cdot [E_{scat} + E_{inc}] = \frac{1-j}{2\pi a}\sqrt{\frac{\mu_0 \omega}{2\sigma}} I \tag{2.97}$$

where $a$ is the antenna radius, $\mu_0$ is the permeability, $\omega$ is the radial frequency of the incident field and $\sigma$ is the AC conductivity of the metal. AC conductivity of the metal can be calculated from the DC conductivity of the metal when the frequency of interest is given and the electron relaxation lifetime of the metal is known.

#### 2.2.2.3 Radiation into Farfield

Finding the scattered fields of a metallic L-shaped nanoantenna using MoM is a problem that consists of two parts. Obtaining the current distribution along the antenna for a known incident field is the first part of this problem. For the second part, this current distribution should be re-radiated in order to find the scattered fields. In this subsection, solution to this part of the problem is provided.

The far-field radiation vector is defined as the three-dimensional spatial Fourier transform of the current density [86] and is given by Equation (2.98).

$$F(\overline{k}) = \int_V J(r') e^{j\overline{k}\cdot\overline{r'}} d^3 r' \tag{2.98}$$

where $J(r')$ is the current density on the antenna.This quantity depends on the wavenumber and the directional unit vector $\hat{r}$ which is completely defined by the spherical coordinate angles $\theta$ and $\phi$. For a thin-linear antenna, current density can be expressed as follows:

$$J(r) = I(l')\left[\hat{x}\delta(y)\delta(z)H(-l') + \hat{y}\delta(x)\delta(z)H(l')\right] \tag{2.99}$$

where $\delta(x)$, $\delta(y)$ and $\delta(z)$ are the dirac functions of variable $x$, $y$ and $z$, respectively while $I(l')$ is the current distribution. Wavevector $\overline{k}$ is expressed in the spherical coordinate system as follows:

$$\overline{k} = k\hat{r} = k(\hat{x}\cos\phi sin\theta + \hat{y}\sin\phi sin\theta + \hat{z}\cos\theta) \tag{2.100}$$

Then, $\bar{k} \cdot \bar{r}' = (\frac{2\pi}{\lambda}\hat{r}) \cdot (l'\hat{l}) = 2\pi\frac{l'}{\lambda}(\hat{r} \cdot \hat{l})$ is given as follows:

$$\bar{k} \cdot \bar{r}' = 2\pi\frac{l'}{\lambda}\sin\theta\left\{H(-l')cos\phi + H(l')\sin\phi\right\} \tag{2.101}$$

For an $x$ directed antenna standing on top of a semiconductor dielectric interface, $\theta$ electric field component is given by Equation (2.102) and $\phi$ electric field component is given by Equation (2.103)( [87]). For a $y$ directed antenna $\cos\phi$ terms should be replaced by $\sin\phi$ terms and $\sin\phi$ terms should be replaced by $-\cos\phi$ terms.

$$\begin{aligned} E_\theta = &\left[\frac{(\cos\theta)^2}{\cos\theta + \sqrt{(n^2 - (\sin\theta)^2)}}\right]\cos\phi \\ &- \left[(\sin\theta)^2\cos\theta\frac{\cos\theta - \sqrt{(n^2 - (\sin\theta)^2)}}{n^2\cos\theta + \sqrt{(n^2 - (\sin\theta)^2)}}\right]\cos\phi \end{aligned} \tag{2.102}$$

$$E_\phi = -\frac{\cos\theta}{\cos\theta + \sqrt{(n^2 - (\sin\theta)^2)}}\sin\phi \tag{2.103}$$

For designing metasurfaces using L-shaped metallic antennas, their far-field amplitude and phase responses along the incident field's wavevector direction should be considered. Hence, $\theta$ and $\phi$ used in Equation (2.101), Equation (2.102) and Equation (2.103) can be set to 0. Then, both of the electric field components along the $\hat{x}$ and $\hat{y}$ directions reduce to $\frac{1}{1+n}$. Also, $\bar{k} \cdot \bar{r}'$ diminishes for $\theta$ equals 0.

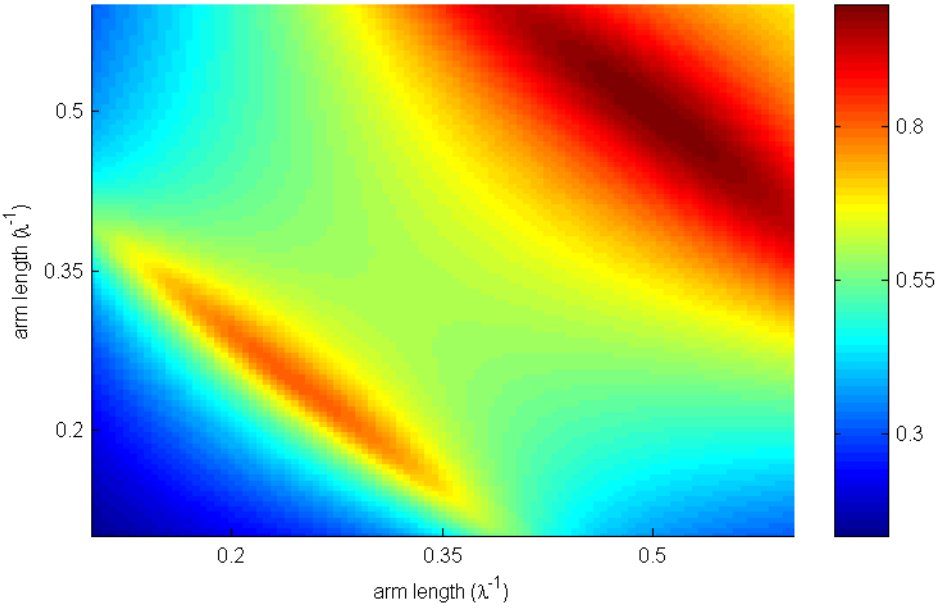


Figure 2.18: The scattered field amplitudes of L-shaped nanoantennas.

Far field amplitudes and phase shifts of L-shaped nanoantennas having varying arm lengths are shown in Figure 2.18 and Figure 2.19. In order to obtain these data, L-shaped nanoantennas are excited by electric field polarized along arm 2 and the scattered field along the normal direction to the antenna plane is calculated. Only the cross-polarized (with respect to incident field) scattered field is considered. Lengths of both antenna arms are varied between 0.1 and 0.6 effective wavelength so that it is possible to excite both resonance modes for most of the antennas. Antennas are considered to be fabricated from gold when considering the effect of finite conductivity of real metals. Scattered field amplitudes of L-shaped nanoantennas maximized when both arm lengths have length close to 0.5 effective wavelength. However, antennas having scattered field amplitudes greater than 0.6 of the maximum scattering field amplitude can also be used to design metasurfaces up to a certain performance. Scattered field phase shifts of these antennas cover the whole $0-2\pi$ range as seen in Figure 2.19. Therefore, L-shaped nanoantennas can be used to design metasurfaces.

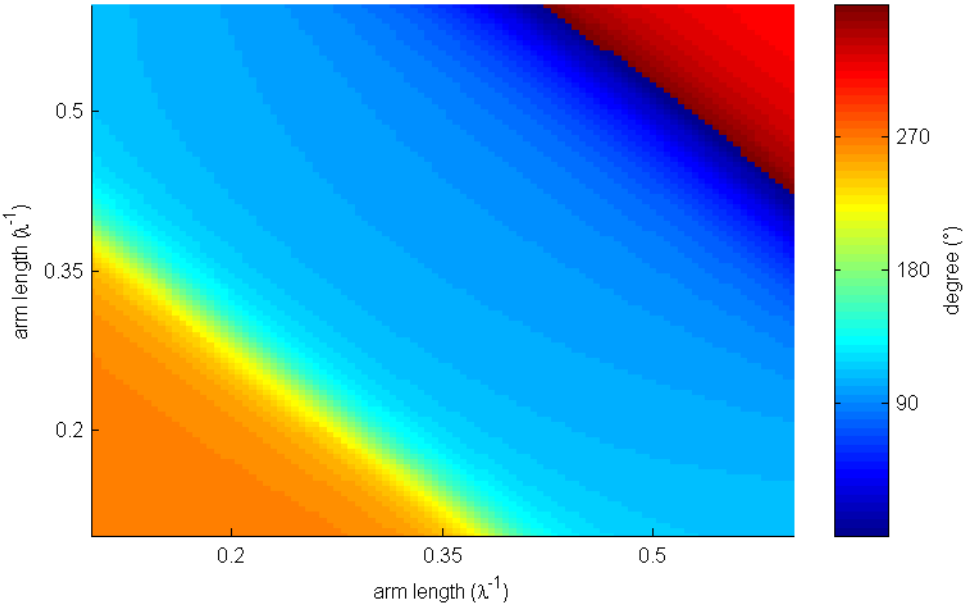


Figure 2.19: The scattered field phase shifts of L-shaped nanoantennas.

### 2.2.3 V-shaped Nanoantennas

In this subsection, amplitude and phase responses of V-shaped metallic antennas are provided. For obtaining the mentioned data, the behavior of this antenna is simulated using both FDTD and MoM methods. The results of the time consuming FDTD simulations are used as references while a simplified model is simulated with MoM method for obtaining fast results and scanning a large parameter space. Similar to L shaped nanoantennas, V-shaped nanoantennas have also phase shift responses that cover the whole 0-2$\pi$ range thereby allowing for a full modification of the wavefront of light.

#### 2.2.3.1 Derivation of the Integral Equation

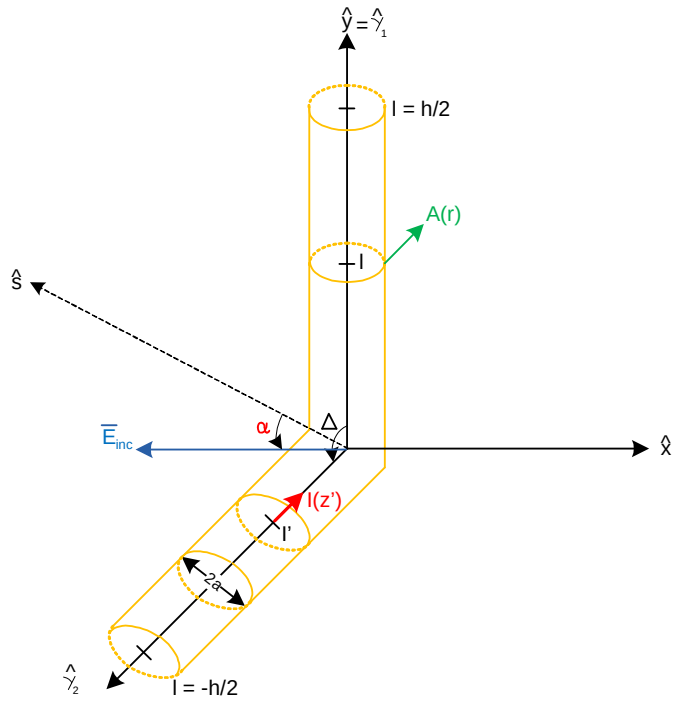


Figure 2.20: Depiction of simplified geometry of V-shaped nanoantennas.

In the derivation of the integral equation governing the behavior of a V-shaped nanoantenna, thin-wire approximation is used. According to this approximation, antenna length and the excitation wavelength are much longer than the radius of the antenna. The simplified geometry of the V-shaped nanoantenna using this approximation and a reference coordinate system are depicted in Figure 2.20. In this figure, lengths of the arms of V-shaped nanoantenna are equal and $h$ corresponds to the total length of these two equivalent arms. $\Delta$ is the angle between these two arms and will be referenced as the opening angle throughout this chapter. $a$ is the radius of the antenna while $\alpha$ is the angle between the incident electric field and the symmetry axis of the antenna which is labeled as $\hat{s}$. $l'$ is a spatial variable on the antenna where the source point is located while $l$ is another spatial variable where the observation point is located. Finally, $A(r)$ is the magnetic potential vector.

The total field, which is described in Section 2.2.1.1, is given by Equation (2.15) for the V-shaped nanoantenna. For PEC antennas, the tangential component of this total field should be zero on the antennas as given by Equation (2.16).

Rearranging this equation, tangential component of the unknown scattered field can be written in terms of the known incident field as given by Equation (2.17). This scattered field depends on the vector magnetic potential and its dependence for an antenna in a homogeneous medium is given by Equation (2.18).

Vector magnetic potentials are related to the induced current on the arms of the antennas. In the limit of a thin antenna where the radius goes to zero, reduced Kernel expression can be used. For this limit, vector magnetic potential is related to the induced current as given in Equation (2.104) for a V-shaped nanoantenna.

$$\bar{A} = \frac{\mu_o}{4\pi} \int_{-\frac{h}{2}}^{\frac{h}{2}} \hat{t} I(l') dl' \frac{e^{-jkR_r^V}}{R_r^V} \tag{2.104}$$

where $\hat{t}$ is expressed as follows:

$$\hat{t} = \left[\hat{x} \sin\Delta - \hat{y} \cos\Delta\right] H(-l) + \hat{y} H(l) \tag{2.105}$$

where $H(l)$ is the Heaviside function whose output is 1(0) when its input is positive(negative). Using Equation (2.17) and Equation (2.104) in Equation (2.18) and rearranging some of the terms, the Pocklington type integral equation is obtained for a V-shaped nanoantenna and given by Equation (2.106). However, this equation does not have an analytical solution and a numerical solution must be used to solve this equation for obtaining the induced current distribution on this antenna.

$$-j4\pi w \varepsilon_o \varepsilon_r \hat{t} \cdot \bar{E}_{inc} = \hat{t} \cdot \left[ \nabla(\nabla \cdot \int_{-\frac{h}{2}}^{\frac{h}{2}} \hat{t} I(l') dl' \frac{e^{-jkR_r^V}}{R_r^V}) + k^2 \int_{-\frac{h}{2}}^{\frac{h}{2}} \hat{t} I(l') dl' \frac{e^{-jkR_r^V}}{R_r^V} \right] \tag{2.106}$$

where $R_r^V$ is the reduced effective distance for the V-shaped nanoantenna. In order to calculate the reduced effective distance, two different conditions should be considered for the V-shaped nanoantenna:

1. when the observation and source points are on the same arm ($l$ and $l'$ have the same sign)

2. when the observation and source points are on the different arms ($l$ and $l'$ have different signs)

For Case 1, Equation (2.47) should be used for the V-shaped nanoantenna. For Case 2, Equation (2.107) should be used for the V-shaped nanoantenna.

$$R_r^V = \sqrt{a^2 + (l + l'cos\Delta)^2 + (l'sin\Delta)^2} \tag{2.107}$$

For an antenna that has tangential unit vectors lying in only $\hat{x}$ and $\hat{y}$ directions, gradient of divergence of the vector magnetic potential is given by Equation (2.49) or Equation (2.50). For the V-shaped nanoantenna, the arm along $\hat{x}$ direction is labeled as $\Gamma_1$ and the other arm is labeled as $\Gamma_2$ meaning arm 1 and arm 2, respectively. In order to find the vector magnetic potential affecting arm 1 of this antenna, $\hat{x}$ and $\hat{y}$ directed components of the vector magnetic potential shall be found. Only the current on arm 2 creates a vector magnetic potential that has $\hat{x}$ component and flow direction of this current is chosen to be the $-\hat{x}$ direction as depicted in Figure 2.20. The vector magnetic potential due to this current is given as follows:

$$A_{1x} = \frac{\mu_o}{4\pi} \int_{-\frac{h}{2}}^{0} I(l') \frac{e^{-jkR_{rd}^V}}{R_{rd}^V} dl' \sin(\Delta) \tag{2.108}$$

where $R_{rd}^V$ is defined by Equation (2.109). $x$ and $y$ are the observation point coordinates. $l'$ is the source point and $\Delta$ is the opening angle of the antenna.

$$R_{rd}^V = \sqrt{a^2 + (y + l'\cos(\Delta))^2 + (x - l'\sin(\Delta))^2} \tag{2.109}$$

The derivative of the kernel $\frac{e^{-jkR_{rd}^V}}{R_{rd}^V}$ with respect to $x$ is given by Equation (2.53) if $R_{rd}^L$ is replaced by $R_{rd}^V$ and it should be evaluated at $x$ equals 0 since the source point is on the antenna. $\left(R_{rd}^V\right)'$ is given by Equation (2.110) for V-shaped nanoantenna.

$$\frac{\partial R_{rd}^V}{\partial x} = \frac{1/2 \times 2(x - l'sin\Delta)}{\sqrt{(a^2 + (y + l'cos\Delta)^2 + (x - l'sin\Delta)^2)}} = \frac{-l'\sin\Delta}{R_{rd}^V} \tag{2.110}$$

Using Equation (2.53) and Equation (2.110) in Equation (2.108), explicit expression for x component of the vector magnetic potential on arm 1 is obtained:

$$\frac{\partial A_{1x}}{\partial x} = \frac{\mu_o}{4\pi} \int_{-\frac{h}{2}}^{0} I(l') \frac{e^{-jkR_{rd}^V}}{\left(R_{rd}^V\right)^3} (1 + jkR_{rd}^V) l' dl' \sin(\Delta) \tag{2.111}$$

where $R_{rd}^V$ is given by Equation (2.107) if $y$ is replaced by $l$.

For the V-shaped nanoantenna, both of the currents on arm 1 and 2 creates vector magnetic potentials that have $\hat{y}$ directed components. Flow direction of the current on arm 1 is chosen to be plus $\hat{y}$ direction. The vector magnetic potential due to these currents on both arms is given as follows:

$$A_{1y} = \frac{\mu_o}{4\pi}\left(\int_0^{\frac{h}{2}} I(l')\frac{e^{-jkR_{rs}^V}}{R_{rs}^V}dl' + \int_{-\frac{h}{2}}^{0} I(l')\frac{e^{-jkR_{rd}^V}}{R_{rd}^V}dl'(-cos\Delta)\right) \tag{2.112}$$

where $R_{rs}^V$ is defined by Equation (2.57) if $L$ is replaced by $V$. $l'$ is the source point and its sign is positive as a result of the coordinate system choice. Note that $x$ is 0 on arm 1, hence source point is only represented by $y$.

In Figure 2.20, the orientation of the incident field is given with respect to the antenna symmetry axis. $\alpha$ is defined as the incidence angle and taken counter clockwise direction from the symmetry axis of the antenna. Incident field propagation direction is assumed to be out of page($+z$) direction. Boundary condition for arm 1 of V-shaped nanoantenna with the assumption of antenna being a perfect electric conductor is given as follows:

$$-E_{inc}\cos(\frac{\Delta}{2}+\alpha) = \frac{1}{jw\mu_o\varepsilon_o\varepsilon_r}\left[\left(\frac{\partial^2}{\partial y^2}+k^2\right)A_{1y} + \frac{\partial}{\partial y}\left(\frac{\partial A_{1x}}{\partial x}\right)\right] \tag{2.113}$$

The constants in Equation (2.113) can be rearranged as given in Equation (2.59). Then, the boundary condition for arm 1 can be written as follows:

$$\begin{aligned} &2kE_{inc}\cos(\frac{\Delta}{2}+\alpha) = \\ &\frac{j\eta}{2\pi}\left(\left[\frac{\partial^2}{\partial y^2}+k^2\right]\left[\int_0^{\frac{h}{2}} I(l')\frac{e^{-jkR_{rs}^V}}{R_{rs}^V}dl' + \int_{-\frac{h}{2}}^{0} I(l')\frac{e^{-jkR_{rd}^V}}{R_{rd}^V}dl'(-cos\Delta)\right]\right) + \\ &\frac{j\eta}{2\pi}\left(\frac{\partial}{\partial y}\int_{-\frac{h}{2}}^{0} I(l')\frac{e^{-jkR_{rd}^V}}{(R_{rd}^V)^3}(1+jkR_{rd}^V)l'dl'(\sin\Delta)^2\right) \end{aligned} \tag{2.114}$$

Rearranging Equation (2.114) and replacing variable $y$ with $l$, the following equation is obtained:

$$\begin{aligned} &2kE_{inc}\cos(\frac{\Delta}{2}+\alpha) = \\ &\frac{j\eta}{2\pi}\left(\left[\frac{\partial^2}{\partial l^2}+k^2\right]\left[\int_{-\frac{h}{2}}^{\frac{h}{2}} I(l')\kappa_1(l,l',\Delta)dl'\right]\right)+ \\ &\frac{j\eta}{2\pi}\left(\frac{\partial}{\partial l}\int_{-\frac{h}{2}}^{\frac{h}{2}} I(l')\kappa_2(l,l',\Delta)dl'\right) \end{aligned} \tag{2.115}$$

where $\kappa_1$ is the integral kernel of the integration that will be differentiated twice and given by Equation (2.116). $\kappa_2$ is the integral kernel of the integration that will be differentiated only once and given by Equation (2.117).

$$\kappa_1(l,l',\Delta) = \frac{e^{-jkR_{rs}^v}}{R_{rs}^v}H(l') + \frac{e^{-jkR_{rd}^v}}{R_{rd}^v}(-cos\Delta)H(-l') \tag{2.116}$$

where $H$ symbolizes the Heaviside function whose output is 1 when its input is positive. $R_{rs}^V$ is given by Equation (2.47).

$$\kappa_2(l,l',\Delta) = \frac{e^{-jkR_{rd}^v}}{{(R_{rd}^v)}^3}(1+jkR_{rd}^v)l'(sin\Delta)^2H(-l') \tag{2.117}$$

where $R_{rd}^V$ is given by Equation (2.107).

For arm 2, reference coordinate system is rotated for relatively easier derivation of the vector magnetic potentials as depicted in Figure 2.21. For this arm the only source of vector magnetic potential that has $x$ component is the current on arm 1. The vector magnetic potential due to this current is given by Equation (2.118).

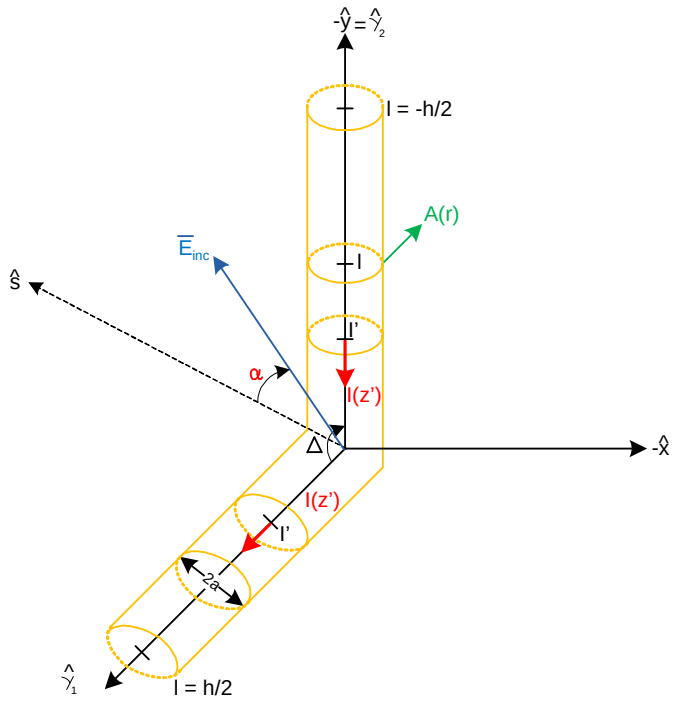


Figure 2.21: Depiction of the simplified geometry of V-shaped nanoantennas for arm 2.

$$A_x = \frac{\mu_o}{4\pi}\int_0^{\frac{h}{2}} I(l')\frac{e^{-jkR_{rd}^V}}{R_{rd}^V}dl'(sin\Delta) \tag{2.118}$$

where $R_{rd}^V$ is defined by the following equation. $x$ and $y$ are the observation point coordinates. $l'$ is the source point and its sign is positive as a result of the coordinate system choice. $\Delta$ is the opening angle of the antenna.

$$R_{rd}^V = \sqrt{a^2 + (y + l'\cos\Delta)^2 + (x - l'\sin\Delta)^2} \tag{2.119}$$

The derivative of the integral kernel of Equation (2.118) with respect to $x$ is given by the following equation and it should be evaluated for $x$ being equal to 0.

$$\frac{\partial}{\partial x}\frac{e^{-jkR_{rd}^V}}{R_{rd}^V} = \left(-jk\frac{e^{-jkR_{rd}^V}}{R_{rd}^V} - \frac{e^{-jkR_{rd}^V}}{(R_{rd}^V)^2}\right)(R_{rd}^v)' \tag{2.120}$$

The derivative of the effective distance is calculated for the case of $x$ being equal

to 0 and the result is given by the following equation:

$$\frac{\partial R_{rd}^V}{\partial x} = \frac{x - l' \sin\Delta}{\sqrt{a^2 + (x - l'\sin\Delta)^2 + (y + l'\cos\Delta)^2}} = -\frac{l'\sin\Delta}{R_{rd}^V} \tag{2.121}$$

Using Equation (2.120) and Equation (2.121) in Equation (2.118), the derivative of the $x$ component of the vector magnetic potential with respect to variable $x$ can be obtained as given in Equation (2.122). Effective distance is given by Equation (2.123) for the case of $x$ being equal to 0.

$$\frac{\partial A_{2x}}{\partial x} = \frac{\mu_o}{4\pi}\int_0^{\frac{h}{2}} I(l')\frac{e^{-jkR_{rd}^V}}{(R_{rd}^V)^3}(1 + jkR_{rd}^V)l'dl'\sin^2\Delta \tag{2.122}$$

$$R_{rd}^V = \sqrt{a^2 + (y + l'cos\Delta)^2 + (l'\sin\Delta)^2} \tag{2.123}$$

Both the current on arm 1 and 2 creates vector magnetic potentials that have $y$ components. The vector magnetic potential due to these currents is given by the following equation:

$$A_{2y} = \frac{\mu_o}{4\pi}\int_{-\frac{h}{2}}^{0} I(l')\frac{e^{-jkR_{rs}^V}}{R_{rs}^V}dl' + \frac{\mu_o}{4\pi}\int_0^{\frac{h}{2}} I(l')\frac{e^{-jkR_{rd}^V}}{R_{rd}^V}dl'(-cos\Delta) \tag{2.124}$$

where $R_{rs}^V$ is defined by the following equation while $R_{rd}^V$ is defined by Equation (2.123). $l'$ is the source point. Note that $x$ is 0 on arm 2, hence source point is only represented by $y$.

$$R_{rs}^V = \sqrt{a^2 + (y - l')^2} \tag{2.125}$$

Boundary condition for arm 2 with the assumption of antenna being a perfect electric conductor is given by the following equation:

$$E_{inc}\cos(\frac{\Delta}{2} - \alpha) = \frac{1}{jw\mu_o\varepsilon_o\varepsilon_r}\left[\left(\frac{\partial^2}{\partial y^2} + k^2\right)A_{2y} + \frac{\partial}{\partial y}\left(\frac{\partial A_{2x}}{\partial x}\right)\right] \tag{2.126}$$

The constants in Equation (2.126) can be re-arranged as follows.

$$\frac{1}{jw\mu_o\varepsilon_o\varepsilon_r}\frac{\mu_o}{4\pi} = -\frac{1}{2k}\frac{j\eta}{2\pi} \tag{2.127}$$

where $\eta$ is the effective intrinsic impedance of the homogeneous medium where the antenna stands. Then, the boundary condition for arm 2 can be written as

follows:

$$
\begin{aligned}
&-2kE_{inc}\cos(\frac{\Delta}{2}-\alpha)= \\
&\frac{j\eta}{2\pi}\left(\left[\frac{\partial^2}{\partial y^2}+k^2\right]\left(\int_{-\frac{h}{2}}^{0} I(l')\frac{e^{-jkR_{rs}^V}}{R_{rs}^V}dl'-\int_{0}^{\frac{h}{2}} I(l')\frac{e^{-jkR_{rd}^V}}{R_{rd}^V}dl'\cos\Delta\right)\right)+ \\
&\frac{j\eta}{2\pi}\left(\frac{\partial}{\partial y}\int_{0}^{\frac{h}{2}} I(l')\frac{e^{-jkR_{rd}^V}}{(R_{rd}^V)^3}(1+jkR_{rd}^V)l'dl'\sin^2\Delta\right)
\end{aligned}
\tag{2.128}
$$

Rearranging Equation (2.128) and replacing variable $y$ with $l$, the following equation is obtained:

$$
\begin{aligned}
&-2kE_{inc}\cos(\frac{\Delta}{2}-\alpha)= \\
&\frac{j\eta}{2\pi}\left(\left[\frac{\partial^2}{\partial l^2}+k^2\right]\int_{-\frac{h}{2}}^{\frac{h}{2}} I(l')\kappa_3(l,l',\Delta)dl'\right)+ \\
&\frac{j\eta}{2\pi}\left(\frac{\partial}{\partial l}\int_{-\frac{h}{2}}^{\frac{h}{2}} I(l')\kappa_4(l,l',\Delta)dl'\right)
\end{aligned}
\tag{2.129}
$$

where $\kappa_3$ is the integral kernel of the integration that will be differentiated twice and given by Equation (2.130). $\kappa_4$ is the integral kernel of the integration that will be differentiated only once and given by Equation (2.131).

$$
\kappa_3(l,l',\Delta)=\frac{e^{-jkR_{rs}^v}}{R_{rs}^v}H(-l')-\frac{e^{-jkR_{rd}^v}}{R_{rd}^v}H(l')cos\Delta \tag{2.130}
$$

where $H$ symbolizes the Heaviside function whose output is 1 when its input is positive. $R_{rs}^V$ is given by Equation (2.47).

$$
\kappa_4(l,l',\Delta)=\frac{e^{-jkR_{rd}^v}}{(R_{rd}^v)^3}(1+jkR_{rd}^v)l'(sin\Delta)^2H(l') \tag{2.131}
$$

where $R_{rd}^V$ is given by Equation (2.107).

Combining the boundary conditions for both arms of the V-shaped nanoantenna, one can obtain the following equation:

$$\begin{aligned} &2kE_{inc}\left[\cos(\frac{\Delta}{2}+\alpha)H(l)-\cos(\frac{\Delta}{2}-\alpha)H(-l)\right]= \\ &\frac{j\eta}{2\pi}\left(\left[\frac{\partial^2}{\partial l^2}+k^2\right]\int\limits_{-\frac{h}{2}}^{\frac{h}{2}} I(l')\kappa_1(l,l')dl'\right)+ \\ &\frac{j\eta}{2\pi}\left(\frac{\partial}{\partial l}\int\limits_{-\frac{h}{2}}^{\frac{h}{2}} I(l')\kappa_2(l,l')dl'\right) \end{aligned} \tag{2.132}$$

Where $\kappa_1$ and $\kappa_2$ are given by Equation (2.133) and Equation (2.134).

$$\begin{aligned} &\kappa_1(l,l',\Delta)=\frac{e^{-jkR_{rs}^V}}{R_{rs}^V}\left[H(l)H(l')+H(-l)H(-l')\right]- \\ &\frac{e^{-jkR_{rd}^V}}{R_{rd}^V}\left[H(l)H(-l')+H(-l)H(l')\right]\cos\Delta \end{aligned} \tag{2.133}$$

where $R_{rs}^V$ is given by Equation (2.47).

$$\kappa_2(l,l',\Delta)=(1+jkR_{rd}^V)\frac{e^{-jkR_{rd}^V}}{(R_{rd}^V)^3}l'\sin^2\Delta\left[H(l)H(-l')+H(-l)H(l')\right] \tag{2.134}$$

where $R_{rd}^V$ is given by Equation (2.107).

#### 2.2.3.2 MoM Numerical Solution

The Pocklington type integral equation Equation (2.132) does not have an analytical solution, hence numerical solutions must be implemented to solve this equation. In this subsection, MoM is applied for solving this equation.

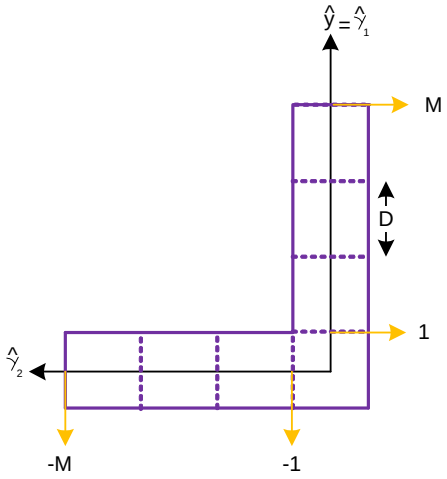


Figure 2.22: Current discretization on a V-shaped nanoantenna.

The antenna is discretized into $N$ $(2 \times M)$ parts such that the curvilinear variable $l'$ is sampled at points $\{-M, -M+1, ..., -1, 1, ..., M-1, M\}$. Figure 2.22 contains a schematic representing the discretization of the antenna. $D$ is the sampling period which is given by the following simple relation:

$$D = \frac{h}{N-1} \tag{2.135}$$

After discretization the integration parts of the Equation (2.132) are represented by discrete functions $V^1[l_n]$ and $V^2[l_n]$ which are given as follows:

$$V^{(i)}[l_n] = \frac{j\eta}{2\pi} \left\{ \int_{-\frac{h}{2}}^{\frac{h}{2}} I(l')\kappa^{(i)}(l_n, l', \Delta)dl' \right\} \tag{2.136}$$

The current distribution on the antenna is expanded into a sum of weighted Dirac functions:

$$I(l') = \sum_{m=-M}^{M} I_m \delta(l' - l_m) \tag{2.137}$$

When this weighted distribution is used in Equation (2.136), the following relation is obtained:

$$V_n{}^{(i)} = \sum_{m=-M}^{M} \kappa_{nm}^{(i)} I_m \tag{2.138}$$

$\kappa_{nm}^{(1)}$ and $\kappa_{nm}^{(2)}$ are given by the following equations:

$$\begin{aligned}\kappa_{nm}^{(1)} = \frac{j\eta}{2\pi}\frac{e^{-jkR_{rs}^V}}{R_{rs}^V}\left[H(l_n)H(l_m) + H(-l_n)H(-l_m)\right] - \\ \frac{j\eta}{2\pi}\frac{e^{-jkR_{rd}^V}}{R_{rd}^V}\cos\Delta\left[H(l_n)H(-l_m) + H(-l_n)H(l_m)\right]\end{aligned} \tag{2.139}$$

$$\kappa_{nm}^{(2)} = \frac{j\eta}{2\pi}(1 + jkR_{rd}^V)\frac{e^{-jkR_{rd}^V}}{(R_{rd}^V)^3}l_m\sin^2\Delta\left[H(-l_n)H(l_m) + H(l_n)H(-l_m)\right] \tag{2.140}$$

First and second order derivatives of $V^{(i)}[l_n]$ are given by Equation (2.141) and Equation (2.142) where finite difference schemes are used to convert derivatives in the integral equation into sums.

$$\frac{\partial^2}{\partial l^2}V^1(l) = \frac{V_{n+1}^1 - 2V_n^1 + V_{n-1}^1}{D^2} \tag{2.141}$$

$$\frac{\partial}{\partial l}V^2(l) = \frac{V_{n+1}^2 - V_{n-1}^2}{2D} \tag{2.142}$$

Equation (2.132) can be rewritten after discretization by using Equation (2.141) and Equation (2.142) after rearranging some of the constants such as $d = 2k$ and $\alpha = 1 - \frac{k^2D^2}{2}$:

$$\frac{1}{D^2}\left(V_{n+1}^1 - 2\alpha V_n^1 + V_{n-1}^1\right) + \frac{1}{2D}(V_{n+1}^2 - V_{n-1}^2) = dE_n \tag{2.143}$$

where $E_n$ is the discretized (normalized) incident field projection on the antenna and given by the following equation:

$$E_n = \cos(\frac{\Delta}{2} + \alpha)H(l_n) - \cos(\frac{\Delta}{2} - \alpha)H(-l_n) \tag{2.144}$$

Now, the discrete form of the Pocklington type integral equation can be written as follows:

$$\left[\mathrm{A}\kappa^{(1)} + C\kappa^{(2)}\right]I = QdE \tag{2.145}$$

where $A$ is given by Equation (2.146), $C$ is given by Equation (2.147) and $Q$ is given by Equation (2.148).

$$A = \frac{1}{D^2}\begin{bmatrix} 0 & 0 & 0 & 0 & 0 & \dots & 0 \\ 1 & -2\alpha & 1 & 0 & 0 & \dots & 0 \\ 0 & 1 & -2\alpha & 1 & 0 & \dots & 0 \\ \vdots & \ddots & \ddots & \ddots & \ddots & \ddots & \vdots \\ 0 & \dots & 0 & 1 & -2\alpha & 1 & 0 \\ 0 & \dots & 0 & 0 & 1 & -2\alpha & 1 \\ 0 & \dots & 0 & 0 & 0 & 0 & 0 \end{bmatrix} \tag{2.146}$$

$$C = \frac{1}{2D}\begin{bmatrix} 0 & 0 & 0 & 0 & 0 & \dots & 0 \\ -1 & 0 & 1 & 0 & 0 & \dots & 0 \\ 0 & -1 & 0 & 1 & 0 & \dots & 0 \\ \vdots & \ddots & \ddots & \ddots & \ddots & \ddots & \vdots \\ 0 & \dots & 0 & -1 & 0 & 1 & 0 \\ 0 & \dots & 0 & 0 & -1 & 0 & 1 \\ 0 & \dots & 0 & 0 & 0 & 0 & 0 \end{bmatrix} \tag{2.147}$$

$$Q = \begin{bmatrix} 0 & 0 & 0 & 0 & 0 & \dots & 0 \\ 0 & 1 & 0 & 0 & 0 & \dots & 0 \\ 0 & 0 & 1 & 0 & 0 & \dots & 0 \\ \vdots & \ddots & \ddots & \ddots & \ddots & \ddots & \vdots \\ 0 & \dots & 0 & 0 & 1 & 0 & 0 \\ 0 & \dots & 0 & 0 & 0 & 1 & 0 \\ 0 & \dots & 0 & 0 & 0 & 0 & 0 \end{bmatrix} \tag{2.148}$$

All of the matrices used in Equation (2.91) are $N \times N$ square matrices. First and last rows of these matrices are purposefully added as zero vectors for making these matrices square. However, both of these rows and first and last columns of these matrices can be removed since the first and last elements of the current vector $(\overline{I})$ must be 0. This situation is a consequence of the end conditions which state that the current distribution must vanish at the physical ends of the antenna. After removing these rows and columns, current distribution on the V-shaped nanoantenna can be find using Equation (2.149) where $I$ is the reduced current distribution and zeros must be added as the first and last elements. $Z$ is given by Equation (2.150)

$$I = dZ^{-1}E \tag{2.149}$$

$$Z = A\kappa Q \tag{2.150}$$

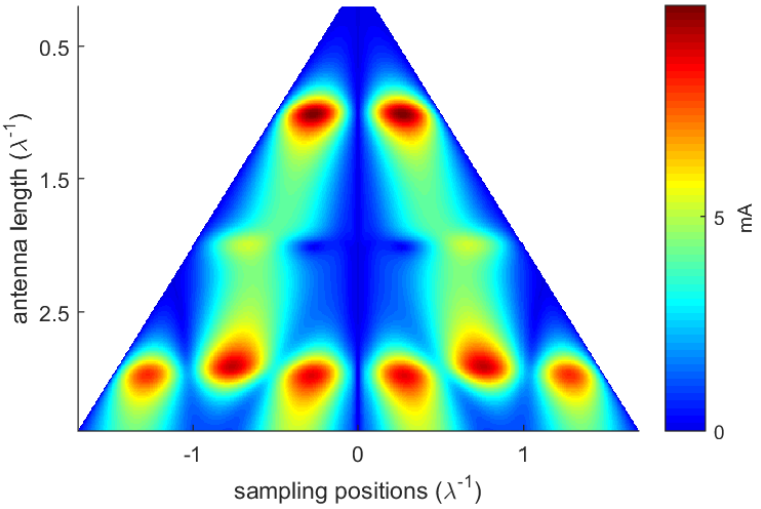


Figure 2.23: Amplitudes of current distributions on V-shaped nanoantennas with symmetric excitation.

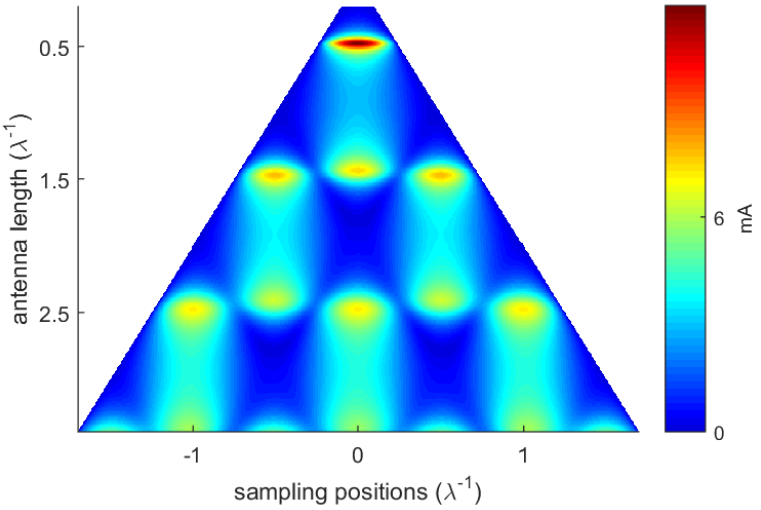


Figure 2.24: Amplitudes of current distributions on V-shaped nanoantennas with antisymmetric excitation.

For finding the current distribution on a V-shaped nanoantenna using MoM, we first find the projection of the incident field on the V-shaped nanoantenna. Then, we calculate the coefficients such as $\alpha$ and $D$. Using these coefficients matrix $A$ and $C$ are calculated. Then, the impedance matrix $Z_1$ and $Z_2$ are calculated using the reduced kernels $R_r d$ and $R_r s$ and multiplied by $A$ and $C$, respectively. Finally, the inverse of the summation of the multiplication of $A$ and $Z_1$ and the multiplication of $C$ and $Z_2$ is multiplied by the vector corresponding to the projection of the incident field on the V-shaped nanoantenna for obtaining the current distribution.

In Figure 2.23 amplitudes of the current distributions on V-shaped nanoantennas of varying length and fixed opening angle of $\frac{\pi}{4}$ are provided for the case of symmetric excitation. In the symmetric excitation, the polarization of the incident field has the same direction of the antenna symmetry axis. For this excitation, both arms of the antennas act as rod antennas of length $\frac{h}{2}$ and their resonance condition occur proportional to this length.

In Figure 2.24 amplitudes of the current distributions on V-shaped nanoantennas of varying length and fixed opening angle of $\frac{3\pi}{4}$ are provided for the case of antisymmetric excitation. In the antisymmetric excitation, the polarization of the incident field has a direction that is orthogonal to the antenna symmetry axis. For this excitation, the antennas act similar to rod antennas of length $h$ and their resonance condition occur proportional to this length. The antenna lengths are varied from 0.25 to 3.0 wavelength in obtaining the data in these figures with MoM simulations. The phase of the current distributions are also provided in Figure 2.25 and Figure 2.26 for the cases of symmetric and antisymmetric excitations.

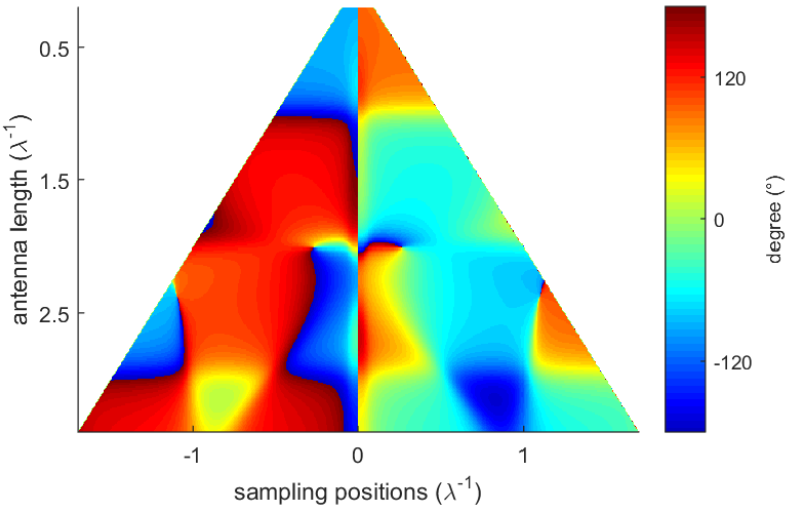


Figure 2.25: Phase of current distribution on a V-shaped nanoantenna with symmetric excitation.

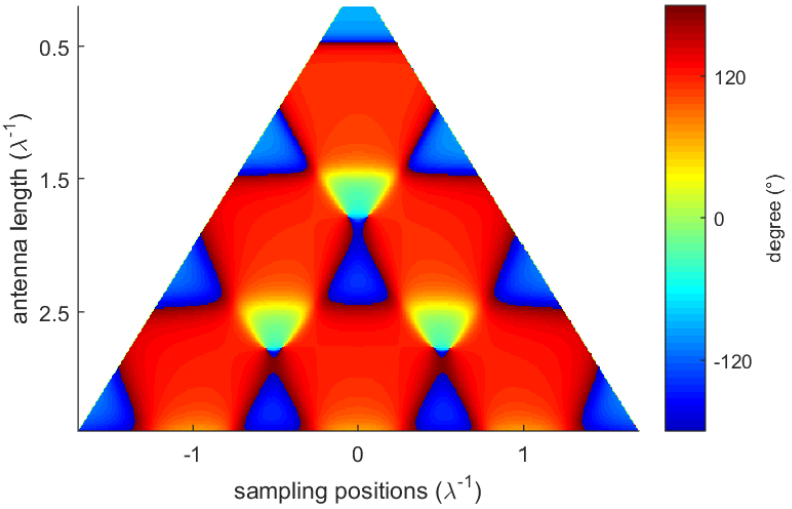


Figure 2.26: Phase of current distribution on a V-shaped nanoantenna with antisymmetric excitation.

In order to account for the finite conductivity of the metals, the boundary condition given in Equation (2.16) should be modified as follows:

$$\hat{t} \cdot [E_{scat} + E_{inc}] = \frac{1-j}{2\pi a}\sqrt{\frac{\mu_0 \omega}{2\sigma}} I \tag{2.151}$$

where $a$ is the antenna radius, $\mu_0$ is the permeability, $\omega$ is the radial frequency of the incident field and $\sigma$ is the AC conductivity of the metal. AC conductivity of the metal can be calculated from the DC conductivity of the metal when the frequency of interest is given and the electron relaxation lifetime of the metal is known.

#### 2.2.3.3 Radiation into Farfield

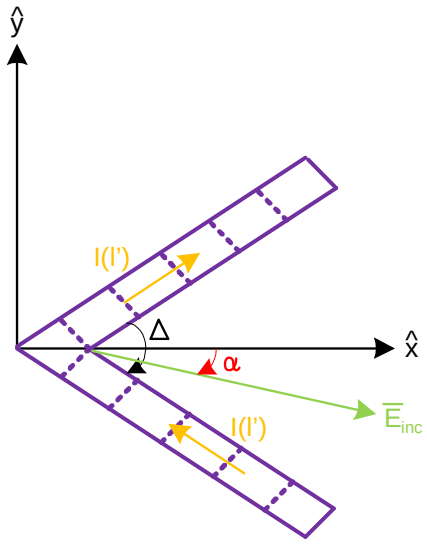


Figure 2.27: Source of scattering depiction on a V-shaped nanoantenna.

Finding the scattered fields of a metallic V-shaped nanoantenna using MoM is a problem that consists of two parts. Obtaining the current distribution along the antenna for a known incident field is the first part of this problem. For the second part, this current distribution should be re-radiated in order to find the scattered fields. In this subsection, solution to this part of the problem is provided.

The far-field radiation vector is defined as the three-dimensional spatial Fourier

transform of the current density [86] and is given by Equation (2.152).

$$F(\overline{k}) = \int_V J(r')e^{j\overline{k}\cdot\overline{r'}}d^3r' \tag{2.152}$$

where $J(r')$ is the current density on the antenna. This quantity depends on the wavenumber and the directional unit vector $\hat{r}$ which is completely defined by the spherical coordinate angles $\theta$ and $\phi$. For a thin-linear antenna, current density can be expressed as follows:

$$\begin{aligned} J(r) = I(l')H(l')\left[\hat{x}\cos(\frac{\Delta}{2})\delta(y)\delta(z) + \hat{y}\sin(\frac{\Delta}{2})\delta(x)\delta(z)\right] + \\ I(l')H(-l')\left[\hat{x}(-\cos(\frac{\Delta}{2}))\delta(y)\delta(z) + \hat{y}\sin(\frac{\Delta}{2})\delta(x)\delta(z)\right] \end{aligned} \tag{2.153}$$

where $\delta(x)$, $\delta(y)$ and $\delta(z)$ are the dirac functions of variable $x$, $y$ and $z$, respectively while $I(l')$ is the current distribution. Wavevector $\overline{k}$ is expressed in the spherical coordinate system as follows:

$$\overline{k} = k\hat{r} = k(\hat{x}\cos\phi sin\theta + \hat{y}\sin\phi sin\theta + \hat{z}\cos\theta) \tag{2.154}$$

Then, $\bar{k}\cdot\bar{r}' = (\frac{2\pi}{\lambda}\hat{r})\cdot(l'\hat{l}) = 2\pi\frac{l'}{\lambda}(\hat{r}\cdot\hat{l})$ is given as follows:

$$\bar{k}\cdot\bar{r}' = 2\pi\frac{l'}{\lambda}\sin\theta\left\{H(-l')(-cos(\frac{\Delta}{2}+\phi)) + H(l')\cos(\frac{\Delta}{2}-\phi)\right\} \tag{2.155}$$

For an $x$ directed antenna standing on top of a semiconductor dielectric interface, $\theta$ electric field component is given by Equation (2.156) and $\phi$ electric field component is given by Equation (2.157)( [87]). For a $y$ directed antenna $\cos\phi$ terms should be replaced by $\sin\phi$ terms and $\sin\phi$ terms should be replaced by $-\cos\phi$ terms.

$$\begin{aligned} E_\theta = \left[\frac{(\cos\theta)^2}{\cos\theta + \sqrt{(n^2-(\sin\theta)^2)}}\right]\cos\phi \\ -\left[(\sin\theta)^2\cos\theta\frac{\cos\theta - \sqrt{(n^2-(\sin\theta)^2)}}{n^2\cos\theta + \sqrt{(n^2-(\sin\theta)^2)}}\right]\cos\phi \end{aligned} \tag{2.156}$$

$$E_\phi = -\frac{\cos\theta}{\cos\theta + \sqrt{(n^2-(\sin\theta)^2)}}\sin\phi \tag{2.157}$$

For designing metasurfaces using V-shaped metallic antennas, their far-field amplitude and phase responses along the incident field's wavevector direction should be considered. Hence, $\theta$ and $\phi$ used in Equation (2.155), Equation (2.156) and Equation (2.157) can be set to 0. Then, both of the electric field components along the $\hat{x}$ and $\hat{y}$ directions reduce to $\frac{1}{1+n}$. Also, $\bar{k} \cdot \bar{r}'$ diminishes for $\theta$ equals 0.

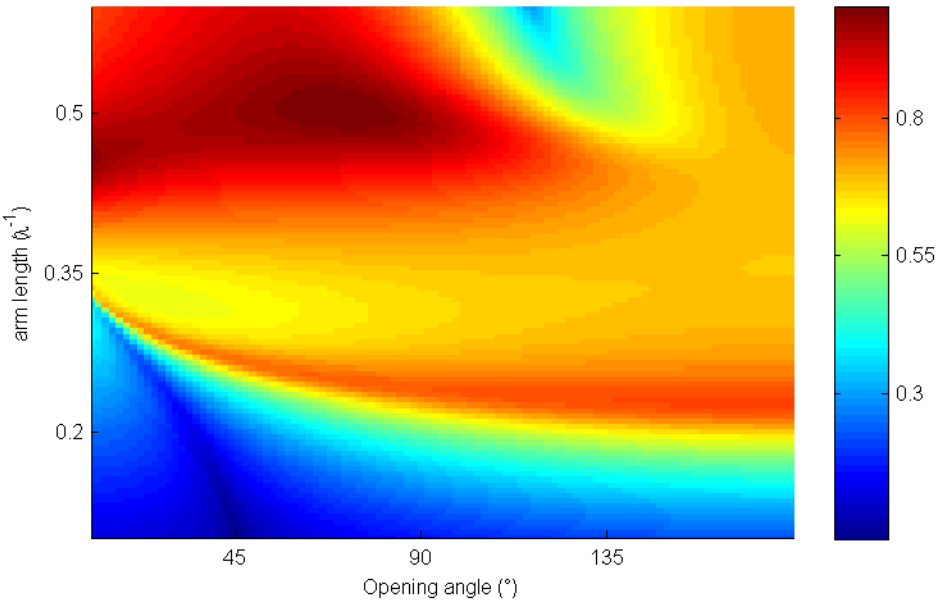


Figure 2.28: Scattered field amplitudes of V-shaped nanoantennas.

Far field amplitudes and phase shifts of V-shaped nanoantennas having varying lengths and opening angles are shown in Figure 2.28 and Figure 2.29, respectively. In order to obtain these data, V-shaped nanoantennas are excited by electric field polarized at a 45° angle with respect to antenna symmetry axis and the scattered field along the normal direction to the antenna plane is calculated. Only the cross-polarized (with respect to incident field) scattered field is considered. Lengths of antennas are varied between 0.2 and 1.1 effective wavelength so that it is possible to excite both resonance modes for most of the antennas. Antennas are considered to be fabricated from gold when considering the effect of finite conductivity of real metals. Scattered field amplitudes of V-shaped nanoantennas maximized when both arm lengths have length close to 0.5 effective wavelength. However, antennas having scattered field amplitudes greater than 0.6 of the maximum scattering field

amplitude can also be used to design metasurfaces up to a certain performance. Scattered field phase shifts of these antennas cover the whole $0 - 2\pi$ range as seen in Figure 2.29. Therefore, V-shaped nanoantennas can be used to design metasurfaces.

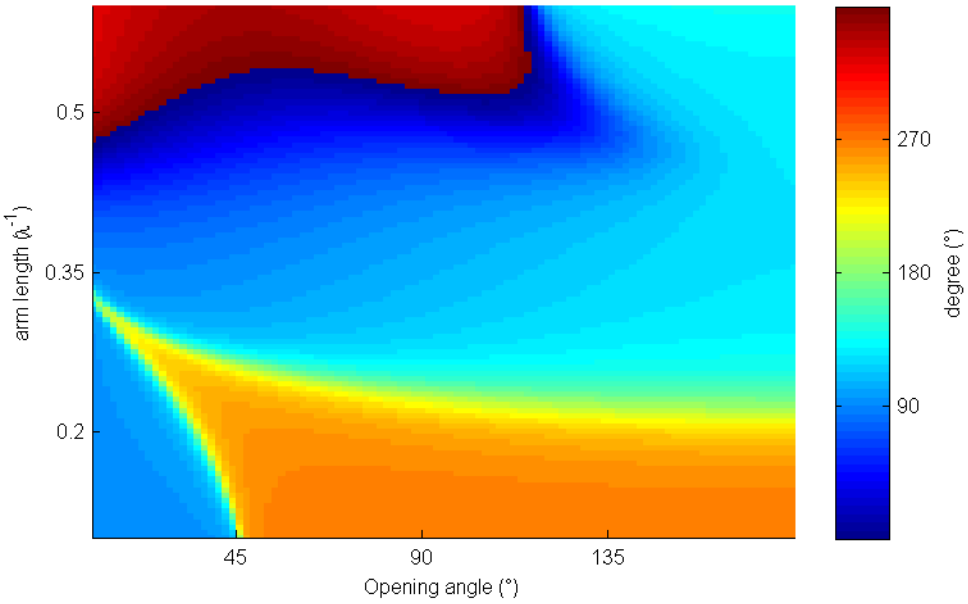


Figure 2.29: Scattered field phase shifts of V-shaped nanoantennas.

#### 2.2.3.4 FDTD Numerical Solution

For understanding the general behavior of V-shaped nanoantennas, probing a large parameter space in a relatively shorter amount of time and obtaining rough results, a simplified model can be simulated with MoM as done in the previous subsections. However, after the rough scanning stage, precise behavior of antennas is required for designing metasurfaces with optimum performance. For this part of the problem, full wave simulations can be used with a much more realistic model having 3D geometry.

In this part, Lumerical FDTD is used to perform full wave simulations of gold V-shaped nanoantennas that are placed onto a silicon substrate. Before

determining the initial value for varying the length and cross-section of the V-shaped nanoantennas, effective wavelength for this media should be considered. Effective wavelength is given by Equation (2.14) for the visible and infrared region of the electromagnetic spectrum. For excitation wavelength of 1550 nm and radii of 20 nm, 50 nm and 100 nm, effective wavelength varies between 800 nm and 1200 nm for rod antennas standing in vacuum [88]. Therefore, total length of a V-shaped nanoantenna can be close to 800 nm if it is standing in vacuum. However, since the V-shaped nanoantennas are placed on a silicon substrate, effective refractive index is close to 2.6 [52]. So, total length close to 300 can be considered for the resonance condition.

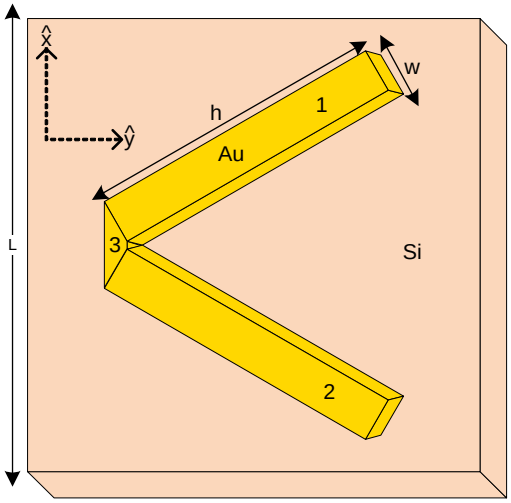


Figure 2.30: Geometry of V-shaped nanoantennas modeled for Lumerical FDTD simulations.

For modeling a realistic V-shaped nanoantenna geometry, two rectangular prisms of gold (gold colored blocks 1 and 2) that have arm lengths $h$ and width $w$ are connected by a triangular prism of gold (gold colored block 3) as depicted in Figure 2.30. Guided by our MoM analysis results obtained in the previous subsections, total length of V-shaped nanoantennas is varied between 100 nm and 400 nm while the opening angle is changed between 30° and 180°. The width $w$ and thickness $d$ is held fixed at 50 nm. For each V-shaped nanoantenna, a silicon substrate having square cross-section of edge length $L$ is used. This edge length $L$ should be long enough for avoiding mutual coupling of antennas when antennas placed nearby to built metasurfaces and it should also be as short as

possible for increasing the efficiency of designed metasurface. After several simulation runs, we obtained the value of 300 nm to be used as the edge length. Then, this V-shaped nanoantenna on a silicon substrate is excited by a monochromatic (1550 nm) total field scattered field (TFSF) source at 1550 nm from the silicon substrate. This TFSF source is a special kind of plane wave source of Lumerical FDTD that is used for scattering simulations and it simplifies the splitting process of the incident and scattered fields by just keeping the incident field inside its boundaries. A frequency domain monitor is placed just above this TFSF source boundary for recording the near scattered fields. Then, far field transformation functions are used to calculate the farfield amplitude and phase responses of these antennas along the desired directions. The polarization direction of the TFSF source is chosen to be $+45^{\circ}$ with respect to $x$ axis shown in the Figure 2.30 so that it is possible to excite different resonance modes (ones that are parallel to the symmetry axis of the antenna and ones that are perpendicular to this symmetry axis). The recorded and far-field transformed scattered field has perpendicular polarization direction to this incident field.

Table 2.1: Length and opening angle of modeled V-shaped nanoantennas

| Antenna Type | Arm Length ($nm$) | Opening Angle ($^{\circ}$) | Axis Orien. ($^{\circ}$) |
|---|---|---|---|
| 1 | 180 | 79 | -45 |
| 2 | 140 | 68 | -45 |
| 3 | 130 | 104 | -45 |
| 4 | 85 | 175 | -45 |
| 5 | 180 | 79 | 45 |
| 6 | 140 | 68 | 45 |
| 7 | 130 | 104 | 45 |
| 8 | 85 | 175 | 45 |

In Table 2.1, length and opening angles of modeled V-shaped nanoantennas are given. Since, our aim is to find a set of V-shaped nanoantennas that cover full $0 - 2\pi$ range by their phase shift responses, we can first find a group of antennas that cover $0 - \pi$ range and then rotate this group by $90^{\circ}$. Therefore, last four of the antennas in Table 2.1 are just $90^{\circ}$ rotated replicas of the first four antennas. The phase shift and scattering amplitudes of these antennas are provided in Table 2.2.

Table 2.2: Far-field responses of modeled V-shaped nanoantennas

| Antenna Type | Phase Shift (°) | Scat. Ampl. (a.u.) |
|---|---|---|
| 1 | 2 | 0.92 |
| 2 | 55 | 0.85 |
| 3 | 98 | 0.73 |
| 4 | 140 | 1.00 |
| 5 | 182 | 0.92 |
| 6 | 235 | 0.85 |
| 7 | 278 | 0.73 |
| 8 | 320 | 1.00 |

## 2.3 Dielectric Nanoantennas

Pioneering studies on metasurfaces focused on metallic nanoantennas [9, 13, 14, 17, 21, 25, 27, 46, 52] for designing metasurfaces. However, absorption losses of metals and cross-polarization scheme required by metallic nanoantennas such as V-shaped nanoantennas cause efficiency problems in metallic metasurfaces that are designed to be used in transmittance mode as mentioned in Section 2.2. Because of this phenomena, practical usage of metallic metasurfaces is limited to reflectance mode optical components.

Dielectric nanoantennas emerged as alternatives to metallic nanoantennas for designing and realizing metasurfaces. Besides the primary advantage of lack of absorption losses, ease of integration with electronics and the possibility of manufacturing by proven semiconductor fabrication technologies favor the dielectric metasurfaces over metallic counterparts when manufacturing requirements are considered. Furthermore, it has been recently shown that high efficiency transmission mode optical components such as ultra-thin gratings, lenses and axicons can be realized by patterning sub-wavelength thick dielectric materials such as silicon [18].

### 2.3.1 FDTD Numerical Solution

Dielectric nanoantennas made from high (¿2.0) refractive index material can show strong Mie-type scattering resonances similar to metallic nanoantennas [89, 90].

For example, silicon nanowires show this type of resonance when their circumference is an integral number of times the incident light's wavelength inside silicon [91]. This resonance condition is given by the following equation:

$$m\frac{\lambda_0}{n} \approx 2\pi r \tag{2.158}$$

where m is a positive integer, $\lambda_0$ is the wavelength of incident light in free space and r is the radius of silicon nanowire. In addition to the electric dipole resonance inside high-refractive index dielectric materials, there can also exist a magnetic dipole resonance depending on the orientation and localization of the electric field [92, 93]. These two resonances can be used to satisfy the 0-to-2$\pi$ phase shift coverage requirement similar to the utilization of orthogonal modes occurring in V and L-shaped metallic nanoantennas. Besides the phase coverage issue, the primary interest in dielectric nanoantennas is the opportunity of increasing device efficiency. In order to provide this, both of the resonance modes should be excited with similar amplitudes and phases so that their far field contributions can interfere constructively in the forward direction. This condition was predicted theoretically for spherical particles in first Kerker's condition [94]. Recently, almost zero back scattering was experimentally demonstrated using this type of dielectric nanoparticles by spectrally overlapping electric and magnetic dipole resonances [95, 96]. For silicon nanodisks (which has a diameter that is larger than its height), this zero backscattering condition is satisfied for a diameter to height ration of 2 [66, 67]. For example, for a design wavelength of 3.6 $\mu m$, the diameter of the nanodisk can be around 1300 nm while its height should be close to 600 nm.

For designing silicon nanodisks that can perform as dielectric nanoantennas used to build metasurfaces, a design wavelength of 3.6 $\mu m$ was selected. Then, using the refractive index of silicon at this wavelength in Equation (2.158), a starting point for nanodisk diameter is determined as 1300 nm. After this, the nanodisk height was chosen as 600 nm. As the substrate, silica was chosen due to its high transmission in the wavelength of interest and its compatibility with silicon. For modeling this geometry Lumerical FDTD was used.

### 2.3.2 Radiation into Farfield

For finding a suitable dielectric nanoantenna set from the proposed design of silicon nanodisks on silica, its farfield scattering amplitudes and phases should be analyzed. Moreover, its transmission efficiency should be obtained for assessing its contribution to device efficiency. In order to obtain these characteristics of silicon nanodisks, full wave simulations were performed using Lumerical FDTD. A simulation region that spanned a volume of $L$ nm x $L$ nm x 5000 nm with a homogeneous refractive index that matches the silica's refractive index in the light source's wavelength was used. $L$ is the size of the axial lengths of the simulation region and chosen as a design parameter in order to maximize transmission without introducing mutual coupling between silicon nanodisks. A monochromatic plane wave source that has wavelength varied between 3.0 $\mu m$ and 5.0 $\mu m$ from simulation to simulation was used to excite the silicon nanodisk from a point that is close to the bottom of the simulation region. A nearfield monitor was used to record the scattered and transmitted field from the silicon nanodisk and placed at a point close to the top of the simulation region. The diameter of the silicon nanodisk was varied between 500 nm to 2000 nm while its diameter was varied between 250 $nm$ to 1000 $nm$. Also, $L$ was varied between 1200 nm to 2400 nm. After probing this parameter space, a suitable dielectric nanoantenna set was obtained for the design wavelength of $3.2\mu m$ and for $L$ being equal to 1800 nm.

Far field amplitude and phase shift responses of the silicon nanodisks are given as a function of the nanodisk diameter for the fixed designed height of 550 nm in Figure 2.31. In the inset of this figure, depiction of the silicon nanodisk's geometry is provided. As seen in this figure, $0 - to - 2\pi$ phase shift coverage is satisfied with an almost uniform amplitude response. So, these antennas can also be used as building blocks of metasurfaces.

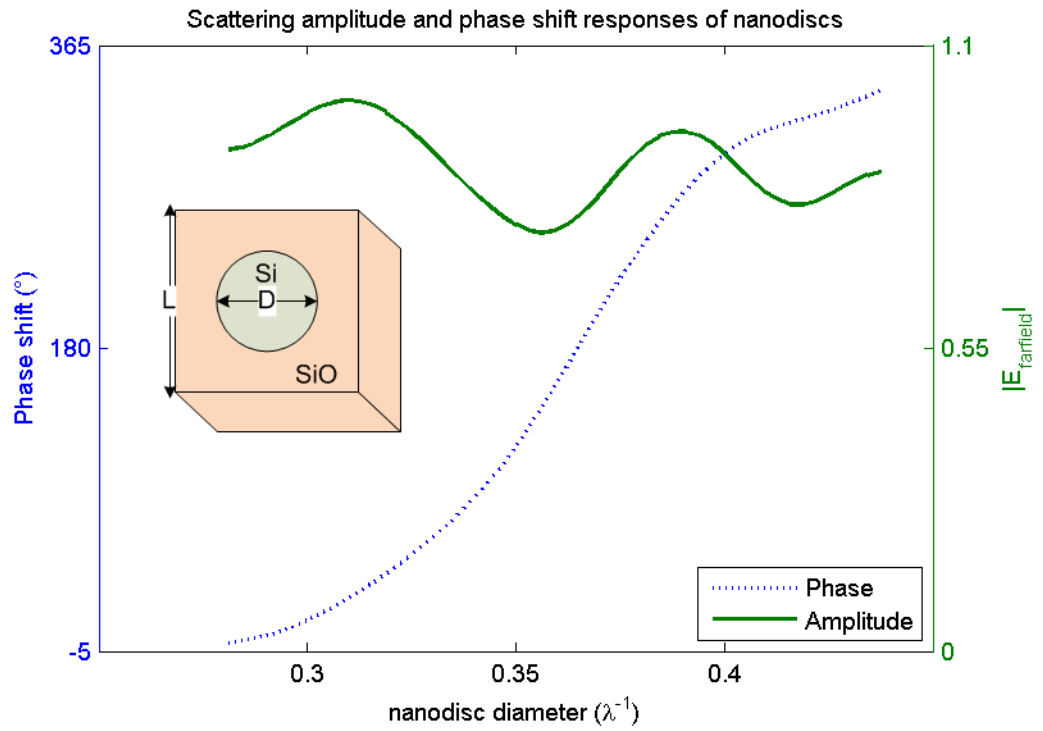


Figure 2.31: Amplitude and phase responses of far-field scattered from Si nanodisks.

For obtaining the transmission efficiency of silicon nanodisks, a similar simulation scenario was used. The only difference was the replacement of near field monitor by a power transmission monitor. For comparing the transmission efficiency to that of the metallic nanoantennas, gold V-shaped nanoantennas were also modeled and full wave simulations were also performed for them. Maximum efficiency that was obtained by using gold V-shaped nanoantennas was less than 11%. The far field characteristics' and transmission efficiencies of a set of silicon nanodisks that can be used to realize transmission mode dielectric metasurfaces is provided in Table 2.3. As seen in this table, the transmission efficiencies of silicon nanodisks is far more better than that of the V-shaped gold antennas. It can even reach very close to zero backscattering when the first Kerker condition is satisfied. The main reason for this very efficient transmission is the lack of absorption losses occurring in metallic nanoantennas. Therefore, these silicon nanodisks can be used to replace metallic counterparts for realizing high efficiency transmission mode metasurfaces that can perform as optical components.

Table 2.3: Farfield characteristics and transmission efficiency of silicon nanodisks

| Diameter (nm) | Phase shift (°) | Amplitude (a.u.) | Transmission (%) |
|---|---|---|---|
| 1240 | 35 | 0.94 | 96 |
| 1200 | 347 | 0.87 | 83 |
| 1160 | 295 | 0.77 | 65 |
| 1130 | 256 | 0.77 | 65 |
| 1090 | 214 | 0.82 | 75 |
| 1020 | 167 | 1.00 | 98 |
| 900 | 125 | 0.92 | 90 |
| 1320 | 79 | 0.82 | 75 |

# Chapter 3

# Metasurface Design Methodology

Metasurfaces consist of dense two-dimensional arrangements of optically thin resonators. By changing the size, shape and orientation of optically thin resonators, their amplitude and phase shift responses can be tuned. This controllability paves the way of achieving desired optical functionalities by designing the arrangement of these resonators.

This chapter consist of two sections. In Section 1, general procedure for designing metasurfaces is explained in detail. Then, using this procedure, several metasurface designs including lenslet arrays and parabolic mirrors are provided in Section 2.

## 3.1 General Procedure

The procedure for designing a metasurface is depicted in Figure 3.1. A good starting point is the determination of the central design wavelength. After fixing this parameter, size range of the optical resonators can be roughly determined depending on the resonance condition. Operational bandwidth of the metasurface can be used as an input at this step. For example, midpoint of this bandwidth can be picked as the central design wavelength.

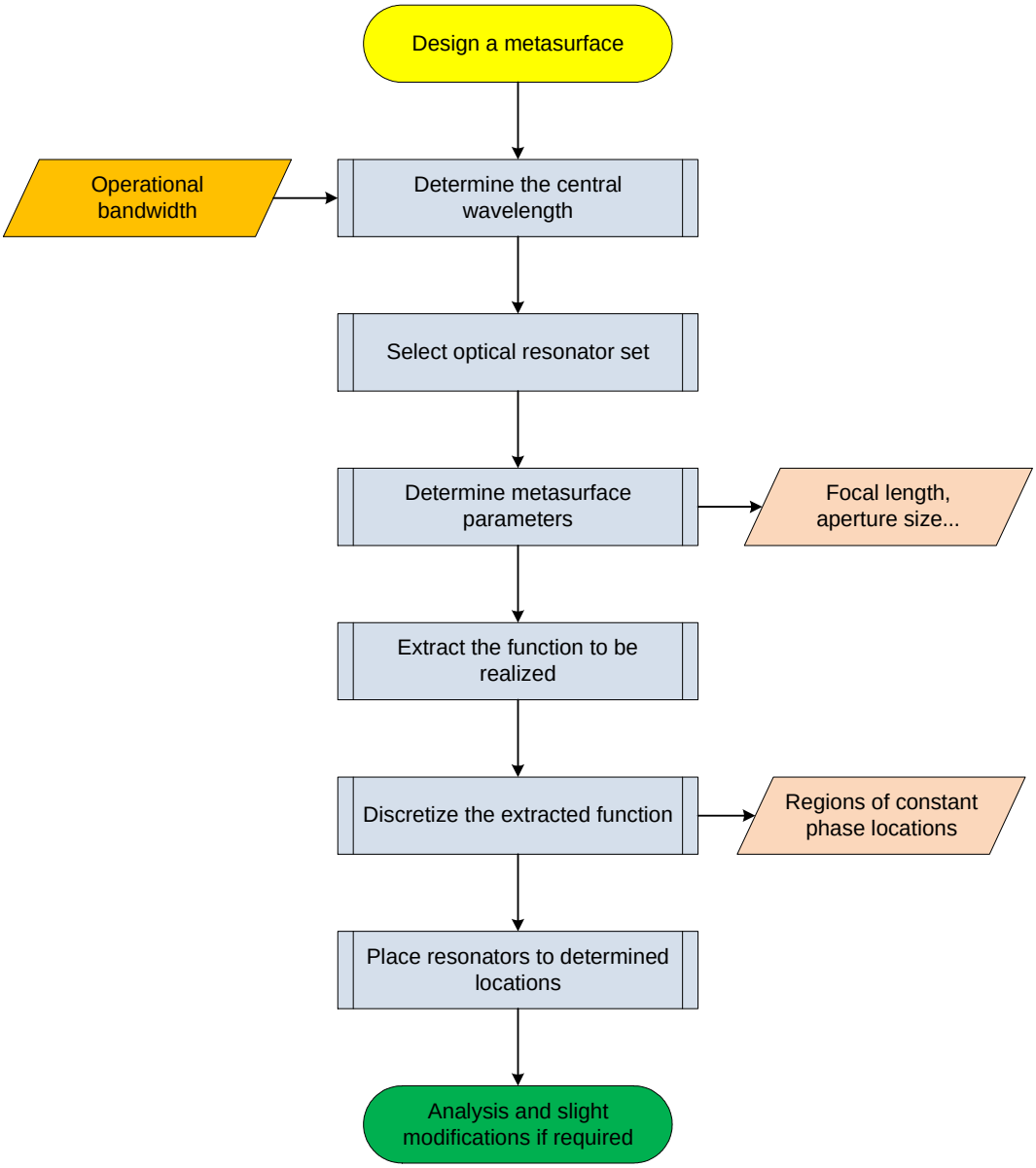


Figure 3.1: Depiction of the metasurface design methodology.

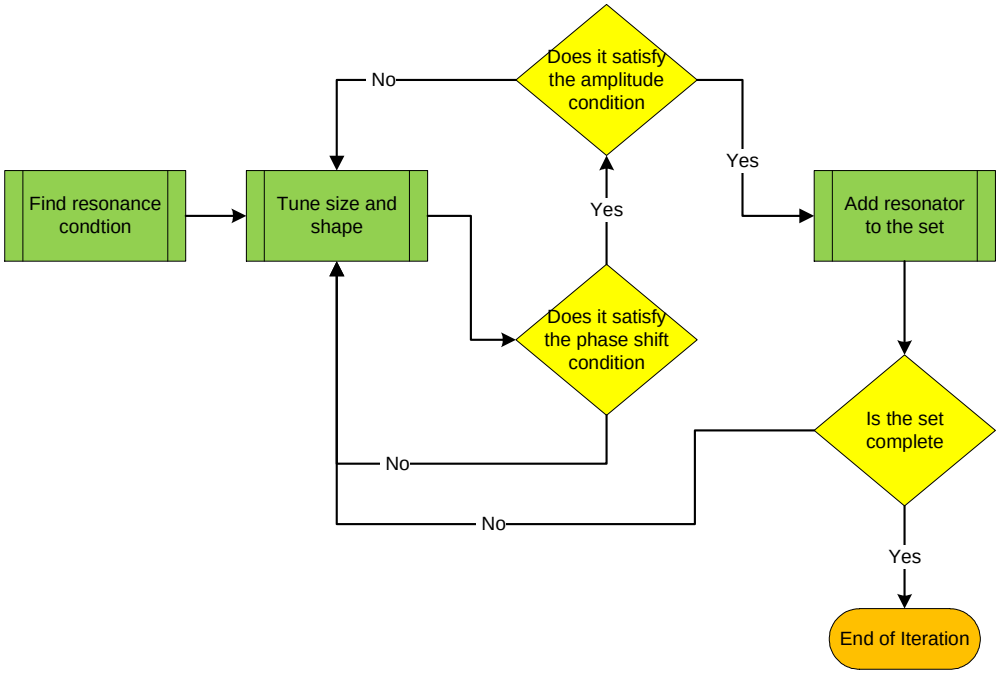


Figure 3.2: Procedure for selecting the resonator set.

Second and most time consuming step of designing a metasurface is the determination of the optical resonator set. A set of optical resonators shall be designed for covering the full $0-2\pi$ range while keeping the amplitude response as uniform as possible. In Chapter 2, a large parameter space is probed using method of moments and it is shown that V and L shaped metallic nanoantennas can satisfy the phase coverage property. A V-shaped nanoantenna model is given in Figure 2.30. The unit cell of this model is a square of edge length $L$ and special care must be given to this parameter since it should be long enough for avoiding mutual coupling of antennas when antennas placed nearby to built metasurfaces. The arm length and opening angle of a V-shaped nanoantenna is changed for tuning the phase shift response and by playing with these parameters, a set of V-shaped nanoantennas can be selected to fulfill phase coverage property with a moderate amplitude uniformity. An exemplary set is provided in Table 2.2. Generalized selection procedure for optical resonators is given in Figure 3.2. After selecting the building blocks, metasurface parameters such as size and functionality shall be determined. For a lens or a lenslet array, these parameters can be aperture size and focal length. Then using these parameters, phase shift response function of the metasurface can be extracted. Phase response that should be imparted on an incident light beam by a cylindrical lens is given by Equation (3.1).

$$\theta(r) = \frac{2\pi}{\lambda}(\sqrt{r^2 + f^2} - f) \tag{3.1}$$

where $r$ is the distance to the lens center and $f$ is the focal length while $\lambda$ is the free space wavelength. This phase response is plotted for two lenslets of different f-numbers and same $(50\mu m)$ aperture size in (a) and (b) of Figure 3.3. However, these continuous phase responses cannot be realized by discontinuous arrangement of optical resonators. Therefore, these phase responses must be discretized into constant phase regions. If a set of $n$ antennas is selected, then the full phase shift response $2\pi$ is divided into $n$ constant phase regions. For a set of 8 antenna, the discretized phase responses imparted by exemplary lenslet metasurfaces are given in (c) and (d) of Figure 3.3.

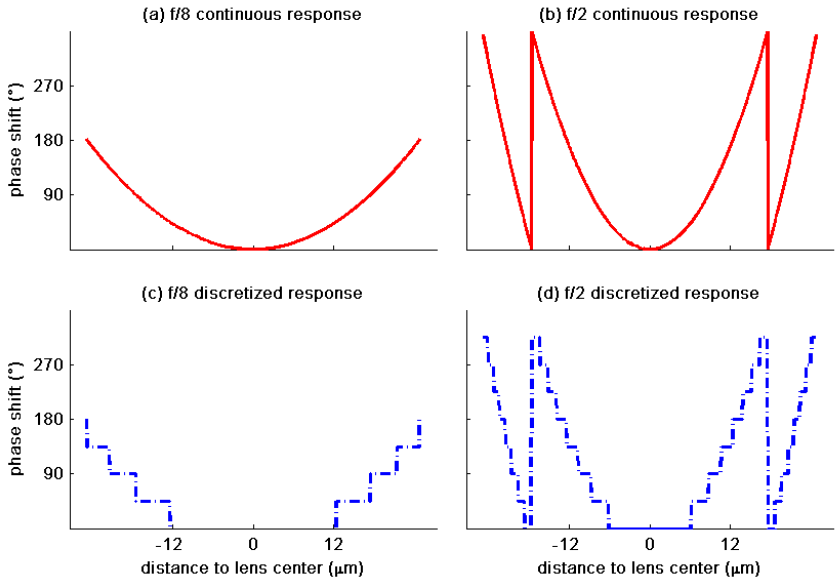


Figure 3.3: Exemplary continuous and discretized phase shift responses of the metasurfaces.

Final step of the metasurface design procedure is placing the resonators with appropriate phase shift response to desired location for realizing the discretized phase response of the metasurface. For a set of 8 antennas, arrangement of V-shaped nanoantennas is shown in Figure 3.4. In this figure, constant phase shift regions are represented with shadings of different densities.

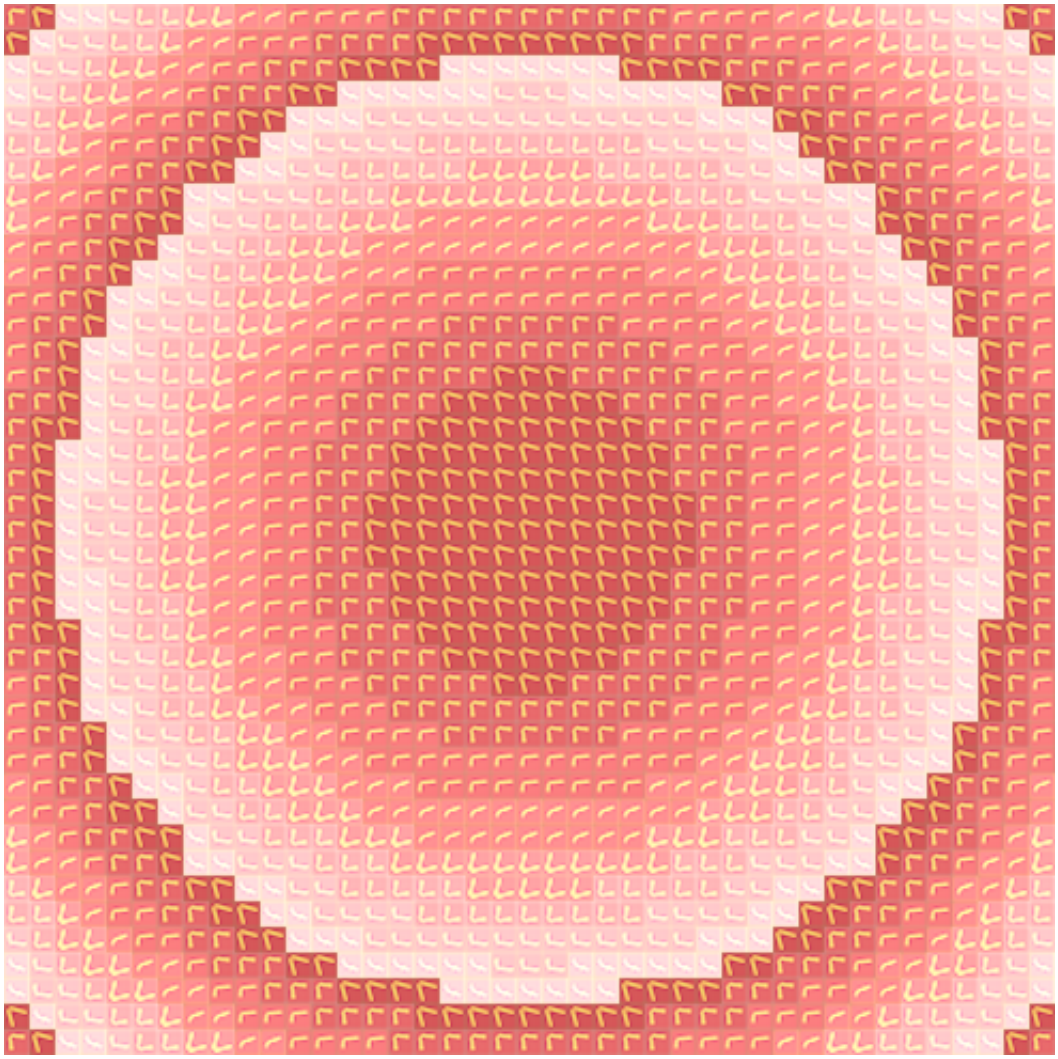

Figure 3.4: Realization of the phase shift response by placing nanoantennas.

## 3.2 Example Designs

### 3.2.1 Metasurface Lens Design

In this subsection, several lenslets and lenslet arrays are designed using the metasurface design methodology described in Section 3.1. As the central design wavelength, 1550 nm is selected. A set of 8 symmetric V-shaped nanoantennas is selected as the optical resonator set that fulfills the $0 - 2\pi$ phase shift coverage issue. The properties of this antenna set is given in Table 2.1 and Table 2.2. The design parameters of the lenslet arrays are given in Table 3.1.

The phase shift responses of the lenslets in the lenslet arrays are given in Figure 3.5. In this figure, only the phase response of one lenslet is shown for each lenslet array. Continuous curves correspond to ideal phase responses while dotted-dashed curves correspond to discretized versions of ideal phase responses. For realization of the discretized phase shift response, the symmetric V-shaped nanoantennas in the antenna set are placed one by one on phase shift response defined locations of a silicon substrate. Since, the discretized phase shift responses have constant phase shift regions, these regions are populated by same antennas having same phase shift response. The distribution of antennas in these regions are provided in Table 3.2.

Table 3.1: Metasurface lenslet array design parameters

| Lenslet Type | No of Lenslets | Focal Len. ($\mu m$) | Aperture Dia. ($\mu m$) |
|---|---|---|---|
| 1 | 2 | 200 | 49.95 |
| 2 | 4 | 100 | 24.95 |
| 3 | 6 | 100 | 24.95 |
| 4 | 6 | 100 | 35.35 |

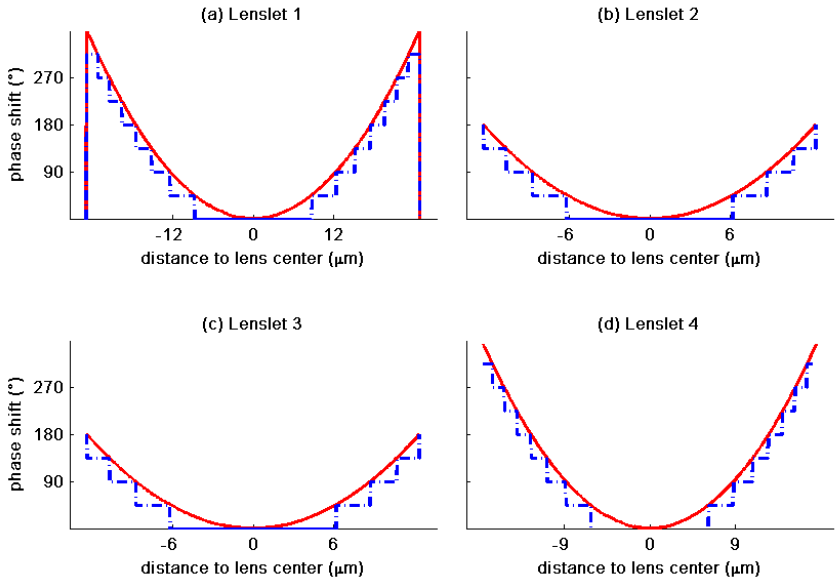


Figure 3.5: Continuous and discretized phase shift responses of the lenslets.

For modeling the lenslet arrays in Lumerical FDTD, symmetric V-shaped nanoantenna's described in Section 2.2.3 are placed inside a 300 nm by 300 nm unit cell. Then, the center of this unit cell is placed to the origin of the simulation region and shifted to the discretized phase response specified location of a silicon substrate. Each constant phase region specified in Table 3.2 are scanned by these unit cells. By this way, a lenslet is modeled and by repeating this lenslet along the desired directions a lenslet array is modeled. Since the FDTD simulations are very time consuming, we modeled these lenslet arrays as cylindrical lenslet arrays instead of spherical ones so that periodic boundary conditions can

Table 3.2: Antenna distributions in constant phase regions of lenslets

| Lenslet 1 | | Lenslet 2 | | Lenslet 3 | | Lenslet 4 | |
|---|---|---|---|---|---|---|---|
| Reg No | No of Ant | Reg No | No of Ant | Reg No | No of Ant | Reg No | No of Ant |
| 0 | 59 | 0 | 41 | 0 | 41 | 0 | 41 |
| 1,-1 | 12 | 1,-1 | 9 | 1,-1 | 9 | 1,-1 | 9 |
| 2,-2 | 9 | 2,-2 | 6 | 2,-2 | 6 | 2,-2 | 6 |
| 3,-3 | 8 | 3,-3 | 6 | 3,-3 | 6 | 3,-3 | 6 |
| 4,-4 | 7 | 4,-4 | - | 4,-4 | - | 4,-4 | 5 |
| 5,-5 | 6 | 5,-5 | - | 5,-5 | - | 5,-5 | 4 |
| 6,-6 | 6 | 6,-6 | - | 6,-6 | - | 6,-6 | 5 |
| 7,-7 | 6 | 7,-7 | - | 7,-7 | - | 7,-7 | 3 |

be used to decrease computation time. After modeling the cylindrical lenslet array, a monochromatic (1550 nm) plane wave source is injected from the silicon substrate. The polarization of the incident field is along the $+\hat{x}$ direction of the simulation region where the antennas are located on a silicon substrate that lied on the $x-y$ plane. The antennas are oriented in such a way that their symmetry axis and the polarization direction of the incident field has an angle of 45°. This orientation angle makes sure that both of the orthogonal resonance modes in the antennas are excited. Then the scattered field is recorded on a near field monitor that is located above the lenslet array structure. Finally, this recorded field data is transformed into far-field for cross-polarized (with respect to incident field) field. This far-field data is sampled along the normal direction ($+\hat{z}$) of the lenslet array surface and focusing behavior is observed. This focusing behavior of lenslets in the arrays can be seen in Figure 3.6 as the beam-width of the scattered field narrows at the metasurface dictated focal plane.

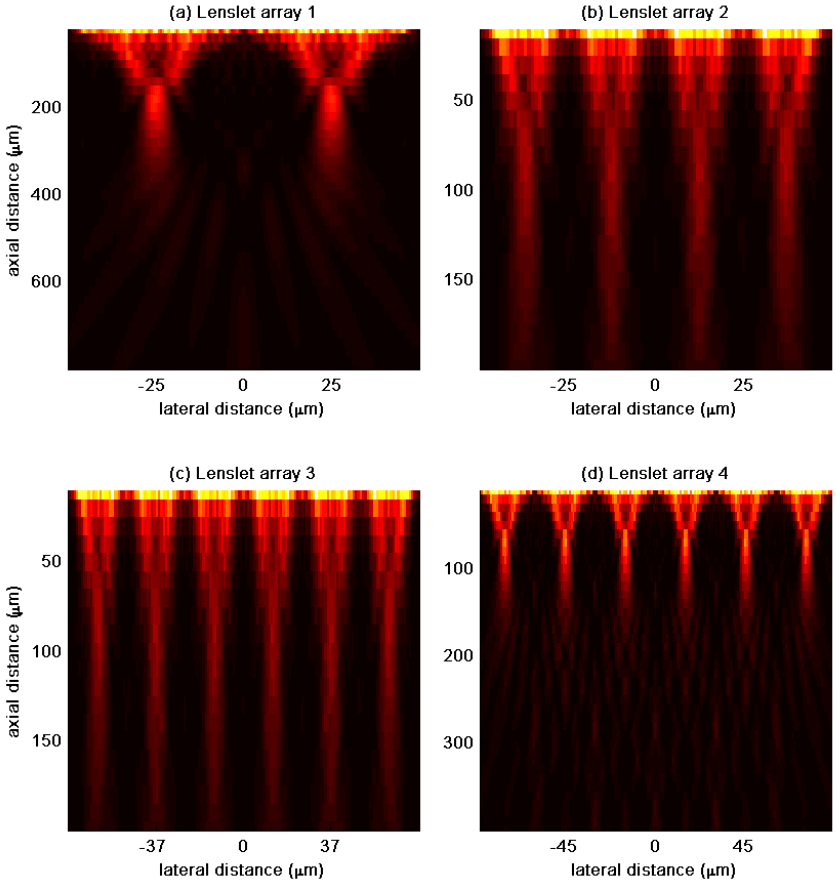


Figure 3.6: Cross-polarized far-field distributions of the lenslet arrays.

### 3.2.2 Metasurface Parabolic Mirror Design

In this subsection, parabolic mirrors are designed using the metasurface design methodology described in Section 3.1. As the central design wavelength, 850 nm is selected. In the previous subsection, a set of 8 symmetric V-shaped nanoantennas are used to build transmitting metasurfaces since the lenslets are transmitting optical components. However, mirrors are reflective optical components and reflective metasurfaces should be designed to function as mirrors.

The optical resonator model used for building metasurface mirrors is depicted in Figure 3.7. In this model, a gold plate is used for reflecting the incoming field and a gold rectangular prism is placed on top of a magnesium fluoride spacer which is also placed above the gold plate. By tuning the size of this gold rectangular prism, phase of the reflected beam can be controlled with an almost constant amplitude response. The width, length and thickness of the gold plate is fixed and set to $L_1 = 120nm$, $L_2 = 300nm$ and $d_3 = 130nm$, respectively. Similarly, the width, length and thickness of the magnesium fluoride spacer is also fixed and set to $L_1 = 120nm$, $L_2 = 300nm$ and $d_2 = 50nm$, respectively. The width and thickness of the gold plate is also fixed at $w = 90nm$ and $d_3 = 30nm$, respectively but its length $L$ is varied to control the phase shift response at its location. An optical resonator set of 8 reflective metasurface unit cells is obtained after performing FDTD simulations by modeling these unit cells having only $L$ varied. Simulation region and meshing properties are similar to the FDTD simulations of the V-shaped nanoantennas, however, Lumerical FDTD lacked the refractive index data for magnesium flouride. This data is calculated using the temperature dependent Sellmeier coefficients [97]. Since this structure is a reflective structure, a near field monitor is placed below the structure and source to record the reflected field. Then this recorded reflected near field data is transformed with far field transformation functions to obtain the far field phase shift and amplitude responses. The phase shift responses and lengths of this optical resonator set is given in Table 3.3.

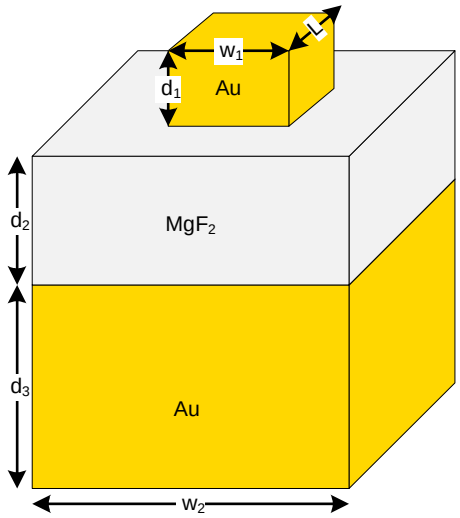


Figure 3.7: Reflective metasurface unit cell model.

Two different sized ($27\mu m$ and $19\mu m$) parabolic metasurface mirrors with same focal length of $50\mu m$ are designed. The continuous and discretized phase response of these mirrors are given in Figure 3.8. Continuous curves correspond to ideal phase responses while dotted-dashed curves correspond to discretized versions of ideal phase responses. For realization of the discretized phase shift response, the reflective metasurface unit cells in the optical resonator set are placed one by one on phase shift response defined locations. Since, the discretized phase shift responses have constant phase shift regions, these regions are populated by same unit cells having same phase shift response. The distribution of these unit cells in these regions are given in Table 3.4.

Table 3.3: Phase shift responses of modeled reflective metasurface unit cells

| Antenna Type | Length (nm) | Phase Shift (°) |
|---|---|---|
| 1 | 40 | 134 |
| 2 | 104 | 177 |
| 3 | 122 | 218 |
| 4 | 134 | 258 |
| 5 | 146 | 302 |
| 6 | 162 | 349 |
| 7 | 206 | 35 |
| 8 | 260 | 51 |

Table 3.4: Reflective metasurface unit cell distributions in constant phase regions of mirrors

| Mirror 1 | | Mirror 2 | |
|---|---|---|---|
| Reg No | No of Ant | Reg No | No of Ant |
| 0 | 31 | 0 | 31 |
| 1,-1 | 6 | 1,-1 | 6 |
| 2,-2 | 5 | 2,-2 | 5 |
| 3,-3 | 4 | 3,-3 | 4 |
| 4,-4 | 4 | 4,-4 | - |
| 5,-5 | 3 | 5,-5 | - |
| 6,-6 | 3 | 6,-6 | - |

For modeling the parabolic metasurface mirrors in Lumerical FDTD, reflective metasurface unit cells are placed at the center of the simulation region. Then, the center of a placed unit cell is shifted to the discretized phase response specified location. Each constant phase region specified in Table 3.4 are scanned by these unit cells. By this way, a parabolic is modeled. Since the FDTD simulations are very time consuming, we modeled the parabolic mirrors as cylindrical mirrors so that the periodic boundary conditions can be used to decrease computation time. After modeling the structure, a monochromatic (850 nm) plane wave source is placed for exciting the structure. Then the reflected field is recorded on a near field monitor that is located below the plane wave source. Finally, this recorded field data is transformed into far-field. This far-field data is sampled along the normal direction ($+\hat{z}$) of the metasurface mirror and focusing behavior is observed. This focusing behavior of metasurface mirrors can be seen in Figure 3.9 as the beam-width of the scattered field narrows at the metasurface dictated focal plane.

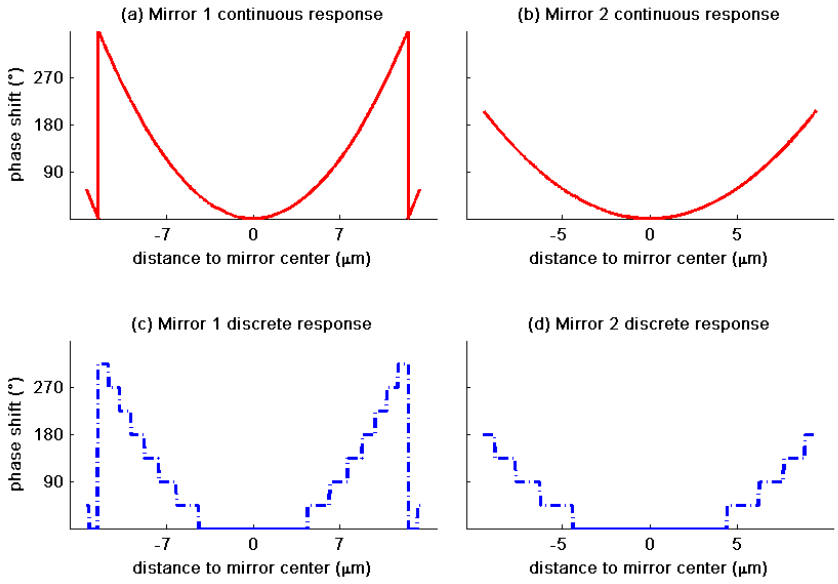


Figure 3.8: Continuous and discretized phase shift responses of metasurface mirrors.

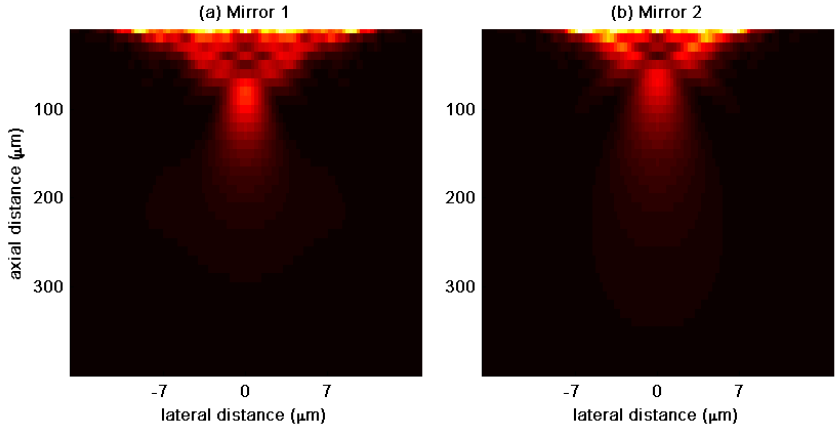


Figure 3.9: Far-field distributions of reflected beam from the metasurface mirrors.

### 3.2.3 Metasurface Magnetic Mirror Design

In this subsection, a metallic metasurface-based mirror that relies on silver nanogrooves and operates in the visible region of the spectrum is presented and its resulting strong field localization capability is quantitatively analyzed, which can be useful for reducing lasing threshold in CdSe nanostructure lasing.

#### 3.2.3.1 Field Localization Problem

Semiconductor nanostructure lasing has the promising functionality of high spectral coverage due to quantum confinement effect [98]. This type of lasing generally requires a metallic contact plate which reflects the incoming beam with an 180° phase shift. Due to this phase shift, the reflected beam reaches its peak value after propagating a quarter wavelength distance. However, since the semiconductor nanostructure has a subwavelength thickness, the field strength inside the nanostructure can be very low (closer to minimum of the field strength). Therefore, this metallic contact configuration causes a field localization problem, thereby increasing the lasing threshold. For reducing lasing threshold, the distribution of the reflected field should be maximized inside the nanostructure (which is subwavelength close to the metallic contact) using a contact that acts as a perfect magnetic conductor. However, this can not be achieved using metallic contacts since this requirement fundamentally contradicts with the boundary conditions imposed by metals that ideally act as perfect electric conductors.

#### 3.2.3.2 Approach, Methodology and Modeling

**3.2.3.2.1 Metallic Metasurface Approach and Methodology** Recently, reflective type metasurfaces such as metasurface mirrors (metamirrors) have started to attract increasing attention following the initial interest in transmission mode metasurface optical components [6, 50, 75, 79]. Metallic metamirros were designed for achromatic conversion of polarization state of light [50]. Dielectric metamirrors were designed for surpassing the reflectance of metal mirrors and over 99% reflectance was reported at the telecommunication wavelength of $1530nm$ [75]. At the same wavelength, frequency selective dielectric metamirrors with reflection phase control were also designed [79]. However, these studies were limited to the infrared region of the spectrum. Esfandyarpour et al. studied the surface impedance engineering of metamaterial mirrors in the visible spectrum (at $600nm$) [6]. In that study, magnetic metamirrors were designed and fabricated for increasing the absorption efficiency and photocurrent generation in solar cells and close to 20% enhancement was reported. However, functionality and performance of magnetic metamirrors were previously not studied for the purpose of reducing lasing threshold to the best of our knowledge. Especially,

reflectance phase engineering in the presence of semiconductor (CdSe) quantum dots or nanoplatelets using metamirrors was not explored and analyzed in detail.

For addressing the problem of field location in contact surfaces, metallic metasurface approach can be used since metasurfaces allow for control of the phase profile along the surface. Moreover, since the contact based on metasurface will be used a reflectance-mode optical component, transmission efficiency issues of transmission-mode metallic metasurfaces will not be encountered. Using this approach, we developed a methodology based on designing magnetic metasurface mirrors (metamirrors) for engineering the intensity distribution of the reflected light inside the active semiconductor nanostructure layer by controlling the reflectance phase of the metamirror. An examplary schematic describing the metamirror that can be used for reducing lasing threshold in CdSe quantum dots is given in Figure 3.10. While designing these magnetic metamirrors, the effect of semiconductor nanostructures on reflectance phase should also be considered for optimizing the intensity distribution inside the active semiconductor layer.

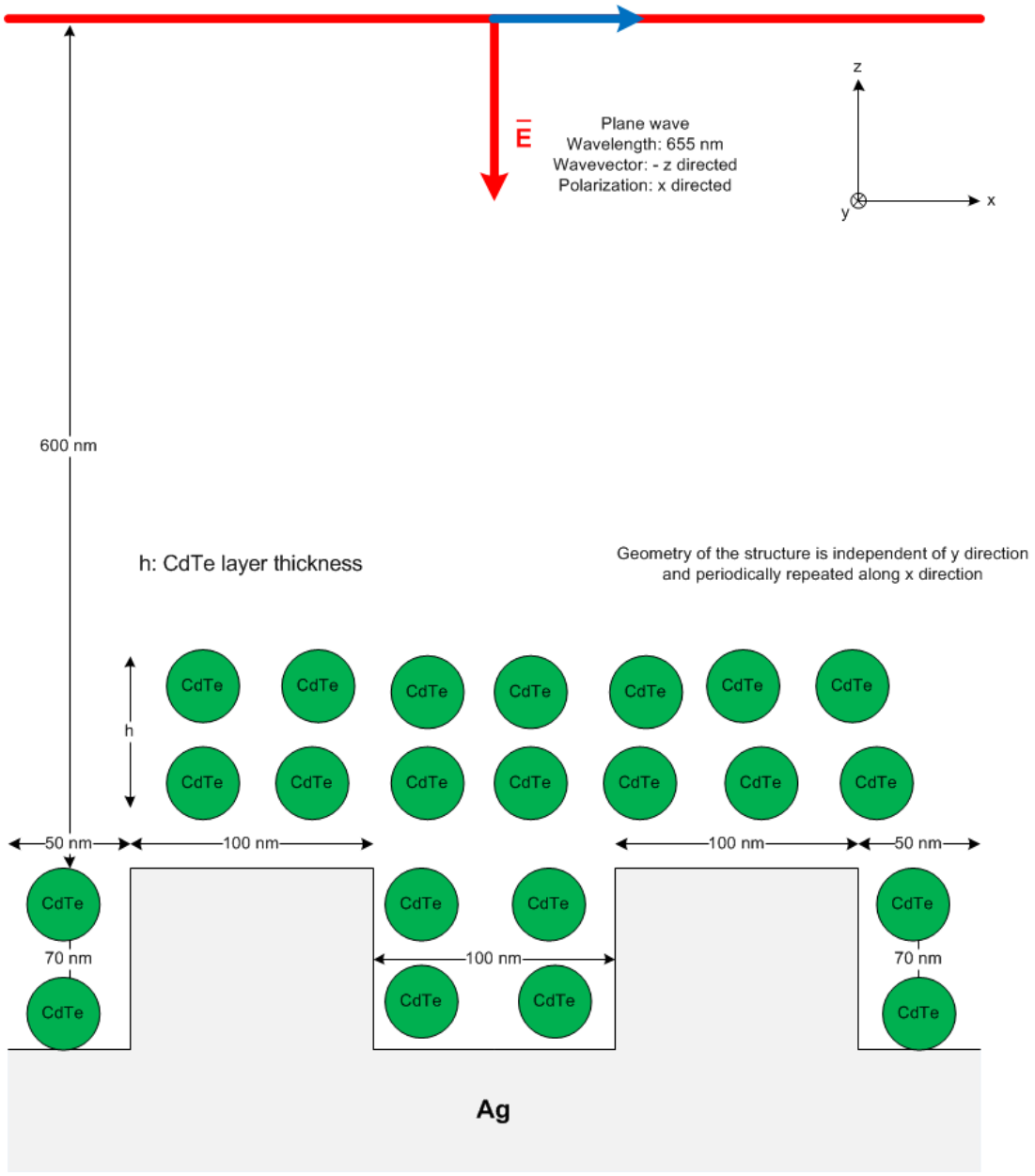


Figure 3.10: Schematic of the metamirror with CdSe quantum dots on top.

To optimize the electric field intensity inside a subwavelength active semiconductor nanostructure layer on top of a metallic metasurface, reflectance from the surface must be engineered. The reflection coefficient for a surface defined by its permittivity and permeability takes the following form

$$r_s = \frac{z_s - z_a l}{z_s + z_a l} \tag{3.2}$$

for an s polarized light normally incident upon the surface [40]. $z_{al} = \sqrt{\frac{\mu_{al}}{\varepsilon_{al}}}$ and $z_s = \sqrt{\frac{\mu_s}{\varepsilon_s}}$ are the impedances of the active layer and the surface to be realized as metasurface, respectively. For a high conductivity metallic surface, $z_s$ is low with respect to $z_{al}$ and this results in a $\pi$ radian reflectance phase thereby diminishing the electric field inside the active layer. For enhancing the electric field inside the active layer, structures consist of nanogrooves can be used by exciting the surface plasmon polaritons (SPP) on the walls of the nanogrooves for creating an interference Fabry-Perot cavity [99]. Nanogroove structures are defined by their widths (periods) and depths and by tuning these parameters the surface impedance can be controlled [37]. Therefore, metamirrors can be designed by patterning nanoscale grooves inside silver (Ag) plates for engineering the reflectance phase by controlling the surface impedance with fine tuning the width and depth of the nanogrooves.

**3.2.3.2.2 Modeling and Simulations** For realizing metasurface mirrors that can act as perfect magnetic conductors while providing strong field localization, we designed metasurfaces by patterning nanoscale grooves on top of a flat silver substrate. For modeling these metasurface mirrors and simulation the distribution of the field reflected from these metasurfaces, we used Lumerical Finite Difference Time Domain (FDTD) solutions. Firstly, the silver contact was modeled as a thin (along z direction) silver plate that extends along the x and y directions of the simulation region which has a size of $800nmx800nmx1200nm$. Then, this silver plate was placed at the bottom of this simulation region. The nanogrooves were modeles as silver rectangular prisms that extend along the y direction of the simulation region. The width of the rectangular prisms varied between $50nm$ and $200nm$ with steps of $50nm$ while the depth was varied between $0nm$ (corresponding to the standard silver contact that ideally act as perfect electric conductor.) and $200nm$ with steps of 10 nm.

For meshing the metasurface mirror, graded meshing was used such that the nanogrooves were meshed with the highest precision while the degree of precision was gradually decreased as a function of the distance to the nanogrooves (along z direction). As boundary conditions, perfectly matched layer (PML) bounday condition was applied along the direction normal to the metamirror surface and periodic boundary condition was used along the directions parallel to the metamirror surface. As the light source, a monochromatic plane wave (PW) light source that has $520nm$ wavelength was used and its polarization was changed orthogonally between two subsequent simulation runs. For collecting the reflected light from the meta-mirror, a field monitor was placed at a distance of $800nm$ from the metamirror. Also, another planar field monitor was placed orthogonal to the metamirror for recording the field distribution around the metamirror.

For modeling the behavior of the metamirror correctly, a CdSe layer that also covers the regions inside the nanogrooves was also placed. The refractive index data was obtained after conducting measurements with the synthesized CdSe nanostructures. After the modeling of the nanogrooves, semiconductor (CdSe) nanostructures were modeled as rectangular prisms filling the gaps of the nanogrooves.

#### 3.2.3.3 Results and Discussions

For analyzing the behavior of metasurface mirrors designed, full wave simulations were performed using Lumerical FDTD. Figure 3.11 illustrates the field distribution on top of the metasurface magnetic mirror when excited with TE polarized light. Although the metasurface mirror was designed to act as a magnetic metasurface mirror, the field distribution was very similar to the field distribution of an ordinary metallic mirror. The reason of this behavior is anti-symmetric structure of the mirror which can not respond to the TE polarized light as a metasurface magnetic mirror. However, when the same metasurface was excited with TM polarized light, the expected behavior was confirmed. This field distribution is illustrated in Figure 3.12. As seen in Figure 3.12, electric field strength is strongly localized around the nanogrooves. This strong localization can be very useful in reducing lasing threshold in CdSe nanostructure lasing.

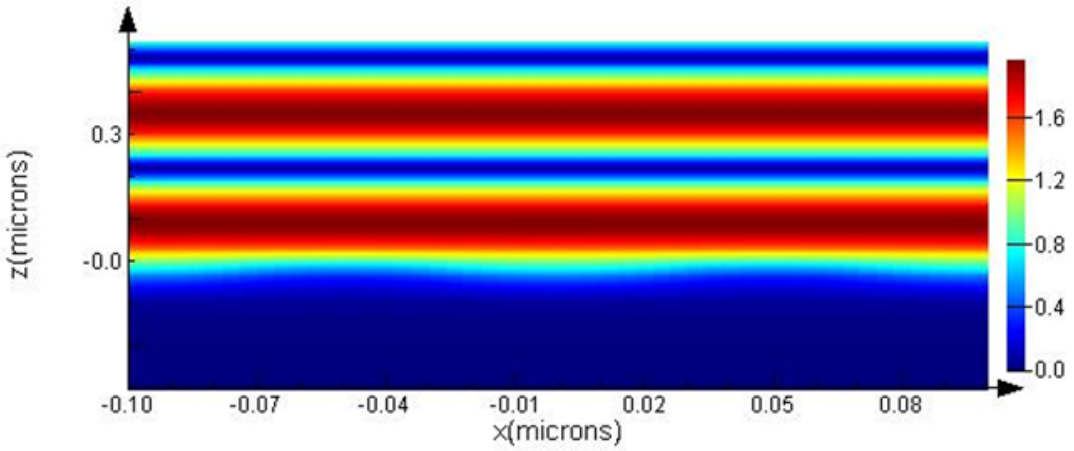


Figure 3.11: TE polarized field distribution on top of the metasurface magnetic mirror.

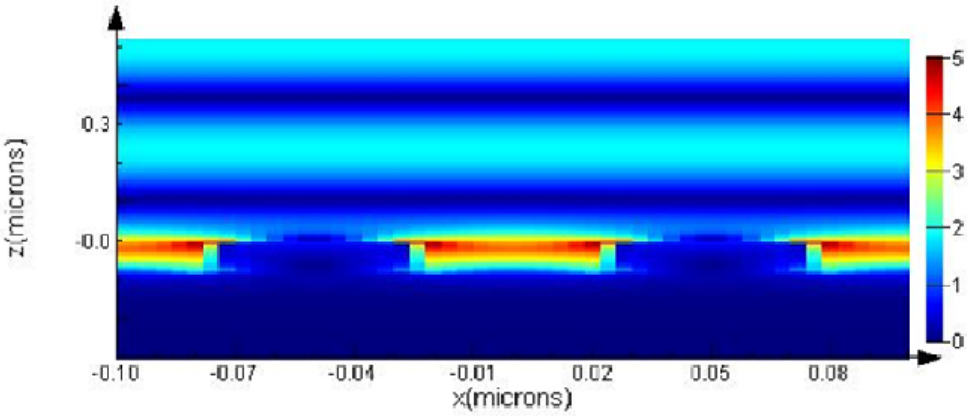


Figure 3.12: TM polarized field distribution on top of the metasurface magnetic mirror.

For optimizing the field localization around nanogrooves, the groove depth is varied between 10 nm and 200 nm with steps of 5 nm. The designed metasurface mirrors were excited with TM polarized light and phase shifts imposed by them were recorded using near-field monitors. These phase shift responses were plotted in Figure 3.13. As seen in Figure 3.13, metasurface mirror with nanogroove depth of 70 nm imposed a phase shift response close to 0, thereby acting as a magnetic metasurface mirror. However, the response of the metasurface mirrors were disturbed when CdSe nanostructures were modeled and filled the void inside nanogrooves. Resulting phase shift responses were plotted Figure 3.14. This time metasurface mirror with nanogroove depth of 40 nm imposed a phase shift response close to 0, thereby acting as a magnetic metasurface mirror.

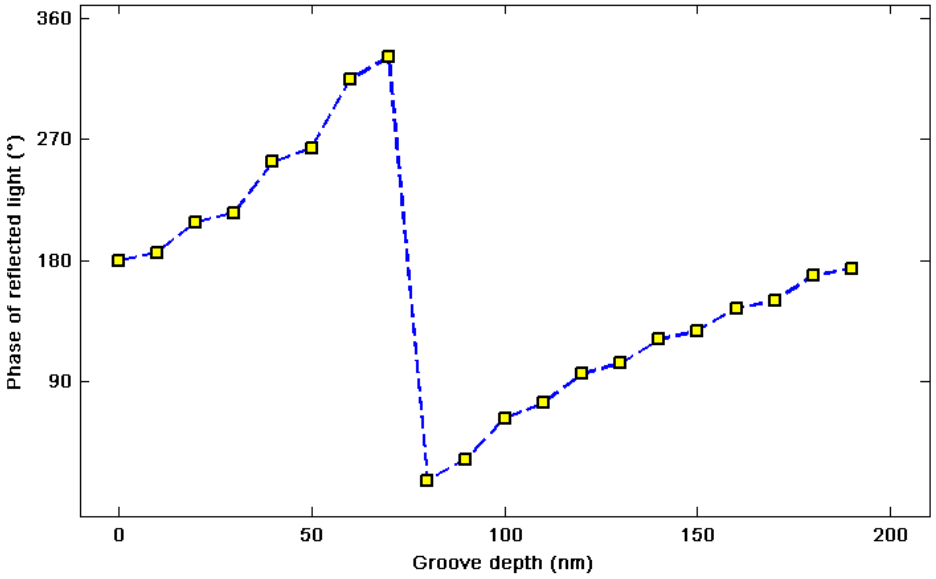


Figure 3.13: Phase shift imposed by metasurface mirrors with varying nanogroove (without CdSe) depths.

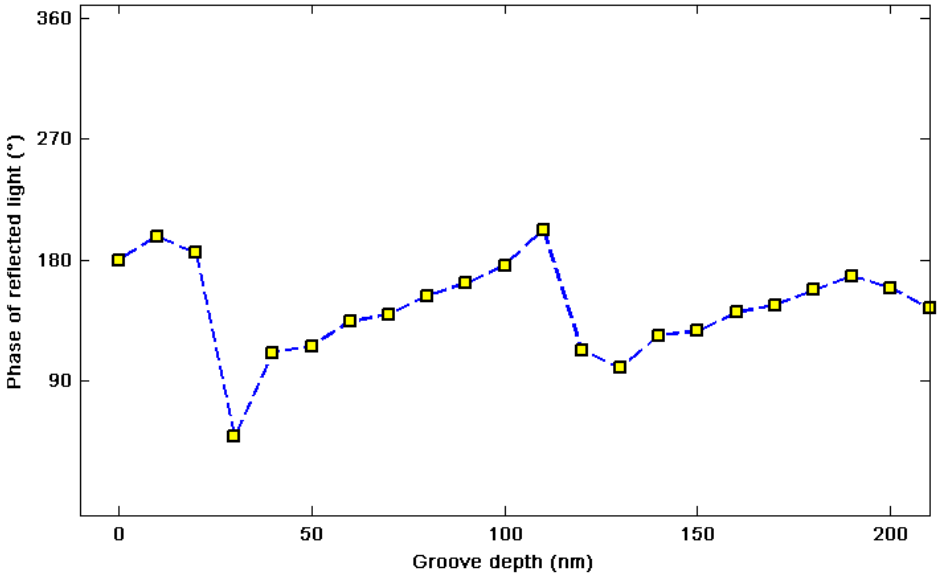


Figure 3.14: Phase shift imposed by metasurface mirrors with varying nanogroove (filled with CdSe) depths.

# Chapter 4

# MWIR Metallic Metasurface Microlens Array with Excellent Optical Crosstalk

Mid-wavelength infrared (MWIR) is a sub-band of the infrared part of the electromagnetic spectrum and it covers the $3 - to - 5\mu m$ wavelength range. Electro-optical applications such as infrared search and tracking systems, infrared imaging systems use this MWIR region to produce signals and images [3]. The core component inside an infrared imaging system is a Focal Plane Array (FPA) that consists of a two-dimensional array of detectors. In MWIR region, FPA's can have very low noise levels ($\leq 50mK$) when cooled to low temperatures ($\leq 90K$) and this property makes them important components for applications requiring high signal-to-noise ratio.

In this chapter, a metallic metasurface-based microlensed FPA that relies on asymmetric optical antennas and operates in MWIR region is presented and its resulting light concentrating capability is quantitatively analyzed, which is useful for suppressing optical cross-talk in MWIR-FPAs.

## 4.1 Optical Crosstalk Problem

Following the improvements in nanoscale growth and fabrication technologies, it has become possible to increase the spatial resolution of IR-FPAs without changing the FPA size. Thanks to these improvements, compact products with high spatial resolution can be developed, packaged and commercialized. However, as the spatial resolution increases, pixel pitch size must decrease to keep the FPA size unchanged. Unfortunately, optical crosstalk between adjacent pixels start to increase tremendously as the pixel pitch size is reduced. This issue limits the device's spatial noise performance which is very critical for obtaining high quality images. Therefore, a fundamental trade-off arises between high spatial resolution and low spatial noise.

In order to compensate the drawbacks of decreasing pixel pitch size, various strategies such as integration of microlens arrays with MWIR-FPAs and mesa isolation can be used. In the mesa isolation method, the pixels are physically separated by etching so that each pixel is spatially isolated from its neighbor pixels. However, one major drawback of this method is that the etching process can unrecoverably damage several pixels making them either dead or bad pixels. On the other hand, in the integration of microlens arrays methodology, pixels do not need to be physically isolated from each other thereby avoiding an etching process. This latter methodology rather relies on controlling and managing the incident light energy flow towards each pixel instead of changing the structure and boundaries of pixels.

Microlens array integration methodology has been applied in a recent study in which a refractive microlens array was integrated with mid-wave HgCdTe IR-FPAs [2]. In that study, the analysis of this method has been conducted numerically and the effects of microlens radius and relative aperture on optical crosstalk suppression have been reported. The refractive microlens array squeezed the size of the Airy disk at the target pixel hence it was expected that the optical crosstalk should be suppressed as less light should now be incident on adjacent pixels. However, the emergence of strong first-order diffraction spots approximately at the centers of the adjacent pixels add an additional optical cross-talk between adjacent pixels and the target pixel. Therefore, the positive effect of the refractive microlens array is canceled by the negative effect of diffraction spots. In another

study related to microlens array integration methodology, a diffractive microlens array was integrated with InSb MWIR-FPAs and the performance of diffractive microlens systems with respect to the refractive microlens systems were investigated [100]. Although an improved system performance was reported in that study, pixels of the InSb IR-FPA were also mesa-isolated. Therefore, the combined effect of both methodologies suppressed the spatial cross-talk in this system and this system still inherits the disadvantages of mesa-isolation technique.

## 4.2 Approach, Methodology and Modeling

In Section 3.2, metasurface lenslets and parabolic mirrors were designed using the metasurface design methodology described in Section 3.1. Various other optical components have also been designed using metasurfaces and novel phenomena such as anomalous reflection and refraction have been observed in recent studies [5, 10–30]. The reason that so many different types of optical components can be designed with metasurfaces is the ability to control the amplitude, phase and polarization state of light on a subwavelength scale with very high precision. As a result of this precise controllability, it is possible to modulate wavefront of light in a desired manner and light beam structure can be designed with new degrees of freedom [5, 10–12].

Integration of microlens array methodology relies on controlling and managing the incident light energy flow towards each pixel as stated in Section 4.1. Similar to controlling and managing the incident light energy, light energy focusing has also been investigated in the context of metasurfaces [27–31]. However, to date integration of metasurface microlens arrays with FPA's have not been studied and optical crosstalk problem has not been addressed in such metalens arrays.

### 4.2.1 Metallic Metasurface Approach and Methodology

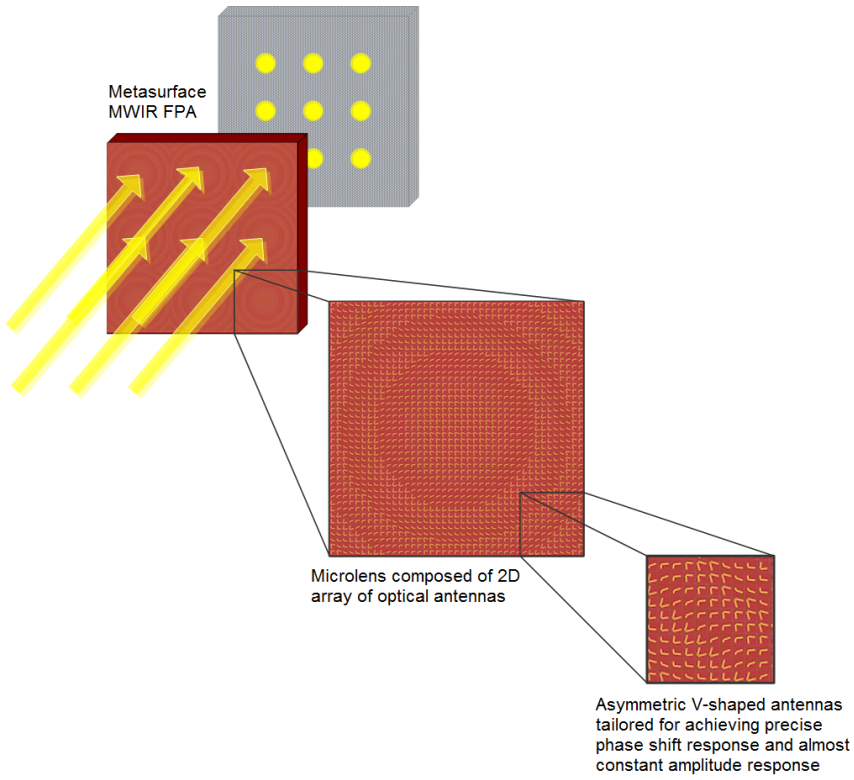


Figure 4.1: Schematic representing the geometry of the proposed metasurface-based microlensed focal plane array (FPA) design [1].

For addressing optical cross-talk problem by using metasurface approach, a metasurface-based microlensed focal plane array that relies on asymmetric optical antennas can be designed [see Figure 4.1 for conceptual architecture]. Then, quantitative analysis of this design's resulting light concentrating capability, which is useful for optical crosstalk suppression in mid-wave IR-FPAs, can be conducted. A two-dimensional array of asymmetrically tailored optical antennas having space-variant phase shift response and subwavelength separation forms the basis of the proposed planar metasurface. Instead of tuning the intrinsic material properties of these optical antennas, their resonances were tuned to realize space-variant phase shift response.

The first part of the metasurface approach methodology involves the design of the mentioned optical antennas followed by the analysis of their scattering characteristics with finite-difference time domain (FDTD) simulations. The second part of this methodology involves the design of metasurfaces for implementing microlens arrays using a specific antenna set based on the analysis carried out in the first part.

### 4.2.2 Modeling and Simulations

#### 4.2.2.1 Modeling of Optical Antennas

The building blocks of the metasurface-based microlenses are asymmetrically-tailored, V-shaped optical antennas. These antennas consist of two end-connected gold nanorods placed on a silicon substrate. The geometry of the selected optical antennas are shown in exemplary schematics of Figure 4.1. Connection angle of the antennas and the length of each nanorod comprising the antenna are tuned separately for covering the full $0 - to - 2\pi$ phase shift response, which is mandatory for designing microlenses. For maximizing the constructive interference of the scattered fields, the amplitude responses of the antennas were hold almost constant. A set of 8 antennas are used in fulfilling the phase shift coverage necessity; hence, an incremental phase shift response of $\frac{\pi}{4}$ exists between subsequent antennas of the microlens array in the set.

FDTD simulations were performed for every single antenna in order to design the specific geometry of the optical antennas. For performing these FDTD simulations Lumerical Solutions FDTD was used. In order to simulate a realistic geometry that can be easily fabricated, a previous metasurface study is used as a reference and similar (scale-wise) structures were designed [52]. Therefore, cross-section of the nanorods were designed as a square with a 100 nm width and a 100 nm thickness. A multicoefficient model was fit by the values found in Palik in order to input the optical constants that determine the optical properties of the antennas [101]. In order to choose the substrate on which the optical antennas are placed, several FDTD simulations are performed with silicon and germanium. We chose these materials as substrate candidates since high refractive index substrate such as silicon and germanium should be used for obtaining smaller building blocks that increase the continuity of the imparted phase profile. The optical antennas were placed on the central region of a silicon substrate after obtaining quite similar results from both simulations. Half of the total simulation area was filled with this silicon substrate which spans $0.75\mu mx0.75\mu mx2.5\mu m$. The simulation area was matched by perfectly matched layers at its boundaries and the other half of the simulation are is modeled as air. A fixed mesh size of $10nm$ along the lateral directions that spans the silicon-air interface is used. However, graded meshing was used along the normal direction to the interface and the antenna-silicon-air boundaries are precisely meshed. A total-field scattered field (TFSF) planewave source that has a wavevector direction normal to the antenna plane and polarization direction having 45° angle with the antenna symmetry axis was used to excite the antenna from the silicon substrate side and this source spans a volume of $0.75\mu mx0.75\mu mx3.5\mu m$. A near-field monitor was used to record the scattered near field and it is placed parallel to the interface at a distance of $1.9\mu m$ from the interface. Finally, far-field transform function called "farfieldexact" was used to obtain the amplitude and phase of the scattered field that is cross-polarized with respect to the incident field and has direction normal to the antenna plane.

Following an iterative simulation process, specific geometries of the 8 antennas in the antenna set were designed. For conduction this iterative simulation process, length of one nanorod was varied from $300nm$ to $600nm$ while length of the other nanorod was varied from $100nm$ to $600nm$. Also, as a third parameter, the connection angle of the nanorods was also varied from 50° to 150° but only specific angles that allow the antennas to be kept inside a $750nmx750nm$ square,

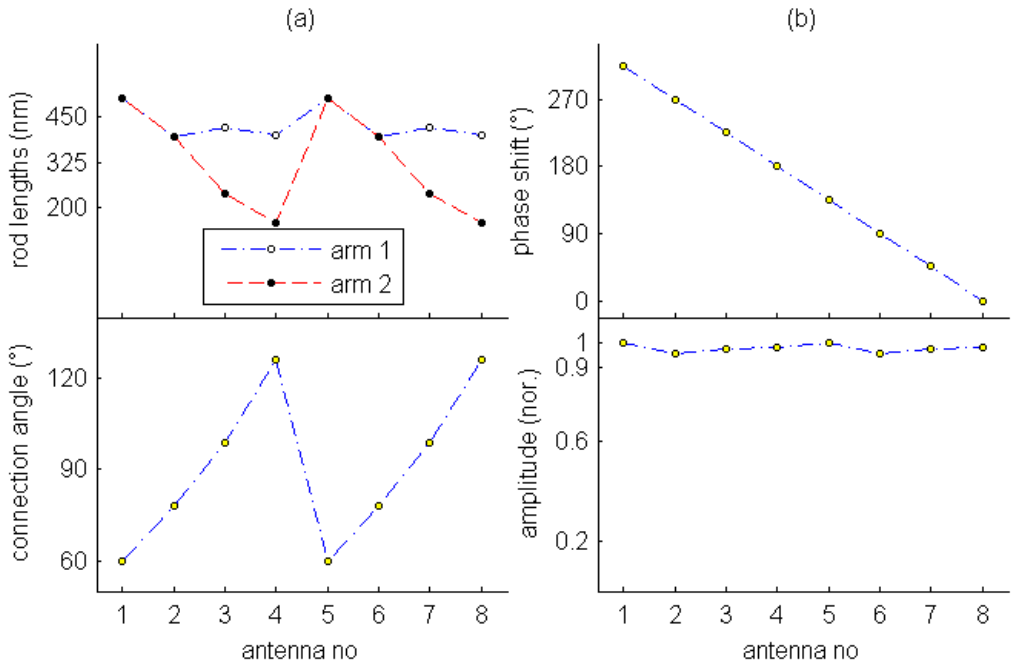


Figure 4.2: (a) Rod lengths and connection angles of the individual optical antennas. (b) Phase shift responses and normalized scattering amplitudes of the individual optical antennas [1].

were selected. The phase shift responses and scattering amplitudes of the selected antenna set, which cover full $0-to-2\pi$ phase shift response with an incremental phase shift response of $\frac{\pi}{4}$ and have almost constant scattering amplitude, are given in parts (a) and (b) of Figure 4.2.

We have analyzed the responses of individual building blocks of asymmetric V-shaped nanoantennas by varying the excitation wavelength. The resulting data is presented in (a) and (b) of Figure 4.3. In (a) of Figure 4.3, the standard deviation in normalized amplitude response of the antennas in the designed set is given. Even though the antenna set is optimized for the excitation length of $4.3\mu m$, their scattering amplitude did not vary much as the excitation wavelength is changed within the limits of MWIR band. This broadband response characteristics is inherent in metallic nano-antennas and previously also studied and reported by Ni et al. [9] for the demonstration of broadband light bending and Yu et al. [10] for the demonstration of broadband quarter wave-plates. In alignment of the previous literature and in the light of the computations for individual antenna

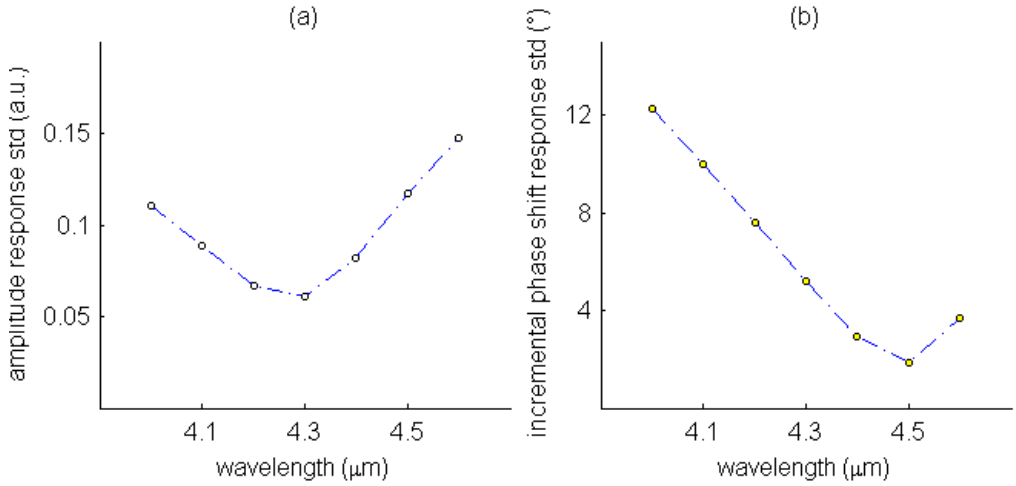


Figure 4.3: (a) Standard deviation in phase responses of the antenna set used in building the microlens arrays. (b) Standard deviation in amplitude responses of the antenna set used in building microlens arrays.

building blocks, it can be concluded that these antenna set can function across the entire MWIR bandwidth.

#### 4.2.2.2 Modeling of Microlens Arrays

Modeling of microlens array comprises of the matrix of microlenses repeated as a unit cell in two dimensions. Narrowing the spot size of the incident beam captured by the cross-section of a microlens is the main functionality of a microlens. In order to realize this functionality, a metasurface having a hyperboloidally varying phase shift response can be used. This response is mathematically formulated by the following equation for a cylindrically symmetric structure:

$$\theta(r) = \frac{2\pi}{\lambda}(\sqrt{r^2 + f^2} - f) \tag{4.1}$$

where r is the distance to the metasurface center and f is the focal length while $\lambda$ is the central design wavelength, here selected to be $4.3\mu m$ (as an MWIR $(3\mu m to 5\mu m)$ wavelength).

However, realizing this function practically with an array of optical antennas,

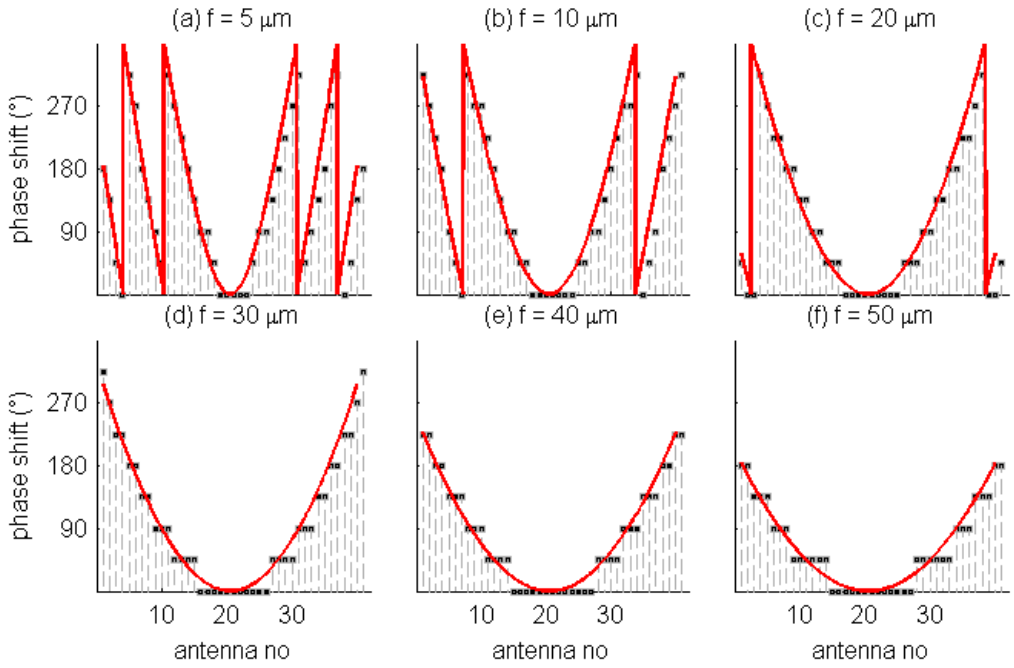


Figure 4.4: (a)-(f) Phase shift responses of the antennas in the designed microlenses with focal lengths of 5, 10, 20, 30, 40 and 50 $\mu m$, represented with black squared markers, respectively. Corresponding continuous phase shift responses realized by these microlenses are also shown with red curves [1].

each having an incremental phase shift, dictated the discretization of the continuous profile given by Equation (4.1). For implementing this discretization process, continuously changing portions of the continuous profile is mapped into constant phase regions. For example, $0 - to - 4\pi$ phase shift portion of the continuous profile was mapped to the 0 phase shift while the $\frac{\pi}{4} - to - \frac{\pi}{2}$ phase shift portion of the continuous profile was mapped to the $\frac{\pi}{4}$ phase shift so that only a single type of antennas (antenna no. 4) were placed in the 0 phase shift regions while another type of antennas (antenna no. 3) were placed in the $\frac{\pi}{4}$ phase shift region. These mentioned continuous phase profile and its discretization are given in Figure 4.4 for the central unit cells of the designed microlens arrays.

The designed microlens arrays had a unit cell having a fixed width of $30\mu m$. This size is a commercially available MWIR-FPA pixel pitch size and it contains 40 nano-antennas located on a square silicon substrate of 750 nm side length. This side length is determined with respect to the resonance condition of the

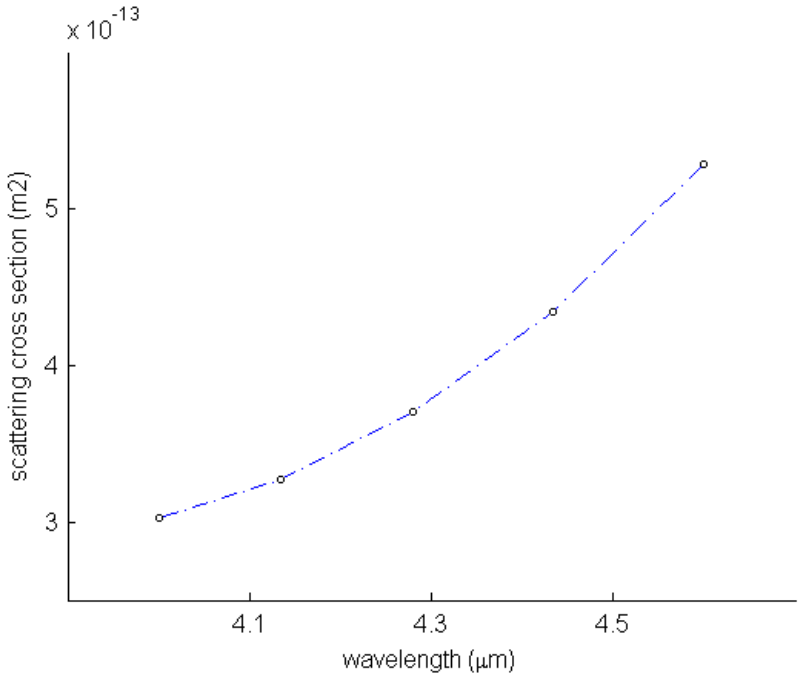


Figure 4.5: Scattering cross-section of the V-shaped nanoantenna having equal arm lengths of 395 nm and an opening angle of 78°.

antennas. The following equation describes this resonance condition:

$$l = \frac{\lambda_0}{2n_{eff}} \tag{4.2}$$

where $\lambda$ is the wavelength in free psace and $n_eff$ is the medium's effective refractive index while l is the length of the antenna. Using $4.3\mu m$ as the wavelength and 2.6 as the effective refractive index,l is calculated to be 826 nm. Although a single wavelength was used as a starting point for the design, the design was checked for the entire mid-wave IR by investigating the behavior of the antennas in different wavelengths of MWIR band Figure 4.3, confirming its operation across the entire band. For placing antennas having similar total lengths to this resonance length (hence covering a large phase shift) and picking a length that is an integral divisor of 30 $\mu m$, the side length was determined as 750 nm.

At this point, it is worth noting that, using this side length, neighboring V-antenna units remain uncoupled since no noticeable coupling effect between adjacent antennas that can alter their scattering response was observed. We have analyzed the scattering cross-section of our unit elements consisting of V-shaped

nanoantennas after simulating them in Lumerical FDTD (by using optical power analysis group for cross-section), which is shown in Figure 4.5. After running the analysis, we have found that the scattering cross-section for our largest and smallest sized V-shaped nanoantennas are $4.3 \times 10^{-13} m^2$ and $3.8 \times 10^{-13} m^2$. However, our unit cell has a size of $750nm \times 750nm$, making $5.62 \times 10^{-13} m^2$, which is 30% larger than the scattering cross-section of our largest V-antenna. We compared the scattering amplitude and phase responses of our unit cells by both varying the size of the unit cell and repeating the structure in one direction and we obtained similar results for both of the responses.

Lumerical Solutions FDTD was also used for performing the full-wave simulations of the designs microlens arrays. This time, periodic boundary conditions were used as constraints instead of PML along the directions tangential to the antenna plane. Also, the TFSF source was replaced with a planewave source. Again, we modeled cylindrical microlens arrays instead of spherical microlens arrays by utilizing the symmetry of the structure. This choice is necessary if the numerical solution is desired to be tractable in a reasonable amount of time. A monitor was placed on top of the microlens array structure at a distance of $1.9\mu m$ from the interface so that near-field distributions can be recorded. The far-field transformation function used in simulations of antennas was also used to obtain the intensity distributions (as a function of distance to the microlens array) of the cross-polarized field with respect to the source polarization. In Figure 4.6, the far-field transformed intensity distributions are given for 6 different microlens array structures corresponding to the focal length varied realizations of the hyperboloidally varying phase shift response. When performing these simulations, only the central unit cell of the microlens array was illuminated for analyzing the concentration of the focused light. In the ideal case, this focused light should only be present in the central IR-FPA pixel that spans $30\mu m$ width in the focal plane.

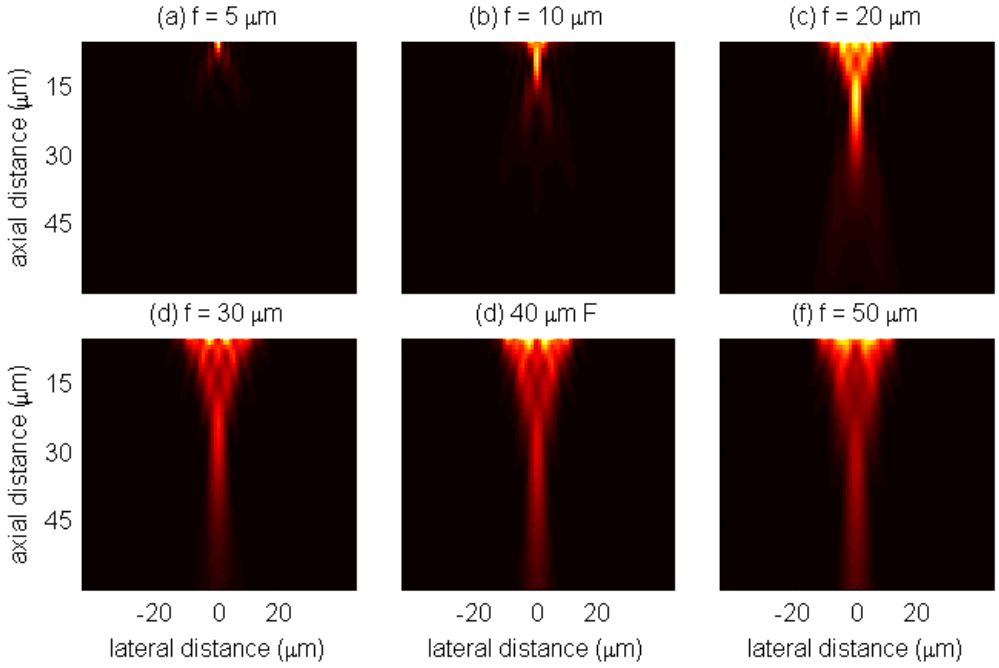


Figure 4.6: Intensity distributions of the cross-polarized field obtained by illuminating the central unit cell of the proposed metasurface-based FPAs [1].

## 4.3 Results and Discussions

Point-spread function (PSF) is used to characterize the optical cross-talk in FPA's [2]. In order to quantitatively analyze the optical cross-talk in the proposed designs, the corresponding areas under the PSF curve of the distribution in the central pixel and its nearest neighbor of the IR-FPA is integrated. A moderate f-number (1.8) is chosen for two reference systems. One of them is a system that does not include microlenses while the other one is a system that is composed of refractive microlens arrays (which is the same as the one used in a previous microlens study [2]). Following the integration of the corresponding areas in the reference study, it was found that 95.7% and 94.9% of the total energy were focused to the central pixel for the system without a microlens and the refractive microlens system, respectively. However, 2.15% and 2.55% of the energy were also focused to each one of the nearest neighbor pixels, respectively. 2.2% and 2.6% optical crosstalk's were obtained following the division of these ratios. Surprisingly, the optical crosstalk of the microlens system was higher than the reference system without microlenses and the reason for this situation is the emergence of the strong first order diffraction spots at the center of the adjacent pixels. These diffraction spots issue is a fundamental drawback of the refractive microlens array systems. Metasurface based microlens arrays do not include this drawback and over 96% of the incident energy is focused in the central pixel in all of the designs with the focal length parameters of 10, 20, 30, 40 and 50 $\mu m$. The highest value obtained was 98.4% in the case of 10 $\mu m$ focal length structure. This enhancement is a direct consequence of the inherent non-diffractive characteristics of metasurfaces. However, despite this improvement, it should also be noted that asymmetric metallic V-shaped nanoantennas only focus cross-polarized light and, as a result, total focusing efficiency of the microlens arrays is decreased when both polarizations are taken into consideration. The optical cross-talk values are given in Table 4.1.

Spatial cross-talk consists of two components and one of them is the optical crosstalk is one of the two components of spatial crosstalk in IR-FPA pixels and the other one is the electrical crosstalk [2]. The spatial cross-talk for the reference system and the refractive microlens system were found to be 2.82% and 2.9%, respectively, in the reference refractive microlens study. These values are compared with the optical cross-talk performances and it was observed that the

Table 4.1: Percentages of optical energy in the central and neighbor pixels [1]

| MWIR-FPA's | Halfwidth ($\mu m$) | Optical Cross-talk (%) |
|---|---|---|
| Reference | 7.7 | 2.2 |
| Refractive microlens | 2.6 | 2.6 |
| f = 10 $\mu m$ microlens | 1.0 | 0.8 |
| f = 20 $\mu m$ microlens | 1.2 | 1.0 |
| f = 30 $\mu m$ microlens | 1.7 | 2.0 |
| f = 40 $\mu m$ microlens | 2.0 | 1.4 |
| f = 50 $\mu m$ microlens | 2.2 | 1.9 |

resulting spatial crosstalk is much closer and the reason for this is a potential reduction in the spatial cross-talk due to much narrowed Airy disk in refractive microlenses. The normal halfwidth of the reference system was 9 $\mu m$ and this was reduced to 3 $\mu m$ (approximate to a 9-fold narrowing) with refractive microlens arrays. The proposed metasurface designs have normal halfwidths shorter than 1.0, 1.2, 1.7 and 2 $\mu m$ for the focal length parameters of 10, 20, 30 and 40 $\mu m$, respectively, (The reference system has a 7.74 $\mu m$ normal halfwidth that can be calculated by Equation (4.3)). Therefore, a substantial narrowing is achieved with the metasurface-based microlens arrays (narrowing roughly by 38-folds). This substantial narrowing shall also lead to further reduction of the spatial crosstalk in IR-FPAs with metasurface-based microlenses already allowing for much weaker optical crosstalk.

$$HW = \lambda_0 F_{\#} \tag{4.3}$$

# Chapter 5

# MWIR Dielectric Metasurface Microlens Array with High Transmission Efficiency and Good Optical Crosstalk

In this chapter, a dielectric metasurface-based microlensed FPA that relies on silicon nanodisks and operates in MWIR region is presented and its resulting high efficiency light concentrating capability is quantitatively analyzed, which is useful for suppressing optical cross-talk in MWIR-FPAs with higher f-numbers.

## 5.1 Efficiency Problem

One of the critical performance parameters of MWIR FPAs is its optical crosstalk as stated in Section 4.1. This noise parameter is especially important for electro-optical systems used in infrared imaging applications such as detection and tracking of small and dim (low signal-to-noise ratio (SNR)) objects. Another important parameter of MWIR FPAs is its f-number and relatively higher f-number MWIR

FPAs can be required for applications that are very sensitive to optical aberrations (Optical aberrations increase with smaller f-number). However, the optical crosstalk of conventional MWIR FPAs also increases with higher f-numbers [2]. To overcome these difficulties, different methodologies based on integration of different types of microlens arrays has been studied [1, 2]. The spot size of the incoming beam was narrowed much better than conventional MWIR FPAs when refractive type microlens arrays was used. Despite this promising result, the optical crosstalk performance was not improved surprisingly and the primary reason is the emergence of diffraction spots. The integration of metallic metasurface type microlens arrays for suppressing optical crosstalk was discussed in Chapter 4. Although an excellent optical crosstalk performance ($leq$ 1%) was obtained, the focusing efficiency was extremely low to make metallic metasurfaces of MWIR FPAs practical.

Metallic metasurfaces has been studied extensively over the last couple of years as stated in Chapter 2 and offer promising features such as broadband functionality. However, the device efficiency has become a common problem of transmission-mode metallic metasurfaces [9,13,14,21,25,27,45–53,55–62]. Here high absorption losses of metallic nanoantennas and cross-polarized focusing scheme dictated by asymmetric antennas are the main reasons of this typical drawback. Because of this phenomena, practical usage of metallic metasurfaces is limited to reflectance mode optical components. Therefore, for designing an efficient metasurface microlens array of MWIR FPAs that can be used in practice, metallic nanoantennas should be replaced by much more efficient nanoantennas.

## 5.2 Approach, Methodology and Modeling

### 5.2.1 Dielectric Metasurface Approach and Methodology

Recently, dielectric nanoantennas have been used as building blocks of dielectric metasurfaces and highly efficient transmission-mode dielectric metasurfaces were designed [67, 69, 77, 102–104]. Dielectric metalenses with high numerical aperture were studied and diffraction-limited focusing efficiency up to 86% was claimed to be observed after realizing these metalenses using $TiO_2$ nanofins [77]. However,

the metalens design was for the visible portion of the spectrum and length of the $TiO_2$ nanofins were too large for scaling and designing a nanoantenna which can be used in realization of metasurface microlens arrays of MWIR FPAs. Also, sub-wavelength thick high numerical aperture metalenses were studied and focusing efficiency reaching 82% was claimed to be observed after realizing these metalenses using silicon posts on hexagonal lattices [69]. However, the diameter of the nanopost were also too large for scaling and designing a nanoantenna which can be used in realization of metasurface microlens arrays of MWIR FPAs having pitch size less than 30 $\mu m$. Also, the metalens designs were for the near-infrared portion of the spectrum. Using silicon nanodisks having relatively smaller size that can be scaled and used in realization of such a metasurface microlens, Gaussian to Vortex beam shaping was studied but the device efficiency was slightly lower (close to 70%) and the design was also for the near infrared [67].

For addressing the optical crosstalk problem of conventional MWIR FPAs and efficiency problem of metallic metasurfaces of MWIR FPAs, we used an approach based on designing optical crosstalk optimized dielectric metasurfaces. First part of this approach is increasing the device efficiency dramatically and for doing so, a new dielectric metasurface of MWIR FPAs using silicon nanodisks is proposed. However, while improving the device efficiency dramatically, the superior optical crosstalk performance of metallic metasurfaces (which however suffer undesirably high, fundamental absorptive loss) of MWIR FPAs should also be fullfilled. Another key consideration that should be taken into account is preventing the increase in optical crosstalk due to increase in f-number, thereby paving the way of higher f-number MWIR FPAs with low optical crosstalk. For achieving these altogether, silicon nanodisks, which can cover the full 0-to-$2\pi$ phase shift range (see Fig. Figure 5.1(a) for the phase shift response of dielectric nanoantennas) should replace the asymmetrically tailored metallic antennas used in Chapter 4. This is a necessary condition for designing metasurfaces and providing higher transmission efficiency.

Using this approach, first, we focused on the specific design of silicon nanodisks that fullfills the phase shift criterion with high transmission efficiency in MWIR. Then, phase shift profile of the microlens arrays were designed for dramatically increasing focusing efficiency and satisfying good optical crosstalk while preventing the increase in optical crosstalk due to increase in f-number. Following the design, the microlens array was realized by placing the designed nanodisks in a

set of 8 nanoantennas in appropriate locations of an array with subwavelength separation (see Fig. Figure 5.1(b) and Fig. Figure 5.1(c)).

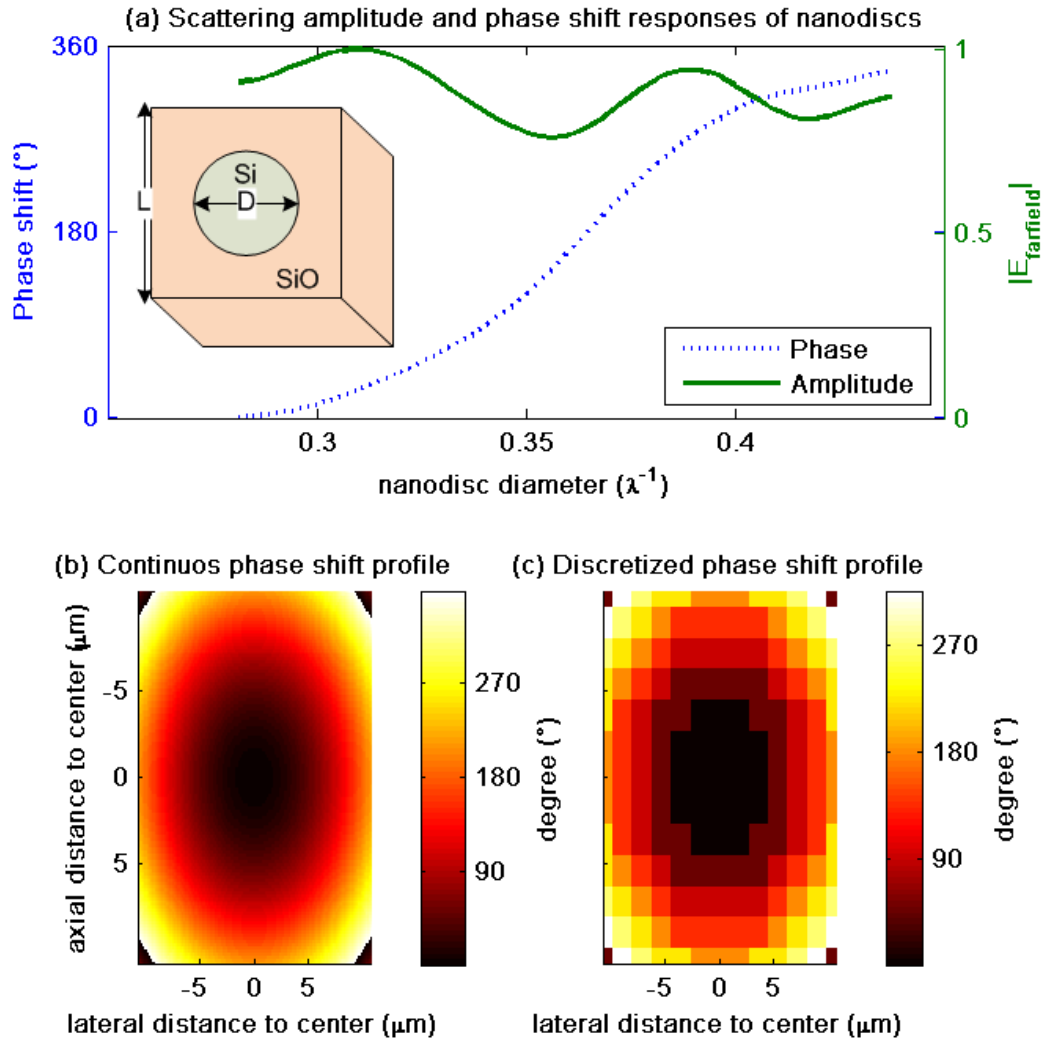


Figure 5.1: (a) Scattering amplitude and phase shift responses of the silicon nanodisks that cover the 0-to-2$\pi$ phase shift coverage with highly uniform amplitude response (Geometry of the Si nanodisk is shown in the inset). (b) Ideal (continuous) phase profile that should be imparted by a single microlens in the microlens array having a pitch length of 20 $\mu m$. (c) Discretization of the ideal phase profile for realization with silicon nanodisks inside unit cells having an edge length of 1800 nm.

The ideal phase profile that must be imparted by a metalens is given by Eq.Equation (5.1). For achieving excellent optical crosstalk performance while keeping f-number (f/#) more than a reasonably high value (1.5) (increasing FoM), a design methodology based on restriction of a parameter of Eq.Equation (5.1) was developed. According to this design methodology, focal length variable was picked as the design variable and its value was limited to a certain range of values that provide a phase shift of at least $\pi$ radians between the center and edge of a microlens in the microlens array while keeping a ratio that is greater than the threshold of 1.5 between itself and aperture size of the microlens. This methodology was used in designing various dielectric metasurfaces of MWIR FPAs having focal length varied from 15 to 90 $\mu m$ and aperture size varied from 20 to 30 $\mu m$ depending on the value of focal length parameter.

$$\theta = \frac{2\pi}{\lambda}\left(\sqrt{x^2 + y^2 + f^2} - f\right) \tag{5.1}$$

### 5.2.2 Modeling and Simulations

For designing the set of silicon nanodisks, the resonance and transmission conditions were used for computing the initial parameters for diameter and height of nanodisks. For the MWIR band (3-to-5 $\mu m$), the diameter was varied from approximately 1000 to 1800 nm while the height was half of the diameter values. The silicon nanodisk is placed inside a unit cell which is a square with an edge length varied from 1500 to 2500 nm (during different design runs). The mutual coupling between nanoantennas was taken into account and minimized when determining the edge length for unit cell. For modeling and simulating these silicon nanodisks, full-wave simulations were performed using Lumerical finite difference time domain (FDTD) solver. Each nanodisk was placed at the center of a simulation region and surrounded by a homogenous medium. A monochromatic plane wave source is used to excite the nanodisk and a near-field monitor is placed to record the near-field data. Then, the near-field data was transformed into far-field data by using transformation functions provided by Lumerical FDTD. Periodic boundary conditions were used as boundary conditions along the axial directions and perfectly matched layers (PML) boundary condition was imposed at the normal direction as the boundary condition. After conducting a series of simulation runs, an optimized silicon nanodisk set was designed for the design wavelength of 3.2 $\mu m$ and for the homogeneous medium refractive index of 1.42 which is close

to the refractive index of fused silica. The diameters, phase shift and amplitude responses of these silicon nanodisks were given in Table Table 5.1 (Height was fixed at 550 nm). The main advantage gained by replacing metallic nanoantennas by silicon nanodisks was the dramatically increased transmission efficiency. For calculating the transmission efficiency of metallic and dielectric unit cells that will be used in realizing metasurfaces, full wave simulations were performed and transmitted power was recorded on a field monitor. The unit cells containing asymmetrically shaped metallic nanoantennas scattered cross-polarized light with an efficiency of 11% while the unit cells containing the silicon nanodisks transmitted any polarization with an efficiency more than 65% and even reaching 90% for the diameter of 1020 nm (this diameter to height ratio most probably corresponds to the Kerkers condition at which the electric and magnetic dipoles spectrally overlap, allowing almost unity transmission [94]).

Table 5.1: Far-field responses of designed silicon nanodisks.

| Nanodisk No | Diameter ($nm$) | Phase shift ($^\circ$) | Scattering amp. |
|---|---|---|---|
| 1 | 1240 | 35 | 0.94 |
| 2 | 1320 | 79 | 0.82 |
| 3 | 900 | 125 | 0.92 |
| 4 | 1020 | 167 | 0.98 |
| 5 | 1090 | 214 | 0.82 |
| 6 | 1130 | 256 | 0.77 |
| 7 | 1160 | 295 | 0.77 |
| 8 | 1200 | 347 | 0.87 |

For realizing the designed phase profile with Si nanodisks, this phase profile must be discretized. For implementing this discretization process, continuously changing portions of the continuous profile is mapped into constant phase regions. For example, $0 - to - 4\pi$ phase shift portion of the continuous profile was mapped to the 0 phase shift while the $\frac{\pi}{4} - to - \frac{\pi}{2}$ phase shift portion of the continuous profile was mapped to the $\frac{\pi}{4}$ phase shift so that only a single type of nanodisk (nanodisk no. 1) were placed in the 0 phase shift regions while another type of nanodisk (nanodisk no. 1) were placed in the $\frac{\pi}{4}$ phase shift region. (See Fig. 5.2(a) for the realization of the central microlens with silicon nanodisks).

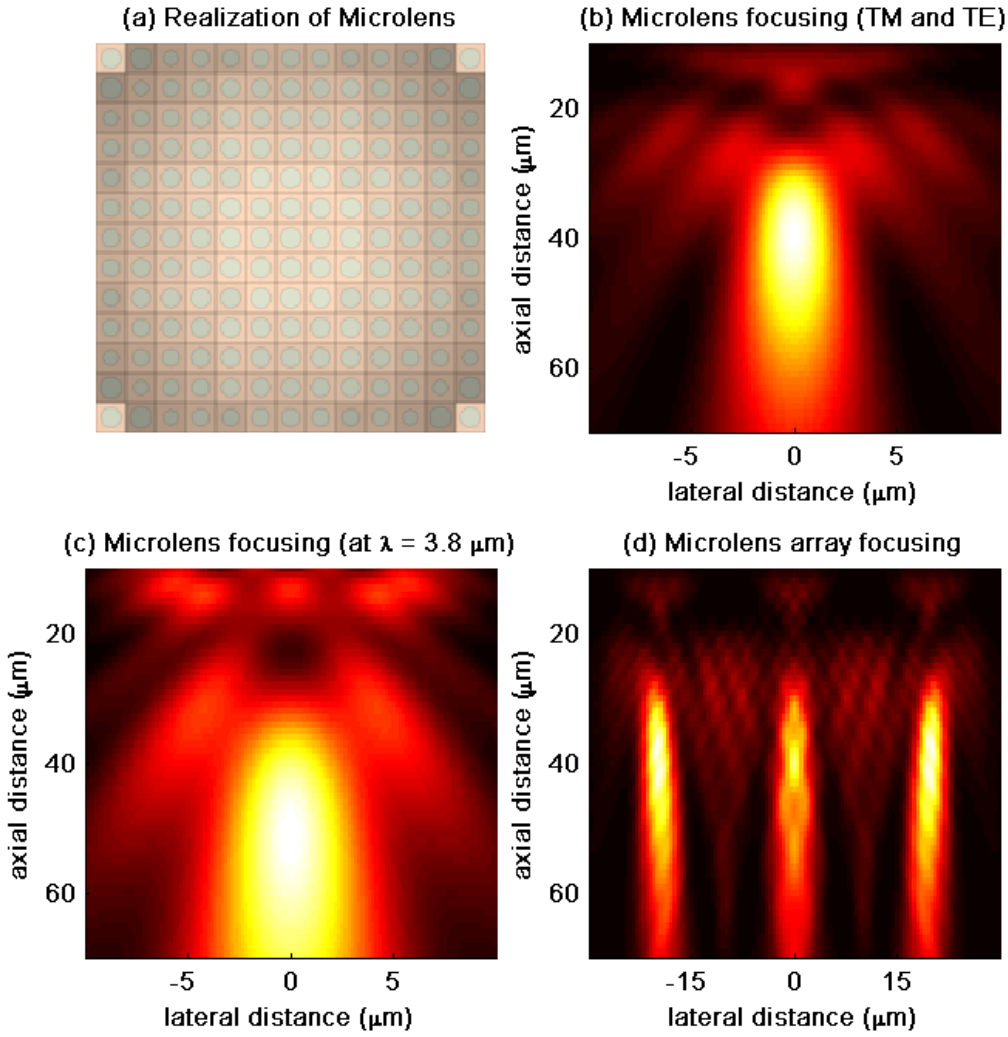


Figure 5.2: (a) Realization of the optimized design's central microlens by silicon nanodisks (color of unit cells are graded within constant phase regions). (b) Far-field intensity distribution of light focused by the central microlens of the optimized design when excited with either TM or TE polarized light. (c) Far-field intensity distribution of light focused by the central microlens of the optimized design for the wavelength of 3.5 $\mu m$ which is different from the design wavelength. (d) Far-field intensity distribution of light focused by different pixels of the optimized microlens array design.

After realization, full wave simulations were performed by exciting these microlens arrays with both polarizations (TM and TE) of light. For the source, a monochromatic plane wave with the design wavelength of 3.2 $\mu m$ was used. In Fig. Figure 5.2(b), far-field distribution of light (which was the same distribution for both TM and TE polarizations of light) scattered from the central microlens of the optimized microlens array design is presented. As understood from Fig. Figure 5.2(b), unlike the metallic metasurfaces that require cross-polarization scheme to function, the dielectric metasurface microlens can focus both polarizations of light efficiently due to its cylindrically symmetric structure. Since the MWIR FPAs are designed to function at a certain portion of spectrum (not just a single wavelength), we simulated the behavior of dielectric metasurface microlens array at different wavelengths. When the source wavelength was changed to 3.5 $\mu m$ (300 nm away from the design wavelength) for analyzing the device performance at a different wavelength, we observed that the focusing behavior of the microlens array was disturbed (See Fig. Figure 5.2(c) for the distribution of 3.5 $\mu m$ wavelength light from the same central microlens). This is a drawback of the dielectric metasurfaces when compared to the metallic metasurfaces that can work over a broader range of wavelengths. However, the focusing efficiency of the dielectric metasurface is more than 80% which is a dramatic improvement considering the very low focusing efficiency (11%) of metallic metasurfaces. Finally, far-field light distribution of all the microlenses in the optimized design is given in Fig. Figure 5.2(d).

## 5.3 Results and Discussions

For MWIR FPAs, optical crosstalk is characterized by point spread function (PSF) [2]. When the incoming light from a point source is focused on a pixel of the FPA, its energy is distributed spatially. Although main portion of the distribution is inside the central pixel, some portion of it leaks to neighbor pixels and this is the source of optical crosstalk. Therefore, optical crosstalk can be calculated as the ratio of the corresponding PSF distributions inside the neighbor and central pixels. Eq. Equation (5.2) can be used for computing optical crosstalk. The optical crosstalk values of designed microlens arrays were compared with other types (refractive and metallic metasurface) of microlens arrays

and conventional MWIR FPAs. The halfwidths of the focused beams and optical crosstalk values are given in Table 5.2. Although dielectric metasurfaces have lower optical crosstalk (≤3%) than refractive microlens arrays and conventional MWIR FPAs, metallic metasurfaces have the lowest optical crosstalk (≤2%) for f-number greater than 2.0. The primary reason of the slightly degraded optical crosstalk performance is undersampling of the phase profile due to greater unit cell size of dielectric metasurfaces (more than twice of the metallic unit cells).

Table 5.2: Halfwidth and optical crosstalk values of different types of MWIR FPAs

| IR-FPAs | Halfwidth ($\mu m$) | Optical Crosstalk (°) |
|---|---|---|
| f/2.0 Conventional | 6.4 | 3.2 |
| f/2.8 Conventional | 8.9 | 4.1 |
| f/2.0 Refractive M.A. | 3.0 | 3.0 |
| f/2.0 Metallic Metasurface M.A. | 2.2 | 2.0 |
| f/2.6 Metallic Metasurface M.A. | 2.8 | 2.5 |
| f/2.0 Dielectric Metasurface M. A. | 2.4 | 2.5 |
| f/3.0 Dielectric Metasurface M. A. | 3.0 | 2.9 |

The transmission (focusing) efficiency of designed microlens arrays were compared with other types (refractive and metallic metasurface) of microlens arrays and conventional MWIR FPAs. The resulting values are given in Table 5.3. As expected, dielectric metasurfaces (≥80%) outperform the metallic ones (≤11%) by a promising factor of 8, enabling the practical usage of microlens arrays based on dielectric metasurfaces. Main reasons for this improvement are the lack of cross-polarization scheme and removal of the intrinsic absorption losses occurring in metallic nanoantennas.

Table 5.3: Transmission (focusing) efficiencies of metasurface microlens arrays

| IR-FPAs | Focusing efficiency (°) |
|---|---|
| f/2.0 Metallic Metasurface M.A. | 10.4 |
| f/2.6 Metallic Metasurface M.A. | 10.7 |
| f/2.0 Dielectric Metasurface M. A. | 68.5 |
| f/3.0 Dielectric Metasurface M. A. | 80.6 |

$$Crosstalk = 100 \times \frac{\int\limits_{A_{neighbor}} PSF(x,y)dA}{\int\limits_{A_{central}} PSF(x,y)dA} \tag{5.2}$$

For infrared imaging applications regarding the detection and tracking of small objects with low SNR, firstly, the photons irradiated from the object should be collected (focused) on the FPA as much as possible. Thus, the transmission efficiency of any component betweent the FPA and the object (such as microlens arrays) should be as high as possible. More importantly, these photons should be collected by the right pixel (by engineering the PSF) by minimizing the optical crosstalk for improving the spatial SNR. However, conventional MWIR FPAs with relatively lower optical crosstalk has small f-numbers which is disadvantageous for reducing optical aberrations [2]. Therefore, an MWIR FPA should have a high FoM, which is directly proportional to the transmission efficiency and f-number while inversely proportional to the optical crosstalk. In designing and optimizing our dielectric metasurfaces, we aimed to maximize this FoM. Fig Figure 5.3 shows the FoM comparison of different types of MWIR FPAs. Despite achieving excellent optical crosstalk, metallic metasurfaces of MWIR FPAs have the lowest FoM values due to their very poor focusing efficiency. Refractive microlens array MWIR FPAs do not show any improvement regarding either optical crosstalk or f-number, thereby the FoM. The arrow in Fig Figure 5.3 shows the optimization process of our proposed metasurfaces which have the highest FoM after achieving better optical crosstalk values (with higher f-numbers) than reflective microlens array and conventional MWIR FPAs while having a dramatically improved transmission efficiency compared to the metallic metasurfaces.

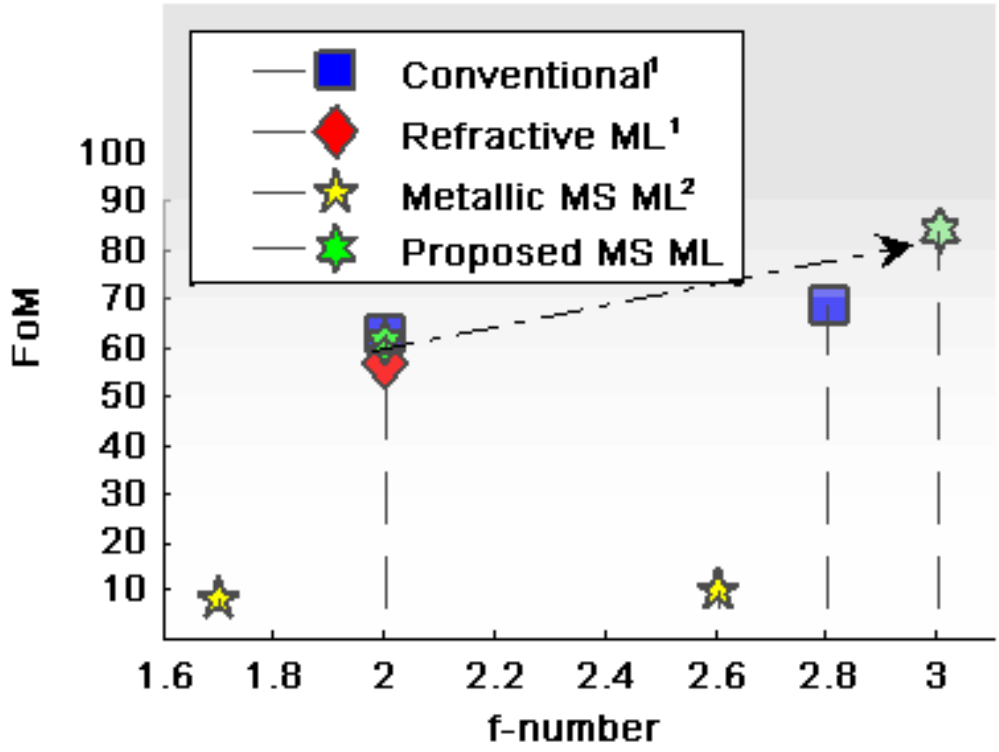


Figure 5.3: FoM comparisons of different types of MWIR FPAs showing superior performance of proposed (dielectric) metasurface microlensed (green hexagram marker) FPAs over conventional [2] (blue square markers suffering from higher optical crosstalk), refractive microlensed [2] (red circle marker suffering from diffraction noise) and metallic metasurface microlensed [1] (yellow pentagram marker suffering from very poor transmission performance) FPAs.

To conclude this chapter, we have proposed and demonstrated an efficient, high-SNR, low-crosstalk microlens array integrated MWIR FPA designs based on dielectric metasurfaces that can be used in MWIR portion of the infrared spectrum. We confirmed the expected behavior of these designs and analyzed the focusing efficiencies and crosstalk performances by performing full-wave simulations in Lumerical FDTD and compared these results to those of the microlens arrays based on metallic metasurfaces and other types of microlens arrays and conventional MWIR FPAs. We showed that high focusing efficiency (over 80%) can be obtained while achieving best figure of merit (at a level of 84) and preserving ultralow optical crosstalk (at a level of 2.6%) which is still superior to refractive microlens arrayed MWIR FPAs without the inclusion of mesa-isolation technique. These MWIR microlens arrays can be used to improve the spatial noise performance of corresponding MWIR FPAs so that small objects with low SNR can possibly be detected at much lower false alarm rates.

# Chapter 6

# Conclusion and Future Outlook

Optical components are key parts of the electro-optical (EO) and infrared (IR) systems. However, conventional optical components have bulky structure that can include multiple parts and the choice of transparent material is limited in certain portions of the electro-magnetic spectrum. Due to these drawbacks, the system complexity and cost of EO and IR systems increase. Moreover, the functionality and performance of these systems can also be limited and degraded when conventional optical components are used such as the emergence of diffraction spots increased spatial cross-talk when microlens arrays are built from refractive lenses.

Metamaterials generalized the concept of transformation optics and enabled emergence of a new class of optical components. New phenomena such as abnormal light bending, sub-wavelength focusing and cloaking have been shown. However, despite the addition of these new functionalities, material characteristics still impose rigid restrictions of usual Snell's law on capabilities of optical components based on metamaterials. Recently, metasurfaces, two-dimensional counterparts of metamaterials, have been investigated and relying on a different concept in which abrupt phase changes are used, new optical components such as meta-lenses and meta-holograms are designed, fabricated and characterized. However, focal plane arrays (FPAs) have not been studied using metasurfaces and optical-crosstalk problem have not been dealt with such meta-lens arrays.

Alternatively, we proposed and designed new optical components based on

metasurfaces and addressed the problems of optical-crosstalk and focusing efficiency in MWIR FPAs using the metasurface concept. To summarize, in this thesis study:

1. We developed simple nanoantenna models for different shapes of metallic and dielectric nanoantennas. Then, we derived the integral equations for finding the current distributions on metallic nanoantennas using method of moments.

2. We characterized the far-field amplitude and phase shift responses of metallic nanoantennas by re-radiating the current distributions that are calculated using the simple models we developed . Then, we probed a large parameter space for finding suitable nanoantenna types that can be used to built metasurfaces.

3. We developed a more realistic model that can be used in performing full-wave simulations in order to find precise metallic and dielectric nanoantennas that can be used to built high-performance metasurface lenses and metasurface mirrors.

4. We developed a design methodology that can be used to model optical components from metasurfaces. Then, using this design methodology we designed metasurface lenses, metasurface parabolic mirrors and metasurface magnetic mirrors. We investigated the far-field distributions of scattered light from these models and confirmed the predescribed functionalities of metasurface lenses and mirrors.

5. We designed sets of asymmetrically shaped metallic nanoantennas and silicon nanodisks that have incremental phase shifts of $\frac{\pi}{4}$ and an almost constant amplitude response in order to maximize the constructive interference that defines the functionality of metasurface lenslets.

6. We proposed and designed metallic MWIR microlens arrays built from the set of asymmetrically shaped optical antennas. By performing full-wave simulations and by varying the design parameter ($f$) of microlens arrays, we obtained far-field distributions of cross-polarized scattered light. Then, we compared the spot size narrowing ability and optical-crosstalk performance of our designs with reference systems (one without microlens arrays and one

with refractive microlens arrays) and showed the superior optical-crosstalk suppression ability of microlens arrays designed from metasurfaces.

7. We proposed and designed dielectric MWIR microlens arrays built from the set of silicon nanodisks. By performing full-wave simulations and by varying the design parameter ($f$) of microlens arrays, we obtained far-field distributions of cross-polarized scattered light. Then, we compared the optical-crosstalk performance and focusing efficiency of our designs with reference systems (MWIR FPAs without microlens arrays, MWIR FPAs with refractive microlens arrays and MWIR FPAs with metallic metasurface microlens arrays) and showed the superior figure of merit performance of microlens arrays designed from dielectric metasurfaces.

## 6.1 Scientific Contributions

Our research studies began with the investigation of the energy transfer between excitons and plasmons. We proposed and designed several architectures of cascaded nanofilms that consist of semiconductor quantum dots (QD) and metallic nanoparticles (MNP). After fabricating these devices with Layer-by-Layer assembly and characterizing the optical properties, we observed a 2.7 fold emission enhancement in acceptor QDs and showed that with precise engineering of the distance and arrangement of QDs and MNPs, emission of QDs can be further enhanced. This study has led to publications of a science-citation index journal (Nano Letters) and two refereed international conference papers [105–107].

This research work has led to several designs of a new-class of optical components using metasurfaces both in transmitting and reflecting mode. For building these optical components from optical resonators, different sets of metallic nanoantennas were designed. In order to design these nanoantennas, simple models of metallic nanoantennas were developed after solving the integral equations describing the current distributions on these antennas. After gaining experience in designing several optical components and antenna sets, we improved the amplitude response uniformity performance of antennas by adding another degree of freedom in geometry of the nanoantennas. Then, using these nanoantennas, metasurface microlens arrays are designed and modeled in order to address the optical

crosstalk problem in MWIR-FPA's. Superior optical crosstalk suppression and beam narrowing properties of these designs are shown and compared to reference systems such as refractive microlens arrays. This study also led to a publication of a science-citation index journal (Optics Express) [1]. However, since the focusing efficiencies of metallic metasurface microlens arrays was too low to make these devices practical, we focused on designing and modeling microlens arrays built from dielectric metasurfaces for increasing the device efficiency dramatically. First, we designed a set of silicon nanodisks for realizing dielectric metasurface microlens arrays. Then, we confirmed the superior focusing efficiency of dielectric metasurface microlens arrays by performing full-wave simulations. Finally, we optimized our dielectric metasurface designs for also achieving low optical crosstalk. This study also led to a manuscript which is submitted to the Applied Physics Letters journal.

## 6.2 Future Outlook

MWIR FPAs are core components of EO and IR systems used in detection and tracking of objects with low signal-to-noise ratio (SNR). As a future work, we aim to study the integration of dielectric metasurface microlens arrays to MWIR FPAs for reducing the optical crosstalk of the system without degrading transmission efficiency, thereby increasing the SNR of small and dim objects spatially. By increasing the SNR and reducing crosstalk, the false alarm rates of such electro-optical systems can be reduced and the reliability of the system in detection and tracking of small and dim objects can increase.

# Bibliography


[1] O. Akin and H. V. Demir, "Mid-wave infrared metasurface microlensed focal plane array for optical crosstalk suppression," *Optics Express*, vol. 23, pp. 27020–27027, 2015.

[2] Y. Li, Z.-H. Ye, W.-D. Hu, W. Lei, Y.-L. Gao, K. He, H. Hua, P. Zhang, Y.-Y. Chen, C. Lin, X.-N. Hu, R.-J. Ding, and L. He, "Numerical simulation of refractive-microlensed hgcdte infrared focal plane arrays operating in optical systems," *Journal of Electronic Materials*, vol. 43, no. 8, pp. 2879–2887, 2014.

[3] K. Seyrafi and S. A. Hovanessian, *Introduction to electro-optical imaging and tracking systems*. Artech House, 1993.

[4] R. G. Driggers, P. Cox, and T. Edwards, *Introduction to infrared and electro-optical systems*. Artech House, 1999.

[5] N. Yu, P. Genevet, M. A. Kats, F. Aieta, J.-P. Tetienne, F. Capasso, and Z. Gaburro, "Light propagation with phase discontinuities: generalized laws of reflection and refraction," *Science*, vol. 38, no. 7, pp. 964 – 972, 2011.

[6] M. Esfandyarpour, E. C. Garnett, Y. Cui, M. D. McGehee, and M. L. Brongersma, "Metamaterial mirrors in optoelectronic devices," *Nature Nanotechnology*, vol. 9, pp. 542–547, 2014.

[7] N. Engheta and R. W. Ziolkowski, *Metamaterials: Physics and Engineering Explorations*. Wiley-IEEE Press, 2006.

[8] W. Cai and V. Shalaev, *Optical Metamaterials: Fundamentals and Applications*. Springer, 2009.

[9] X. Ni, N. K. Emani, A. V. Kildishev, A. Boltasseva, and V. M. Shalaev, "Broadband light bending with plasmonic nanoantennas," *Science*, vol. 335, p. 427, 2012.

[10] N. Yu, F. Aieta, P. Genevet, M. A. Kats, and Z. Gaburro, "A broadband, background-free quarter-wave plate based on plasmonic metasurfaces," *Nano Letters*, vol. 12, pp. 6328–6333, 2012.

[11] M. Kang, T. Feng, H. Wang, and J. Li, "Wave front engineering from an array of thin aperture antennas," *Optics Express*, vol. 20, no. 14, pp. 15882–15890, 2012.

[12] A. V. Kildishev, A. Boltasseva, and V. M. Shalaev, "Planar photonics with metasurfaces," *Science*, vol. 28, no. 7, pp. 1037 – 1050, 2013.

[13] N. Yu and F. Capasso, "Flat optics with designer metasurfaces," *Nature Materials*, vol. 13, no. 2, pp. 139–150, 2014.

[14] X. Yin, Z. Ye, J. Rho, Y. Wang, and X. Zhang, "Photonics spin-hall effect at metasurfaces," *Science*, vol. 339, no. 6126, pp. 1405–1407, 2013.

[15] N. Shitrit, S. Maayani, D. Veksler, V. Kleiner, and E. Hasman, "Rashba-type plasmonic metasurface," *Optics Letters*, vol. 38, no. 21, pp. 4358–4361, 2013.

[16] S. Sun, Q. He, S. Xiao, Q. Xu, X. Lin, and L. Zhou, "Gradient-index metasurfaces as a bridge linking propagating waves and surface waves," *Nature Materials*, vol. 11, no. 5, pp. 426–431, 2012.

[17] S. Sun, K. Yang, C. Wang, T. Juan, W. T. Chen, C. Y. Liao, Q. He, S. Xiao, W. Kung, G. Guo, L. Zhou, and D. P. Tsai, "High-efficiency broadband anomalous reflection by gradient meta-surfaces," *Nano Letters*, vol. 12, no. 12, pp. 6223–6229, 2012.

[18] D. Lin, P. Fan, E. Hasman, and M. L. Brongersma, "Dielectric gradient metasurface optical elements," *Science*, vol. 345, no. 6194, pp. 298–301, 2014.

[19] F. Aieta, P. Genevet, N. Yu, M. A. Kats, Z. Gaburro, and F. Capasso, "Out-of-plane reflection and refraction of light by anisotropic optical antenna metasurfaces with phase discontinuities," *Nano Letters*, vol. 12, no. 3, pp. 1702–1706, 2012.

[20] P. Genevet, N. Yu, F. Aieta, J. Lin, M. A. Kats, R. Blanchard, M. O. Scully, Z. Gaburro, and F. Capasso, "Ultra-thin plasmonic optical vortex plate based on phase discontinuities," *Applied Physics Letters*, vol. 100, no. 1, p. 013301, 2012.

[21] Y. Zhao and A. Alu, "Manipulating light polarization with ultrathin plasmonic metasurfaces," *Physical Review B*, vol. 84, no. 20, p. 205428, 2011.

[22] J. Lin, P. Genevet, M. A. Kats, N. Antoniou, and F. Capasso, "Nanostructured holograms for broadband manipulation of vector beams," *Nano Letters*, vol. 13, no. 9, pp. 4269–4274, 2013.

[23] W. T. Chen, K. Yang, C. Wang, Y. Huang, G. Sun, I. Chiang, C. Y. Liao, W. Hsu, H. T. Lin, S. Sun, L. Zhou, A. Q. Liu, and D. P. Tsai, "High-efficiency broadband meta-hologram with polarization controlled dual images," *Nano Letters*, vol. 14, no. 1, pp. 225–230, 2014.

[24] X. Ni, A. V. Kildishev, and V. M. Shalaev, "Metasurface holograms for visible light," *Nature Communications*, vol. 4, p. 2807, 2013.

[25] M. A. Kats, P. Genevet, G. Aoust, N. Yu, R. Blanchard, F. Aieta, Z. Gaburro, and F. Capasso, "Giant birefringence in optical antenna arrays with widely tailorable optical anisotropy," *Proceedings of the National Academy of Sciences USA*, vol. 109, no. 31, pp. 12364–12368, 2012.

[26] A. Shaltout, V. Shalaev, and A. Kildishev, "Homogenization of bi-anisotropic metasurfaces," *Optics Express*, vol. 21, no. 19, pp. 21941–21950, 2013.

[27] M. Farmahini-Farahani, J. Cheng, and H. Mosallaei, "Metasurfaces nanoantennas for light processing," *Journal of Optical Society of America B*, vol. 30, no. 9, pp. 2365–2370, 2013.

[28] F. Aieta, P. Genevet, M. A. Kats, N. Yu, R. Blanchard, Z. Gaburro, and F. Capasso, "Aberration-free ultrathin flat lenses and axicons at telecom wavelengths based on plasmonic metasurfaces," *Nano Letters*, vol. 12, no. 9, pp. 4932–4936, 2012.

[29] X. Ni, S. Ishii, A. V. Kildishev, and V. M. Shalaev, "Ultra-thin, planar, babinet-inverted plasmonic metalenses," *Light: Science and Applications*, vol. 2, no. 4, p. e72, 2013.

[30] F. Aieta, P. Genevet, M. Kats, and F. Capasso, "Aberrations of flat lenses and aplanatic surfaces," *Optics Express*, vol. 21, no. 25, pp. 31530–31539, 2013.

[31] F. Aieta, M. A. Kats, P. Genevet, and F. Capasso, "Multiwavelength achromatic metasurfaces by dispersive phase compensation," *Science*, vol. 347, no. 6228, pp. 1342–1345, 2015.

[32] Y. Sun, B. Edwards, A. Alu, and N. Engheta, "Experimental realization of optical lumped nanocircuits at infrared wavelengths," *Nature Materials*, vol. 11, pp. 208–212, 2012.

[33] H. Caglayan, S.-H. Hong, B. Edwards, C. R. Kagan, and N. Engheta, "Near-infrared metatronic nanocircuits by design," *Physical Review Letters*, vol. 111, no. 7, p. 073904, 2013.

[34] F. Abbasi and N. Engheta, "Roles of epsilon-near-zero (enz) and mu-near-zero (mnz) materials in optical metatronic circuit networks," *Optics Letters*, vol. 22, no. 21, pp. 25109–25119, 2014.

[35] H. T. Miyazaki and Y. Kurokawa, "Controlled plasmon resonance in closed metal/insulator/metal nanocavities," *Applied Physics Letters*, vol. 89, no. 211126, 2006.

[36] D. Fattal, J. Li, Z. Peng, M. Fiorentino, and R. G. Beausoleil, "Flat dielectric grating reflectors with focusing abilities," *Nature Photonics*, vol. 4, pp. 466–470, 2010.

[37] A. Polyakov, M. Zolotorev, P. Schuck, and H. Padmore, "Collective behavior of impedance matched plasmonic nanocavities," *Optics express*, vol. 20, no. 7, pp. 7685–7693, 2012.

[38] J. A. Fan, C. Wu, K. Bao, J. Bao, R. Bardhan, N. J. Halas, V. N. Manoharan, P. Nordlander, G. Shvets, and F. Capasso, "Self-assembled plasmonic nanoparticle clusters," *Science*, vol. 328, pp. 1135–1138, 2010.

[39] B. Lukyanchuk, N. I. Zheludev, S. A. Maier, N. J. Halas, P. Nordlander, H. Giessen, and C. tow Chong, "The fano resonance in plasmonic nanostructures and metamaterials," *Nature Materials*, vol. 9, pp. 707–715, 2010.

[40] A. Moreau, C. Ciracì, J. J. Mock, R. T. Hill, Q. Wang, B. J. Wiley, A. Chilkoti, and D. R. Smith, "Controlled-reflectance surfaces with film-coupled colloidal nanoantennas," *Nature*, vol. 492, no. 7427, pp. 86–89, 2012.

[41] R. D. Grober, R. J. Schoelkopf, and D. E. Prober, "Optical antenna: Towards a unity efficiency near-field optical probe," *Applied Physics Letters*, vol. 70, no. 1354, 1997.

[42] L. Novotny and N. van Hulst, "Antennas for light," *Nature Photonics*, vol. 5, pp. 83–90, 2011.

[43] C. Jansen, I. A. Al-Naib, N. Born, and M. Koch, "Terahertz metasurfaces with high q-factors," *Applied Physics Letters*, vol. 95, no. 5, p. 051109, 2011.

[44] N. Yu, P. Genevet, F. Aieta, M. A. Kats, R. Blanchard, G. Aoust, J.-P. Tetienne, Z. Gaburro, and F. Capasso, "Flat optics: controlling wavefronts with optical antenna metasurfaces," *IEEE Journal of Selected Topics in Quantum Electronics*, vol. 19, no. 3, pp. 4700423–4700423, 2013.

[45] C. Ma and Z. Liu, "A super resolution metalens with phase compensation mechanism," *Applied Physics Letters*, vol. 96, no. 18, p. 183103, 2010.

[46] B. Memarzadeh and H. Mosallaei, "Array of planar plasmonic scatterers functioning as light concentrator," *Optics Letters*, vol. 36, no. 13, pp. 2569–2571, 2011.

[47] X. Chen, L. Huang, H. Mühlenbernd, G. Li, B. Bai, Q. Tan, G. Jin, C.-W. Qiu, S. Zhang, and T. Zentgraf, "Dual-polarity plasmonic metalens for visible light," *Nature communications*, vol. 3, p. 1198, 2012.

[48] C. Qu, S. Xiao, S. Sun, Q. He, and L. Zhou, "A theoretical study on the conversion efficiencies of gradient meta-surfaces," *EPL (Europhysics Letters)*, vol. 101, no. 5, p. 54002, 2013.

[49] C. Pfeiffer and A. Grbic, "Cascaded metasurfaces for complete phase and polarization control," *Applied Physics Letters*, vol. 102, no. 23, p. 231116, 2013.

[50] M. Pu, P. Chen, Y. Wang, Z. Zhao, C. Huang, C. Wang, X. Ma, and X. Luo, "Anisotropic meta-mirror for achromatic electromagnetic polarization manipulation," *Applied Physics Letters*, vol. 102, no. 13, p. 131906, 2013.

[51] X. Wan, W. X. Jiang, H. F. Ma, and T. J. Cui, "A broadband transformation optics metasurface lens," *Applied Physics Letters*, vol. 104, no. 15, p. 151601, 2014.

[52] R. Blanchard, G. Aoust, P. Genevet, N. Yu, M. A. Kats, Z. Gaburro, and F. Capasso, "Modeling nanoscale v-shaped antennas for the design of optical phased arrays," *Physical Review B*, vol. 85, no. 155457, 2012.

[53] M. Farmahini-Farahani and H. Mosallaei, "Birefringent reflectarray metasurface for beam engineering in infrared," *Optics letters*, vol. 38, no. 4, pp. 462–464, 2016.

[54] F. Aieta, A. Kabiri, P. Genevet, N. Yu, M. A. Kats, Z. Gaburro, and F. Capasso, "Reflection and refraction of light from metasurfaces with phase discontinuities," *Journal of Nanophotonics*, vol. 6, no. 1, pp. 063532–063532, 2012.

[55] T. Roy, E. T. Rogers, and N. I. Zheludev, "Sub-wavelength focusing metalens," *Optics express*, vol. 21, no. 6, pp. 7577–7582, 2013.

[56] L. Huang, X. Chen, H. Mühlenbernd, H. Zhang, S. Chen, B. Bai, Q. Tan, G. Jin, K.-W. Cheah, C.-W. Qiu, *et al.*, "Three-dimensional optical holography using a plasmonic metasurface," *Nature communications*, vol. 4, 2013.

[57] L. Huang, X. Chen, B. Bai, Q. Tan, G. Jin, T. Zentgraf, and S. Zhang, "Helicity dependent directional surface plasmon polariton excitation using a metasurface with interfacial phase discontinuity," *Light: Science & Applications*, vol. 2, no. 3, p. e70, 2013.

[58] D. Hu, X. Wang, S. Feng, J. Ye, W. Sun, Q. Kan, P. J. Klar, and Y. Zhang, "Ultrathin terahertz planar elements," *Advanced Optical Materials*, vol. 1, no. 2, pp. 186–191, 2013.

[59] E. Karimi, S. A. Schulz, I. De Leon, H. Qassim, J. Upham, and R. W. Boyd, "Generating optical orbital angular momentum at visible wavelengths using

a plasmonic metasurface," *Light: Science and Applications*, vol. 3, no. 5, p. e167, 2014.

[60] W. Wang, Z. Guo, R. Li, J. Zhang, Y. Li, Y. Liu, X. Wang, and S. Qu, "Plasmonics metalens independent from the incident polarizations," *Optics express*, vol. 23, no. 13, pp. 16782–16791, 2015.

[61] G. Zheng, H. Mühlenbernd, M. Kenney, G. Li, T. Zentgraf, and S. Zhang, "Metasurface holograms reaching 80% efficiency," *Nature nanotechnology*, vol. 10, no. 4, pp. 308–312, 2015.

[62] D. Wintz, P. Genevet, A. Ambrosio, A. Woolf, and F. Capasso, "Holographic metalens for switchable focusing of surface plasmons," *Nano letters*, vol. 15, no. 5, pp. 3585–3589, 2016.

[63] P. R. West, J. L. Stewart, A. V. Kildishev, V. M. Shalaev, V. V. Shkunov, F. Strohkendl, Y. A. Zakharenkov, R. K. Dodds, , and R. Byren, "All-dielectric subwavelength metasurface focusing lens," *Optics Express*, vol. 22, no. 21, p. 26212, 2014.

[64] J. Cheng, D. Ansari-Oghol-Beig, and H. Mosallaei, "Wave manipulation with designer dielectric metasurfaces," *Optics letters*, vol. 39, no. 21, pp. 6285–6288, 2014.

[65] M. Decker, I. Staude, M. Falkner, J. Dominguez, D. N. Neshev, I. Brener, T. Pertsch, and Y. S. Kivshar, "High-efficiency dielectric huygens surfaces," *Advanced Optical Materials*, vol. 3, pp. 813–820, 2015.

[66] Y. F. Yu, A. Y. Zhu, R. Paniagua-Dominguez, Y. H. Fu, B. Lukyanchuk, and A. I. Kuznetsov, "High-transmission dielectric metasurface with 2pi phase control at visible wavelengths," *Laser Photonics Reviews*, vol. 9, no. 4, pp. 412–418, 2015.

[67] K. E. Chong, I. Staude, A. James, J. Dominguez, S. Liu, S. Campione, G. S. Subramania, T. S. Luk, M. Decker, and D. N. Neshev, "Polarization-independent silicon metadevices for efficient optical wavefront control," *Nano Letters*, vol. 15, pp. 5369–5374, 2015.

[68] M. I. Shalaev, J. Sun, A. Tsukernik, A. Pandey, K. Nikolskiy, and N. M. Litchinitser, "High-efficiency all-dielectric metasurfaces for ultracompact

beam manipulation in transmission mode," *Nano Letters*, vol. 15, pp. 6261–6266, 2015.

[69] A. Arbabi, Y. Horie, A. J. Ball, M. Bagheri, and A. Faraon, "Subwavelength-thick lenses with high numerical apertures and large efficiency based on high-contrast transmitarrays," *Nature Communications*, vol. 6, no. 7069, 2015.

[70] Y. Yang, I. I. Kravchenko, D. P. Briggs, and J. Valentine, "All-dielectric metasurface analogue of electromagnetically induced transparency," *Nature Communications*, vol. 5, no. 5773, 2015.

[71] A. Arbabi, Y. Horie, M. Bagheri, and A. Faraon, "Dielectric metasurfaces for complete control of phase and polarization with subwavelength spatial resolution and high transmission," *Nature Nanotechnology*, vol. 10, no. 937–944, 2015.

[72] S. W. Kim, K. J. Yee, M. Abashin, L. Pang, and Y. Fainman, "Composite dielectric metasurfaces for phase control of vector field," *Optics Letters*, vol. 40, no. 11, pp. 2453–2456, 2015.

[73] B. Desiatov, N. Mazurski, Y. Fainman, and U. Levy, "Polarization selective beam shaping using nanoscale dielectric metasurfaces," *Optics Express*, vol. 23, no. 17, p. 243526, 2015.

[74] A. F. Koenderink, A. Al, and A. Polman, "Nanophotonics: Shrinking light-based technology," *Science*, vol. 348, pp. 517–520, 2015.

[75] P. Moitra, B. A. Slovick, W. Li, I. I. Kravchencko, D. P. Briggs, S. Krishnamurthy, and J. Valentine, "Large-scale all-dielectric metamaterial perfect reflectors," *ACS Photonics*, vol. 2, no. 6, pp. 692–698, 2015.

[76] V. Asadchy, Y. Radi, J. Vehmas, and S. Tretyakov, "Functional metamirrors using bianisotropic elements," *Physical review letters*, vol. 114, no. 9, p. 095503, 2015.

[77] M. Khorasaninejad, W. T. Chen, R. C. Devlin, J. Oh, A. Y. Zhu, and F. Capasso, "Metalenses at visible wavelengths: Diffraction-limited focusing and subwavelength resolution imaging," *Science*, vol. 352, no. 6290, pp. 1190–1194, 2016.

[78] S. Jahani and Z. Jacob, "All-dielectric metamaterials," *Nature nanotechnology*, vol. 11, no. 1, pp. 23–36, 2016.

[79] V. Asadchy, M. Albooyeh, and S. Tretyakov, "Optical metamirror: all-dielectric frequency-selective mirror with fully controllable reflection phase," *JOSA B*, vol. 33, no. 2, pp. A16–A20, 2016.

[80] S. Pancharatnam, "Generalized theory of interference and its applications part ii. partially coherent pencils," *Proceedings of Indian Academy of Sciences*, 1956.

[81] M. V. Berry, "The adiabatic phase and phancharatnam's phase for polarized light," *Journal of Modern Optics*, vol. 34, no. 11, pp. 1401–1407, 1987.

[82] Z. Bomzon, V. Kleiner, and E. Hasman, "Pancharatnamberry phase in space-variant polarization-state manipulations with subwavelength gratings," *Optics Letters*, vol. 26, no. 18, pp. 1424–1426, 2001.

[83] E. Hasman, V. Kleiner, G. Biener, and A. Niv, "Polarization dependent focusing lens by use of quantized pancharatnamberry phase diffractive optics," *Applied Physics Letters*, vol. 82, no. 3, pp. 328–330, 2003.

[84] B. E. A. Saleh and M. C. Teich, *Fundamentals of Photonics*. New York: Wiley, 1991.

[85] E. Hasman, Z. Bomzon, A. Niv, G. Biener, and V. Kleiner, "Polarization beam-splitters and optical switches based on space-variant computer-generated subwavelength quasi-periodic structures," *Optics Communications*, vol. 209, pp. 45–54, 2002.

[86] S. J. Orfanidis, *Electromagnetic Waves and Antennas*. Unpublished, 2014. http://www.ece.rutgers.edu/ orfanidi/ewa/.

[87] N. Engheta, C. H. Papas, and C. Elachi, "Radiation patterns of interfacial dipole antennas," *Radio Science*, vol. 17, no. 1557, 1982.

[88] G. W. Bryant, F. J. G. de Abajo, and J. Aizpurua, "Mapping the plasmon resonances of metallic nanoantennas," *Nano Letters*, vol. 8, no. 2, pp. 631–636, 2008.

[89] A. B. Evlyukhin, C. Reinhardt, A. Seidel, B. S. Luk'yanchuk, and B. N. Chichkov, "Optical response features of si-nanoparticle arrays," *Physical Review B*, vol. 82, no. 4, p. 045404, 2010.

[90] A. Garcia-Etxarri, R. Gomez-Medina, L. S. Froufe-Perez, C. Lopez, L. Chantada, F. Scheffold, J. Aizpurua, M. Nieto-Vesperinas, and J. J. Saenz, "Strong magnetic response of submicron silicon particles in the infrared," *Optics Express*, vol. 19, no. 6, pp. 4815–4826, 2011.

[91] L. Chao, P. Fan, E. S. Barnard, A. M. Brown, and M. L. Brongersma, "Tuning the color of silicon nanostructures," *Nano Letters*, vol. 10, no. 7, pp. 2649–2654, 2010.

[92] B. I. Popa and S. A. Cummer, "Compact dielectric particles as a building block for low-loss magnetic metamaterials," *Physical review letters*, vol. 100, no. 20, p. 207401, 2008.

[93] Q. Zhao, J. Zhou, F. Zhang, and D. Lippens, "Mie resonance-based dielectric metamaterials," *Materials Today*, vol. 12, no. 12, pp. 60–69, 2009.

[94] M. Kerker, D. S. Wang, and C. L. Giles, "Electromagnetic scattering by magnetic spheres," *Journal of Optical Society of America*, vol. 73, no. 6, pp. 765–767, 1983.

[95] Y. H. Fu, A. I. Kuznetsov, A. E. Miroshnichenko, Y. F. Yu, and B. Luk'yanchuk, "Directional visible light scattering by silicon nanoparticles," *Nature communications*, vol. 4, no. 1527, 2013.

[96] S. Person, M. Jain, Z. Lapin, J. J. Saenz, G. Wicks, and L. Novotny, "Demonstration of zero optical backscattering from single nanoparticles," *Nano Letters*, vol. 13, no. 4, pp. 1806–1809, 2013.

[97] W. J. Troph, "Temperature-dependent refractive index models for baf2, caf2, mgf2, srf2, lif, naf, kcl, zns and znse," *Optical Engineering*, vol. 34, 1995.

[98] M. Kazes, D. Y. Lewis, Y. Ebenstein, T. Mokari, and U. Banin, "Lasing from semiconductor quantum rods in a cylindrical microcavity," *Advanced Materials*, vol. 14, no. 4, pp. 317–321, 2002.

[99] J. Le Perchec, P. Quemerais, A. Barbara, and T. Lopez-Rios, "Why metallic surfaces with grooves a few nanometers deep and wide may strongly absorb visible light," *Physical review letters*, vol. 100, no. 6, p. 066408, 2008.

[100] J. Bai, W. Hu, N. Guo, W. Lei, Y. Lv, X. Zhang, J. Si, X. Chen, and W. Lu, "Performance optimization of insb infrared focal-plane arrays with diffractive microlenses," *J. Electron. Mater.*, vol. 43, pp. 2795–2801, 2014.

[101] E. D. Palik, *Handbook of Optical Constants of Solids*. Academic, 1991.

[102] J. H. Lee, J. W. Yoon, M. J. Jung, J. K. Hong, S. H. Song, and R. Magnusson, "A semiconductor metasurface with multiple functionalities: A polarizing beam splitter with simultaneous focusing ability," *Applied Physics Letters*, vol. 104, no. 23, p. 233505, 2014.

[103] Y. Liu, X. Ling, X. Yi, X. Zhou, H. Luo, and S. Wen, "Realization of polarization evolution on higher-order poincaré sphere with metasurface," *Applied Physics Letters*, vol. 104, no. 19, p. 191110, 2014.

[104] J. Kim, D. Shin, S. Choi, D.-S. Yoo, I. Seo, and K. Kim, "Meta-lens design with low permittivity dielectric materials through smart transformation optics," *Applied Physics Letters*, vol. 107, no. 10, p. 101906, 2015.

[105] T. Ozel, P. L. Hernandez-Martinez, E. Mutlugun, O. Akin, S. Nizamoglu, I. O. Ozel, Q. Zhang, Q. Xiong, and H. V. Demir, "Observation of selective plasmon-exciton coupling in nonradiative energy transfer: donor-selective versus acceptor-selective plexcitons," *Nano letters*, vol. 13, no. 7, pp. 3065–3072, 2013.

[106] O. Akin, T. Ozel, and H. V. Demir, "Cascading plasmonic and nonradiative energy transfer interactions by plasmon-coupling only donor or only acceptor quantum dots of the energy transfer pairs," in *IEEE Photonics Society, 2010 23rd Annual Meeting*, pp. 582–583, IEEE, 2010.

[107] P. L. Hernandez-Martinez, T. Ozel, E. Mutlugun, O. Akin, S. Nizamoglu, I. O. Ozel, Q. Zhang, Q. Xiong, and H. V. Demir, "Selective plasmon-exciton coupling in nonradiative energy transfer: Donor-selective versus acceptor-selective," in *APS Meeting Abstracts*, vol. 1, p. 50002, 2014.